Loan Copy #3

POLARIZATION EFFECTS ON MAGNETIC RESONANCES IN FERROELECTRIC POTASSIUM TANTALATE

STUART H. WEMPLE

TECHNICAL REPORT 425

DECEMBER 31, 1964

MASSACHUSETTS INSTITUTE OF TECHNOLOGY
RESEARCH LABORATORY OF ELECTRONICS
CAMBRIDGE, MASSACHUSETTS

The Research Laboratory of Electronics is an interdepartmental laboratory in which faculty members and graduate students from numerous academic departments conduct research.

The research reported in this document was made possible in part by support extended the Massachusetts Institute of Technology, Research Laboratory of Electronics, by the JOINT SERVICES ELECTRONICS PROGRAMS (U.S. Army, U.S. Navy, and U.S. Air Force) under Contract DA36-039-AMC-03200(E); and was performed under U.S. Army Signal Corps Contract DA36-039-sc-87376.

MASSACHUSETTS INSTITUTE OF TECHNOLOGY

RESEARCH LABORATORY OF ELECTRONICS

Technical Report 425 December 31, 1964

POLARIZATION EFFECTS ON MAGNETIC RESONANCES IN FERROELECTRIC POTASSIUM TANTALATE

Stuart H. Wemple

This report is based on a thesis submitted to the Department of Electrical Engineering, M. I. T., February 4, 1963 in partial fulfillment of the requirements for the degree of Doctor of Philosophy.

(Revised manuscript received April 16, 1964)

Abstract

Electric field effects on electron paramagnetic resonances (EPR) associated with Fe^{3+} impurity ions in the perovskite ferroelectric $KTaO_3$ are presented and discussed. A large effect ($D = 30 \times 10^{-4}$ cm^{-1} for $E = 14$ kv/cm) was predicted and observed at 4.2°K. Because the extrapolated Curie temperature of $KTaO_3$ is close by (~0°K), large lattice polarizations and electrostrictive strains are induced by an externally applied electric field. This gives rise to a shift of the paramagnetic energy levels that is quadratic in the applied field. The effect is several orders of magnitude larger in $KTaO_3$ than has been reported for other centrosymmetric lattices.

The EPR angular dependence data for the Fe^{3+} ion in a cubic environment are interpreted in terms of appropriate spin Hamiltonian parameters. The result is $|a| = (345 \pm 10) \times 10^{-4}$ cm^{-1} and $g = 1.99 \pm 0.01$. We also reported EPR spectra for Fe^{3+} ions that have a neighboring oxygen vacancy, and also for Fe^{5+}, Mn, and Cr. Evidence for covalent bonding of magnetic impurities to the $KTaO_3$ lattice is given. These data include a resolved next-nearest-neighbor hyperfine interaction between the central Fe^{5+} ion and the surrounding eight spin-3/2 potassium nuclei.

Optical absorption spectra associated with Fe, Mn, and Co impurities are also reported.

A brief investigation was made of transport properties of slightly reduced, electrically conducting (n-type) samples of $KTaO_3$. There is a strong temperature-dependent Hall mobility (28 cm^2/volt sec at room temperature and at least 63,000 cm^2/volt sec at 4.2°K). The effective mass is large and temperature-dependent.

A method for growing fairly large (~1 cm^3) and good quality single crystals of $KTaO_3$ is described.

TABLE OF CONTENTS

I. INTRODUCTION

This investigation is primarily concerned with electron paramagnetic resonances (EPR) in single crystals of the perovskite ferroelectric potassium tantalate ($KTaO_3$). In particular, we are interested in the Stark effect produced on EPR spectra by externally applied electric fields.

Published results on the EPR Stark effect were scarce and most of the experimental work had been concerned with nuclear quadrupole resonances. Bloembergen[1] had concluded that a Stark effect that varies linearly with the electric field is possible only if the paramagnetic ions are located in host crystal sites that lack inversion symmetry. This is a direct consequence of the fact that the Stark operator $\mathcal{H}_s = -\bar{r} \cdot \bar{E}$ is an odd-parity operator and only mixes with odd-parity components of the crystalline field. Bloembergen and Royce,[2] as well as Artman and Murphy,[3] observed this linear effect in ruby (Cr^{3+} in Al_2O_3) and reported an 8.8×10^{-4} cm^{-1} shift in the axial splitting parameter D for an applied electric field of 100 kv/cm. They also interpreted their data on angular dependence by adding appropriate terms linear in $\bar{E}$ to the Cr^{3+} spin Hamiltonian.

Browne[4] failed to observe any electric field effects in potassium chrome alum or ammonium chrome alum for fields up to 10 kv/cm. From this negative result, he calculated a small upper limit to the electric dipole moment of the electron and concluded that terms of the form $\bar{S} \cdot \bar{E}$ need not be included in the Stark-effect Hamiltonian.

The largest electric field effects previously observed were in crystals with iron-group interstitial impurities (Fe^{o}, Fe^{1+}, Mn^{1+}, Cr^{o}) in silicon. Ludwig and Woodbury[5] and Ludwig and Ham[6] reported EPR splitting to 0.05 cm^{-1} for fields of 10 kv/cm. Ham[7] discussed the relevant theory and concluded that in the spin Hamiltonian the terms that are dependent on the electric field are largest for ions having ground-state orbital degeneracy or nearby excited states. This result indicated that neither S-state ions nor orbitally quenched ions are the ideal choices for EPR Stark-effect experiments.

A quadratic Stark effect is expected in any host lattice, regardless of the impurity site symmetry. If a center of inversion symmetry exists, as in a cubic lattice, only this second-order Stark effect will be present. Weger and Feher[8] observed such second-order effects in the spectrum of cubic MgO containing Cr^{3+} and reported that line shifts of approximately 0.004×10^{-4} cm^{-1} are produced by an applied electric field of 100 kv/cm. The only other known attempt to observe the quadratic effect in a centrosymmetric lattice was reported by Hornig, Rempel, and Weaver[9] for $BaTiO_3$ containing Fe^{3+}, but no shift in the EPR spectrum was observed. This negative result was puzzling and suggested that similar experiments in another perovskite would be worth while.

We have studied the EPR Stark effect in $KTaO_3$ containing Fe^{3+} ions, and report both the EPR spectra and the optical spectra with Fe, Mn, Co, and Cr ions as substitutional impurities.

As there were few published data on $KTaO_3$, it was necessary to investigate a number of peripheral topics, such as the dielectric, ferroelectric, and the optical properties of $KTaO_3$.

Some transport phenomena in semiconducting (reduced) samples were also measured and included electrical conductivity, Hall effect, and free carrier absorption. We also discuss narrow infrared absorption bands that we have associated with the presence of O-H bonds in the $KTaO_3$ lattice.

A crystal-growing method is described in detail.

II. SELECTION OF $KTaO_3$

An externally applied electric field causes an EPR Stark effect as a consequence of three physical effects. First, the field acts directly on the magnetic ion; second, the field polarizes the host lattice electron cloud and thus changes the electric potential at impurity sites; and third, the electric field shifts the equilibrium positions of all the nuclei. These nuclear displacements can be observed macroscopically as piezoelectric or electrostrictive strain and can produce large polarizations.

The local crystal field at a magnetic-ion site is altered slightly in a polarized lattice, and the consequent modification of the spin-orbit and spin-spin interactions changes the fine-structure energy levels of the magnetic ion.

Published results[2,3,8] on Cr^{3+}-doped Al_2O_3 and MgO plus our order-of-magnitude estimates indicated that very large polarizations and field-induced lattice distortions would be required to give a Stark effect with an easily observable line shift of 10 to 100×10^{-4} cm^{-1}. We have, therefore, confined our search for an appropriate host lattice crystal to those having large polarizations, especially to those with large piezoelectric or electrostrictive strains.

The required lattice strains would be approximately 0.01 per cent. Conventional piezoelectric materials do not allow lattice strains greater than 0.001 per cent. Strains of the required magnitude appear to be limited to a few perovskite ferroelectrics. Even in these materials the large effect is restricted to a small range of temperatures near the Curie transition.

The associated polarizations would have to exceed 3 μcoulombs/cm^2, but such polarizations require a dielectric constant of several thousands. Ferroelectric materials are apparently the only suitable host lattices in which a large EPR Stark effect could be expected. There are excellent review articles[10,11] on these materials. The perovskite family of ferroelectrics is particularly attractive, since this family exhibits the largest polarizations, has a simple crystalline structure, and contains a lattice site in which iron-group ions are expected to substitute readily.

The perovskite ferroelectrics have the generalized formula ABO_3, where A and B can be any of a large variety of cations.[11] Their valences must, of course, add up to six, and for structural reasons their ionic radii generally fall within a restricted range. The term perovskite includes the prototype cubic structure of Fig. 1, as well as structures that are slightly distorted forms of this basic lattice.

Several investigators,[9,12-19] have used EPR techniques to study the nature of ferroelectric phase transitions in the perovskites $BaTiO_3$ and $SrTiO_3$. This work was greatly facilitated by the ease with which iron-group impurities, as well as certain rare earths, enter the perovskite lattice. It has been found[9,12] that Fe^{3+} ions substitute at B sites (Ti^{4+}) in $BaTiO_3$ and $SrTiO_3$ without altering the local symmetry. The Fe^{3+} defect site is affected by the cooperative phenomenon that produces spontaneous polarization, and the associated local strains are comparable with those expected for the bulk lattice.

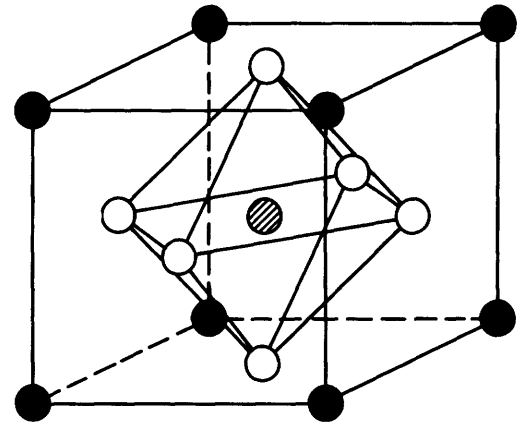

Fig. 1. Cubic perovskite unit cell. Formula ABO_3.
● A sites at cube corners.
⊘ B site at cube center.
O Oxygen sites at centers of cube faces.

We have selected the perovskite potassium tantalate ($KTaO_3$) for our EPR Stark-effect experiments for the following reasons:

1. $KTaO_3$ has a very low extrapolated Curie temperature (T_c) of 1°K. By operating in liquid helium, EPR measurements can be made at temperatures slightly greater than T_c for which the dielectric constant and the induced lattice polarizations are expected to be large. Liquid-helium operation stabilizes the temperature of the sample cavity and crystal. Also, the use of low temperature minimizes spin-lattice broadening that would limit the choice of magnetic-ion impurities.

2. Few dielectric measurements and no EPR had been reported. It was one of our purposes to compare the EPR in $KTaO_3$ with published results in the perovskites $BaTiO_3$ and $SrTiO_3$.

3. Polarization measurements[20] in potassium niobate ($KNbO_3$) gave a saturation value of approximately 30 μcoulombs/cm^2 in the tetragonal phase. This suggested that the chemically similar tantalate (also a I-V compound) might also exhibit large polarizations. Triebwasser[21] reported a saturation polarization of 9.7 μcoulombs/cm^2 in a mixed crystal containing 80 per cent $KTaO_3$ and 20 per cent $KNbO_3$.

III. GROWTH OF SINGLE-CRYSTAL $KTaO_3$

Two crystal-growing methods were used. In the first method, K_2CO_3 and Ta_2O_5 were dissolved in a molten potassium fluoride (KF) flux to produce a saturated solution of $KTaO_3$. Growth took place as the solution cooled. Even though use of this method produced small crystals of poor quality and low resistivity, it was indispensable because our seed crystals were obtained from flux runs. In the second, much more successful, method we used a rotating seed crystal suspended in a melt that consisted of Ta_2O_5 and a stoichiometric excess of K_2CO_3. Growth took place on the seed as the melt cooled through the appropriate region of the Ta_2O_5-K_2CO_3 phase diagram. We grew good-quality single crystals, approximately 1 cm^3 in size, by the melt method.

3.1 KF FLUX METHOD

The potassium tantalate single crystals used by Hulm, Matthais, and Long[22] to obtain their dielectric data were grown from a potassium fluoride (KF) flux in the Bell Telephone Laboratories. This method had been developed by J. P. Remeika[23] and others to grow a number of refractory oxide single crystals, including the well-known "butterfly wings" of barium titanate. In the KF flux method, the required compounds were dissolved in molten KF (melting point 891°C) in a platinum crucible. As the melt was slowly cooled, single crystals of the solute precipitated from the saturated solution onto the crucible wall. Because of the method's simplicity, we used this flux technique in the initial crystal-growing experiments. The chemical equation under consideration was

$$K_2CO_3 + Ta_2O_5 \xrightarrow{KF} 2KTaO_3 + CO_2.$$

Remeika[24] provided data that simplified our experiments. This information was expecially helpful in the case of $KTaO_3$, as no tertiary phase diagram was available for the KF-K_2CO_3-Ta_2O_5 system. He suggested that we (i) use stoichiometric ratios of K_2CO_3 and Ta_2O_5, (ii) use oxide-to-flux ratios between 1:5 and 1:10 by weight, (iii) heat the mixture to 1300°C and let it soak for several hours to ensure total solution, and (iv) cool the melt at 25°C per hour to 900°C.

We thoroughly mixed the reagent grade chemicals before filling the platinum crucible. A platinum-foil cover prevented excessive evaporation of the rather volatile KF. The crucible was inserted into a stabilized zirconia ceramic muffle, and the entire assembly was then placed in an electric furnace. The crystal-growing furnace and its controller are described in section 3.2a. We made 16 runs and tried a variety of oxide-to-flux ratios, soaking times, cooling rates, and stoichiometries.

We found that (i) using a ratio of K_2CO_3 to Ta_2O_5 larger than the stoichiometric ratio (which corresponds to a weight ratio of 0.31286) reduced the crystal quality and size; (ii) an oxide (Ta_2O_5) to flux (KF) ratio of 1:6 gave good results; (ii) a soaking temperature of 1300-1350°C was satisfactory but 1100°C was too low; soaking times of 5-10 hours

were equally effective; and (iv) cooling rates less than 20°C per hour reduced the crystal size. No claim to optimization could be made because of the large number of variables involved. A single attempt to use a $K_2B_2O_4$ flux rather than a KF flux gave a polycrystalline slag.

Most of the flux-grown $KTaO_3$ crystals were small cubes, 1-4 mm in size. The corners were always slightly flattened. The crystals were dark and opaque and had an electrical resistivity that was much too low (<1 ohm cm) for either magnetic resonance or dielectric constant measurements.

Our attempts to grow less opaque crystals of higher resistivity by decreasing the growing temperature were unsuccessful, although Remeika, using the same method and growth parameters, grew pale blue crystals.

Reduction in hydrogen ($Ti^{4+} \rightarrow Ti^{3+}$) makes the titanates ($SrTiO_3$, $BaTiO_3$, and TiO_2) opaque and conducting but they readily reoxidize. Nevertheless, attempts to oxidize our black tantalate crystals, and make them clear and nonconducting were unsuccessful, even when we kept them in flowing oxygen at 1250°C for 100 hours. Oxidation was limited to a very thin surface layer that could be polished away with a few strokes on emery paper. Apparently, oxygen diffusion rates are very low for $KTaO_3$.

Flux methods provide extraneous ions which can become incorporated in the crystal lattice as impurities. (For example, when barium titanate "butterfly wings" are grown by the KF flux method, it is thought that F^- ions lower the temperature of the cubic-tetragonal phase transition from 129°C to 120°C.) We discarded the KF flux method because of these difficulties.

3.2 MELT METHOD

This crystal-growing method, which produced single $KTaO_3$ crystals of good quality and high resistivity, is similar to that used by Miller[25] for growing $KNbO_3$. One of its important advantages is that it does not require the use of a flux with its associated extraneous ions. The only chemicals involved are K_2CO_3 and Ta_2O_5. Inspection of the published[26] phase diagram (Fig. 2) for the K_2CO_3-Ta_2O_5 reveals the crystal-growing conditions. The 50 mole per cent K_2O composition is the desired compound. (The CO_2 in K_2CO_3 is driven off during heating.) Addition of excess K_2O lower the melting point; the region below the associated liquidus line (50 to 68 mole per cent K_2O) is an equilibrium region between $KTaO_3$ and liquid. At 1090°C, a eutectic involving the compound $3K_2O \cdot Ta_2O_5$ begins to form, thereby placing a lower bound on the range of temperatures that allow $KTaO_3$ crystal growth.

a. Crystal-Growing Apparatus

The crystal-growing furnace is shown schematically in Fig. 3. Four silicon carbide Globars stand vertically inside the corners of the working space. The top of the furnace has an access hole that is plugged with an Al_2O_3-coated brick. This brick plug has holes for viewing, thermocouple holes, and a central hole for insertion of the shaft of the

seed-drive motor. The furnace power supply and controller are at the right of the furnace in Fig. 4. The controller is an "on-off" type with manual adjustment of the main variac. Cooling rates are determined by the taper on a motor-driven cam. The controller thermocouple enters the side of the furnace and

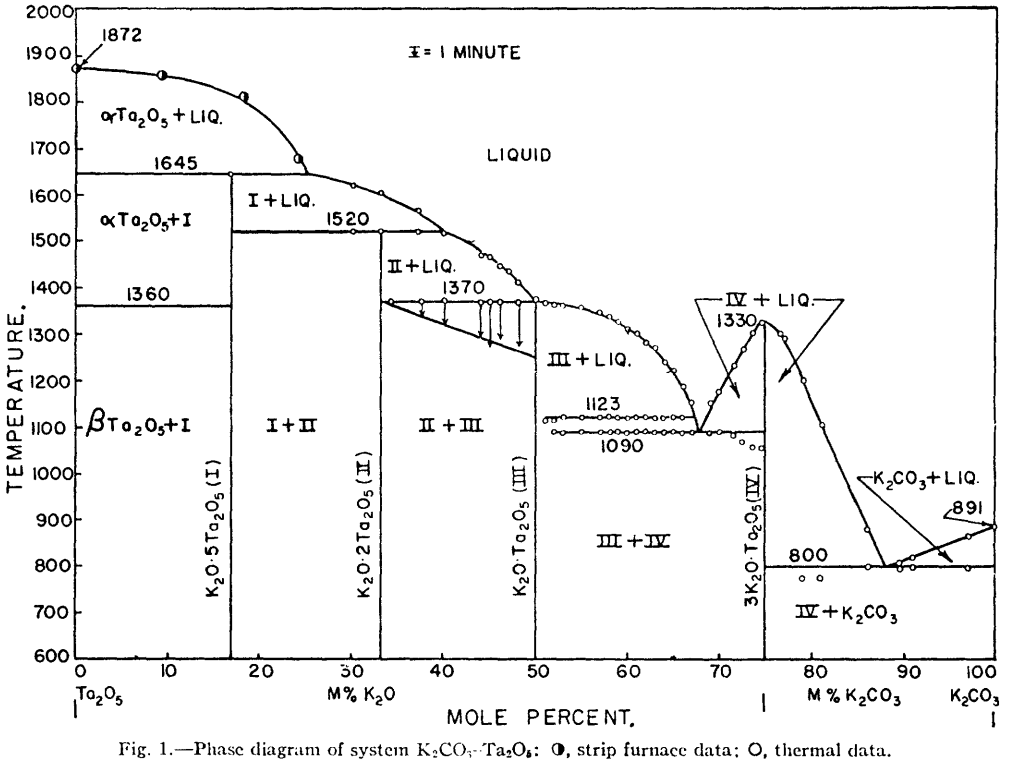

Fig. 1.—Phase diagram of system K_2CO_3-Ta_2O_5: ◑, strip furnace data; O, thermal data.

Fig. 2. K_2CO_3-Ta_2O_5 phase diagram (from Reisman, Holtzberg, Berkenblit, and Berry. Reprinted with permission of the American Chemical Society from J. Am. Chem. Soc. Vol. 78, p. 4517, September 20, 1956).

touches the outside of the Zircon muffle. Changes in temperature of approximately 5°C, which are required to actuate the on-off control, occur only outside the muffle. No temperature variations were observed within the platinum crucible during the controller cycles.

The 100-ml platinum crucible was contained in two ceramic crucibles. The inner one was stabilized zirconia and the outer was Zircon. Granular Al_2O_3 between the platinum and zirconia crucibles reduced the temperature gradients and also prevented sagging of the rather soft platinum at high temperature.

Mirrors, the strong light source, and a viewing telescope served as part of the liquidus-temperature measuring system.

The seed-drive motor rotated at 60 rpm and a time-delay relay circuit reversed the direction of rotation at 30-sec intervals.

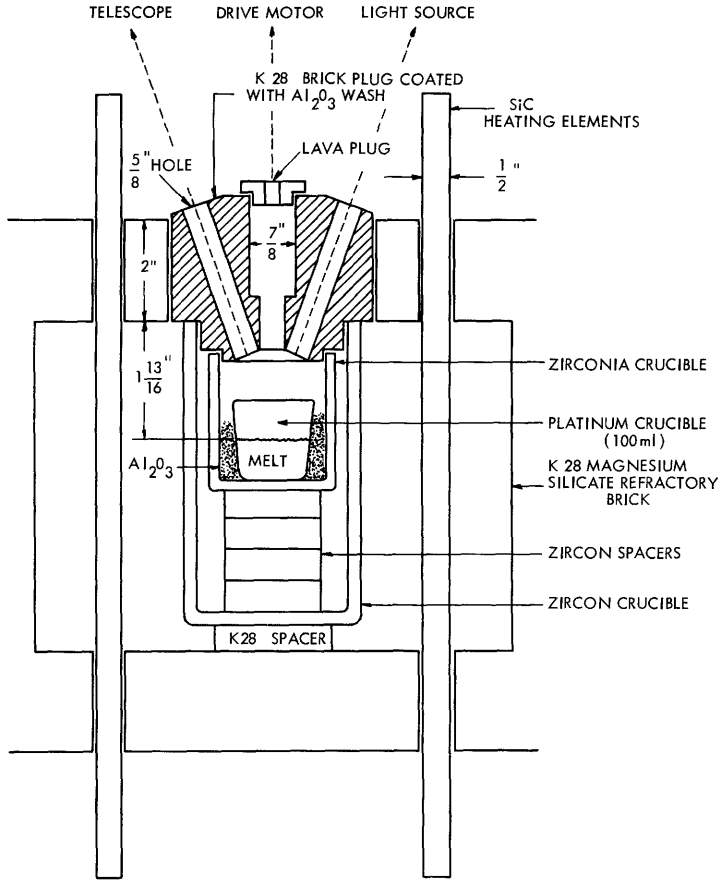

Fig. 3. Crystal-growing furnace.

b. Crystal-Growing Procedure

The best melt composition requires finding a compromise between low growth temperature and yield, since the yield approaches zero as the composition of the melt approaches the 68 mole per cent K_2O eutectic. A straightforward application of the lever rule to the phase diagram of Fig. 2 permits an estimation of yield for each melt composition. We assume that the crystal is removed from the melt at 1135°C, and list the results for various mole percentages of K_2O in Table I. M is the molar percentage of K_2O, W is the weight ratio K_2CO_3 to Ta_2O_5, and T_L is the liquidus temperature.

If crystals of approximately 1 cm^3 are desired, the necessary value of W can be estimated. The 100-ml platinum crucible can be filled with approximately 120 grams of chemicals and, since 1 cm^3 of $KTaO_3$ weighs 7 grams, yields greater than 6 per cent $KTaO_3$ are required. The liquidus temperature T_L and the crystal-removal temperature determine the total amount of $KTaO_3$ that precipitates from the melt. Only half of this actually forms on the seed; the rest solidifies on the crucible wall. Therefore, a 1-cm^3 crystal can be grown if the total yield is approximately 10 per cent. This yield is for a liquidus temperature (T_L) of 1200-1220°C and a weight ratio of 0.59. This

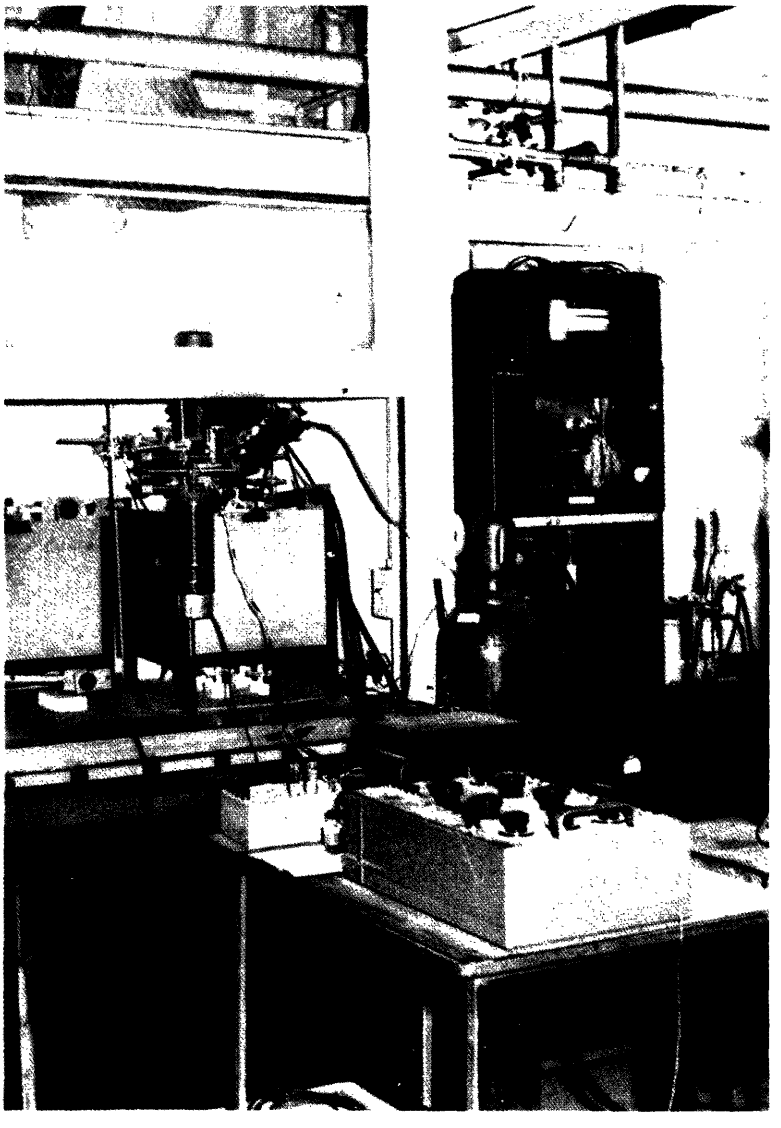

Fig. 4. Crystal-growing apparatus.

Table I. Expected crystal growth yield.

M	W	T_L (°C)	Yield by weight (%)
50	.31286	1370	93
60	.469	1310	46
64	.555	1245	22
65	.582	1219	14
66	.608	1183	6.5
67	.636	1135	0

estimate has been confirmed by our experiments.

Perhaps the most essential feature of the crystal-growing technique is the measurement of the precise liquidus temperature for each chemical charge. The published phase diagram does not have the necessary accuracy. This temperature measurement is important because the seed crystal must be brought in contact with the melt while the melt temperature is slightly (~2°C) above the liquidus temperature. A temperature that is too high will cause the seed to dissolve before crystal growth can begin, and a temperature below the liquidus temperature will prevent exposure of "fresh" seed surface upon which good single-crystal growth can be initiated.

A small (~0.1 × 0.1 × 0.2 mm^3) crystal of $KTaO_3$, obtained by the KF flux method, was dropped through a hole in the furnace plug and onto the melt surface in the platinum crucible. (The test crystal floats because of surface tension.) The thermal radiation was bright orange-red at 1200-1250°C. A 1000-watt projector lamp was used to "overpower" this radiation and permit visual observation of the melt surface and floating seed. The specular reflection from the melt surface was viewed through a telescope. Crossed polarizers were used to reduce the light intensity and the test crystal became clearly visible.

The liquidus temperature, T_L, was then determined by recording the solution times for a series of tiny test crystals while the melt was very slowly cooled. A typical set of solution times is given in Table II. The solution time depends upon the size of the test crystal, so crystals of comparable size are required. We lightly ground one of the small, dark, flux-grown crystals in a mortar and pestle. They cleave into tiny, thin plates which float well. As indicated in Table II, a large increase in solution time occurs for a small change in melt temperature as the liquidus temperature is approached. Other runs had shown that a test-crystal solution time (t_s) of 2-3 minutes corresponds to a temperature 1-2°C above T_L as this amount of additional cooling increases t_s to more than 10 minutes. At temperatures just above T_L, a test crystal will eventually dissolve;

Table II. Liquidus-determination solution times.

Melt temperature (°C)	Solution time t_s (seconds)
1218	5
1213	25
1211	25 (very tiny seed)
1209	45
1208	90
1207	150

just below T_L, the test crystal will not dissolve. A liquidus temperature of ~1206°C is therefore indicated in Table II.

Approximately three hours are required for the T_L determination because (i) very slow cooling rates are necessary to make certain that the thermocouple readings are an accurate reflection of the temperature changes in the melt, and (ii) there is a long time constant between controller temperature and melt temperature. Temperatures were measured with a Pt to Pt-10 per cent Rh thermocouple placed 1/2 inch above the melt surface. Temperature changes of approximately 0.1°C were detectable.

Determination of the liquidus temperature by this method makes it absolutely necessary to prevent small specks of dust from falling into the melt surface. In this event, the $KTaO_3$ test crystal is immediately drawn toward the impurity and visual observation of the solution is prevented. It was found necessary to coat the top furnace plug so that no small particles could fall from it onto the melt. An Al_2O_3 wash, fired at 1400°C, was found to be adequate for this purpose.

We must also keep the test crystal in the field of view. This tiny speck floats toward the nearest depression on the melt surface. If the inner wall of the platinum crucible is not smooth, the lowest point may easily lie outside the 5/8 inch field of view determined by the viewing holes in the furnace plug. This effect is due to the uneven meniscus along the platinum wall. It is necessary, therefore, to smooth the inner surface of the platinum crucible after each run.

Crystal growth takes place on a rotating seed crystal. This seed, which is ~3 × 4 × 7 mm^3, is tied to the end of a 0.125-inch platinum rod by 0.020-inch platinum wire. Holes in the seed are drilled with an ultrasonic driller.

Figure 5 shows exactly how the seed crystal is tied to the end of the platinum rod. This rod is 4.5 inches long and is fastened at its upper end to a 1/4 inch diameter stainless-steel rod that is connected to the motor shaft.

A brief chronological outline of the crystal-growing procedure follows. Typical

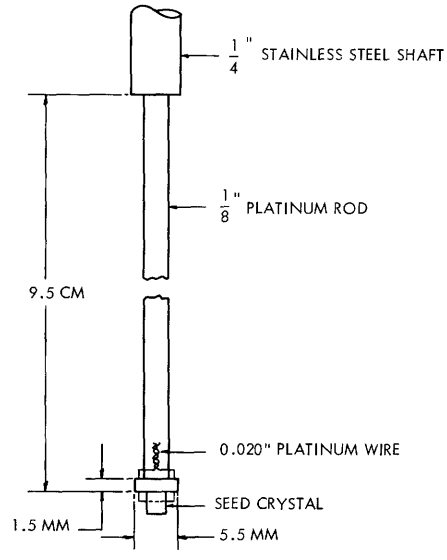

Fig. 5. Detail of seed-crystal mount.

experimental values are given in parentheses.

1. Mix chemicals in polyethylene bottle before placing in 100-ml platinum crucible. A typical charge that just fills the crucible is tabulated below.

Ta_2O_5	70.00 grams
K_2CO_3	42.10 grams
MnO_2	0.024 grams
SnO_2	0.012 grams

2. Slowly heat the mixture to the soaking temperature 10-20°C above liquidus (1218°C). This takes 12-15 hours. Soak for 4-6 hours.

3. Determine liquidus temperature (1200-1220°C) by test seed method.

4. Place seed-drive motor on rack and insert seed into furnace. Lower seed rather slowly (~5 minutes) to 0.5 cm from the melt surface.

5. Raise temperature of melt to approximately 5°C above T_L (one hour) and start the cam for a cooling rate of 3.5°C per hour.

6. As the melt passes through a temperature 2-3°C above T_L, lower the seed so that it touches the melt and then pull a small meniscus by lifting the seed 1-2 mm. It would take approximately 4 mm to break contact. The touching of the seed to the melt is clearly visible. Contact is also monitored by noting the electrical continuity through a circuit consisting of the shaft, seed, melt, platinum crucible, and an attached platinum wire that extends out of the furnace. This procedure was used by Miller.[25]

7. Start seed-drive motor.

8. Maintain the cooling rate for the entire growth period (~21 hours).

9. Pull crystal 1-2 mm at approximately 8-hour intervals during growth. Crystal pulling in a series of manual steps during the growth period prevents lateral growth; this is an important step because transverse growth tends to become polycrystalline after a maximum dimension of 1.5-2 cm is reached. The quality of the crystal growth can be observed as it progresses.

10. Lift crystal above melt at 1120-1130°C. Final temperatures in the vicinity of 1130°C were chosen because the eutectic did not form at 1090°C, as expected from the phase diagram, but occurred somewhere between 1100°C and 1120°C.

11. Change the cooling rate to 25-30°C per hour and anneal to room temperature (approximately two days). Definite color changes occur in the crystal during this annealing period. The crystal is bright green at 1100°C, green-yellow at 900°C, yellow at 600°C, and colorless at room temperature. These color changes are probably associated with the shift of the optical absorption edge toward lower energy as the crystal cools. Similar color changes occur in barium titanate, which is bright red at high temperature.

Using this technique, we grew square crystals of good quality, weighing from 4-10 grams. Two such crystals, with seeds still attached, are shown in Figs. 6 and 7. Figure 8 shows an assortment of cut and uncut samples. Cutting is readily accomplished

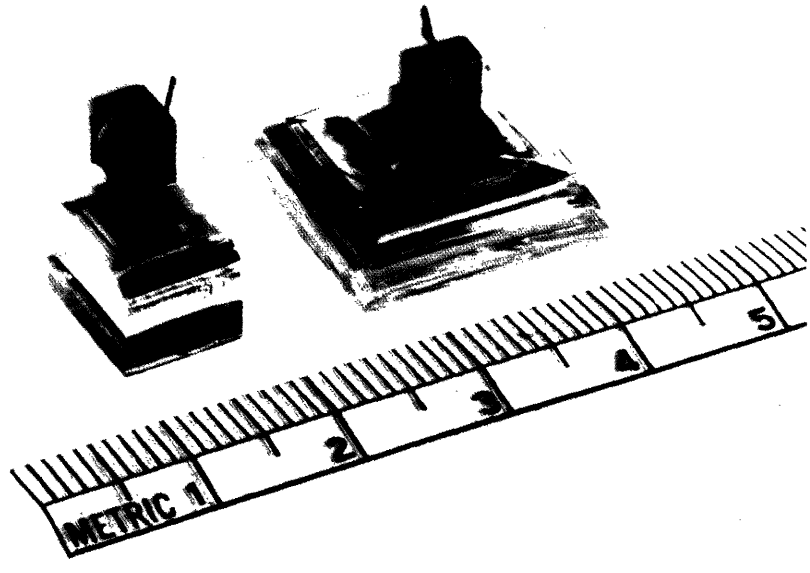

Fig. 6. Uncut $KTaO_3$ crystals.

with a diamond saw. The size, color, and electrical properties of these crystals depend on many growth parameters.

c. Parameters Affecting Crystal Quality

High-purity chemicals must be obtained. Our tantalum oxide was obtained from the Kawecki Chemical Company and from the Fansteel Metallurgical Company. Impurities

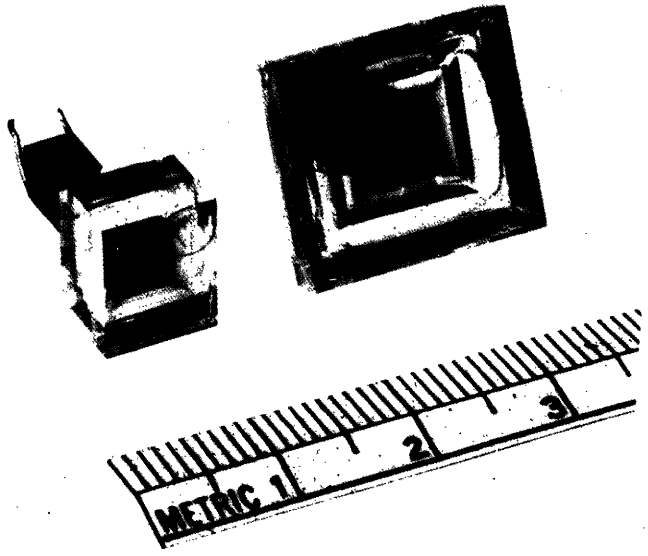

Fig. 7. Uncut $KTaO_3$ crystals.

such as Na and Nb must be avoided because they raise the Curie temperature. The calcium content must be less than ~50 ppm because calcium forms an immiscible compound that floats to the melt surface. This calcium layer prevents contact between

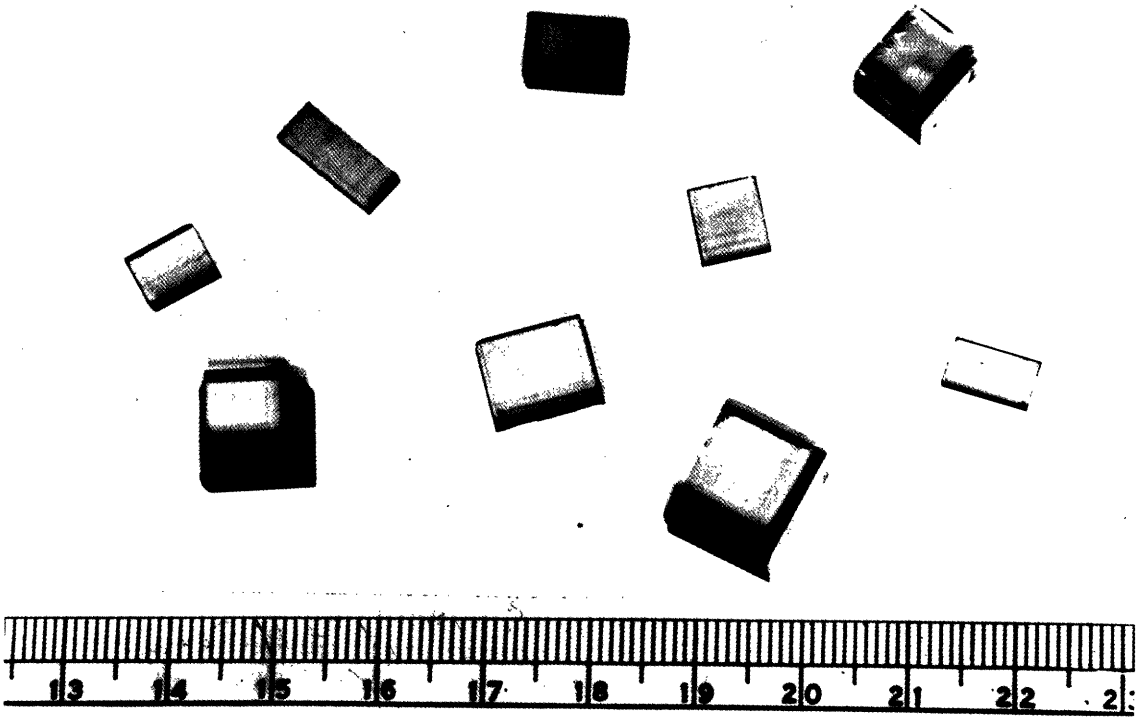

Fig. 8. Assorted cut and uncut crystals.

the test crystal and the rest of the melt and interferes with the liquidus temperature determination. Tin was another important impurity. The presence of ~300 ppm of added Sn produced colorless, high-resistivity (~10^{11} ohm cm) crystals, whereas low-Sn batches gave pale blue, low-resistivity (~1 ohm cm) crystals.

The color of the single crystals of $KTaO_3$ depended on the growth temperature, the tin concentration, and the furnace atmosphere, and varied from an opaque dark blue to colorless. Crystals grown in air without added tin were slightly reduced. They were blue and conducting. The parts of the crystal that grew first (at the highest temperatures) were dark blue and opaque, and the portions that grew last (at the lowest temperatures) were a transparent pale blue and were semiconducting. Addition of 300 ppm of Sn produced clear, insulating crystals. Tin-doped crystals grown in an oxygen atmosphere were transparent and colorless. It is interesting to note that blue crystals heated to 1250°C in oxygen were not oxidized but remained blue; therefore, the oxidizing effect of an oxygen atmosphere is not a consequence of diffusion into the newly grown $KTaO_3$ crystal but is probably a result of the presence of dissolved oxygen in the melt. The results are all consistent with the assumption that the presence of conductivity and the color are caused by oxygen vacancies in the lattice, and that Sn^{4+} impurities act as electron traps. No crystals were grown in oxygen without tin doping.

d. Crystal Doping

Addition of magnetic impurities to $KTaO_3$ was accomplished by dissolving the appropriate oxides or carbonates in the melt. These were Fe_2O_3, MnO_2, $CoCO_3$, and Cr_2O_3. An unsuccessful attempt was made to introduce selected rare earths into the crystal. Gd_2O_3 was practically insoluble in the melt; the smallest speck merely floated on the surface. Eu_2O_3 was also insoluble. Tb_4O_7 dissolved readily but had a harmful effect on crystal growth. Concentrations as low as 50 ppm inhibited all crystallization.

IV. PROPERTIES OF $KTaO_3$

4.1 ELECTRICAL PROPERTIES

a. Dielectric Properties

The only published dielectric data obtained from reasonably pure single-crystal $KTaO_3$ were reported by Hulm, Matthais, and Long,[22] in 1950.

We measured the dielectric constant of single crystals grown in our laboratory. Some of these measurements were made by Suk Soo.[27] Dielectric constant vs temperature for undoped $KTaO_3$ is shown in Fig. 9. No significant change in dielectric constant over a frequency range from 100 cps to 200 kcps was observed.

Figure 10 shows our Curie-Weiss plots of $10^4/\chi$ against temperature, where χ is the dielectric susceptibility. No iron could be detected by chemical analysis of our undoped sample. The dotted curve was taken from Hulm's published data for undoped

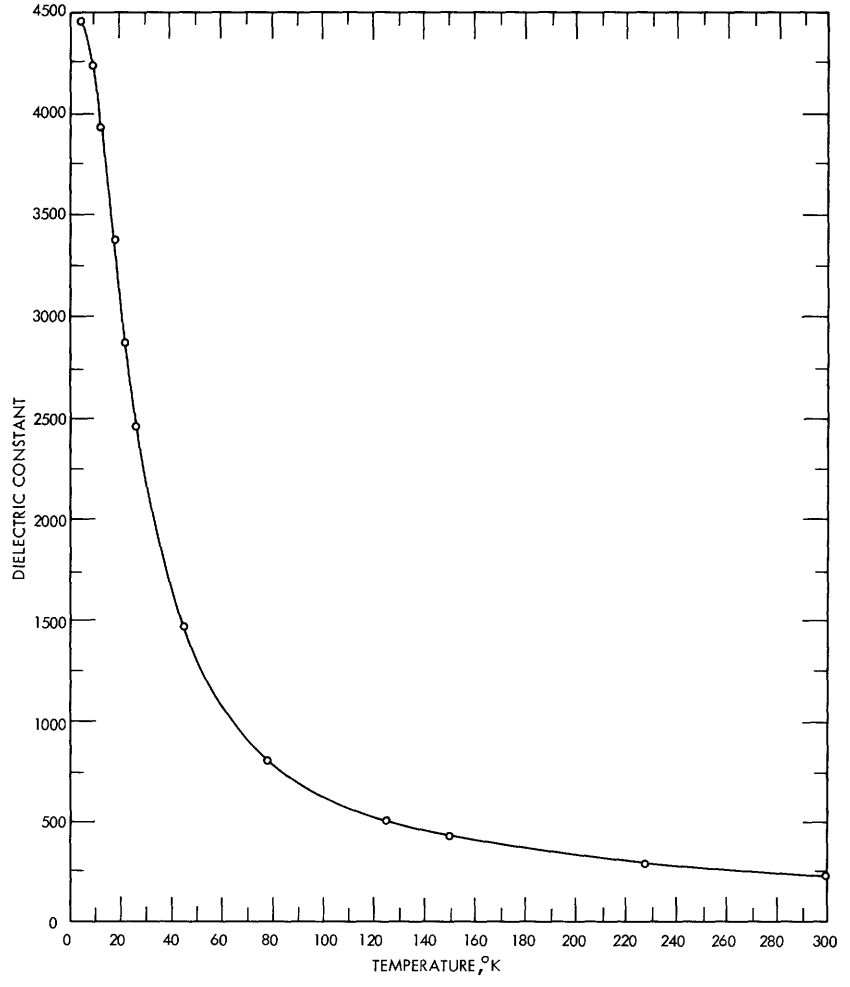

Fig. 9. Temperature dependence of dielectric constant for undoped $KTaO_3$ (200 kcps).

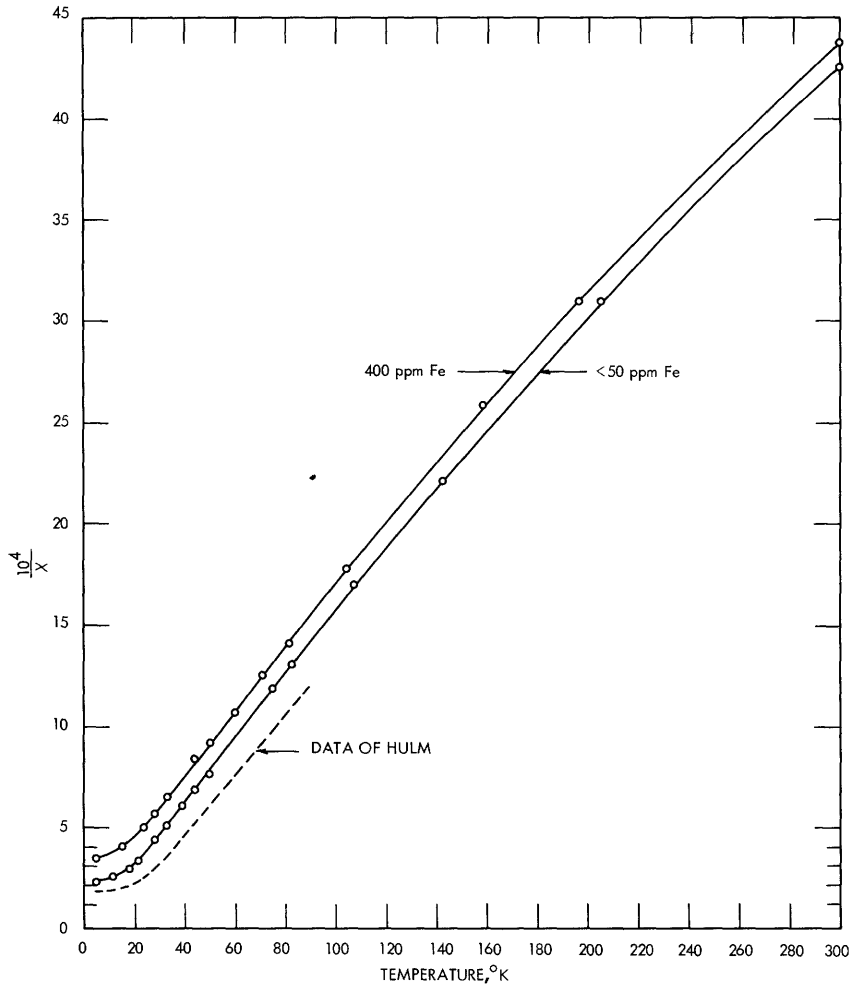

Fig. 10. Curie-Weiss plot for $KTaO_3$ (200 kcps).

$KTaO_3$. The Fe content lowered the Curie temperature; this finding is consistent with the data of Nishioka, Sekikawa and Owaki.[28] Between 30°K and 80°K the Curie-Weiss expression

$$\kappa = \frac{6.0 \times 10^4}{T - 1}$$

fits the data reasonably well for an undoped sample. Accordingly, the extrapolated Curie temperature (T_c) is 1°K. This is not in agreement with the 14°K reported by Hulm, Matthais, and Long. The difference is probably due to impurities in the earlier crystals.

Barrett[29] gave a theoretical discussion of deviations of dielectric constant from Curie-Weiss law behavior at low temperature. He assumed, after Slater,[30] that the B ion motion in an ABO_3 perovskite causes the high dielectric constant, and that the temperature dependence is associated with the anharmonicity of the potential well in which the B ion is situated. Barrett then calculated the relevant energy levels, took a Boltzmann average, and obtained

$$1/\chi = \frac{T_1 \coth (T_1/2T) - 2T_c}{2M},$$

where T_1 and M are theoretical parameters. Below T_1, quantum effects become important and deviations occur. The curvature of $1/\chi$ versus T is positive at low temperatures and agrees with our observations. The same effect has been observed[29] in $SrTiO_3$ below 40°K. For $T \gg T_1$, this expression reduces to the Curie-Weiss law. Other

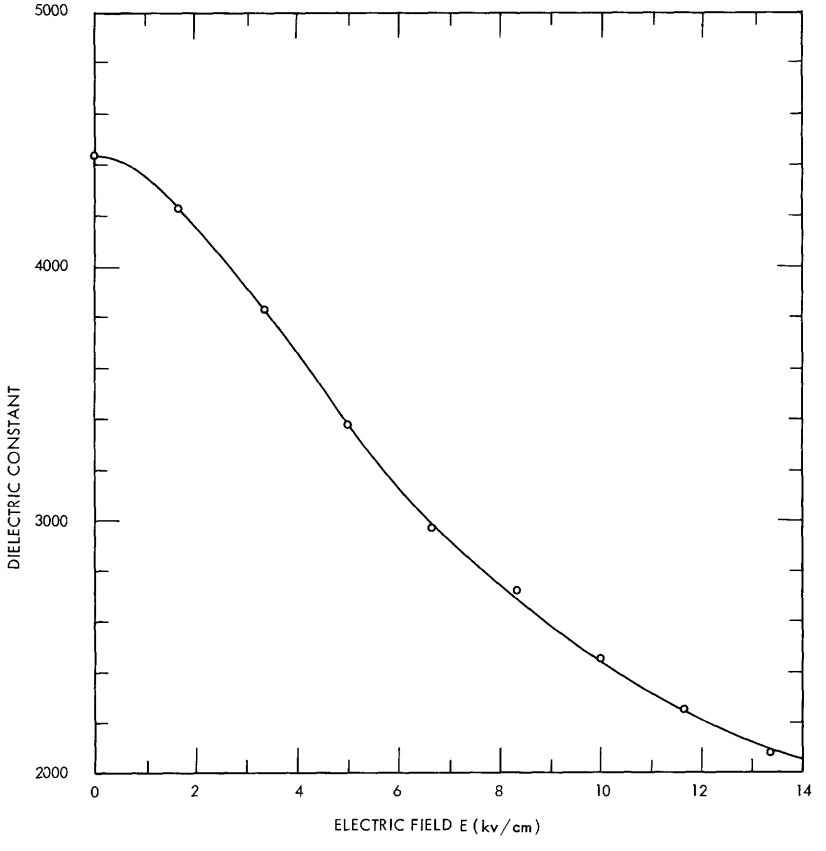

Fig. 11. Effect of DC biasing field on small-signal dielectric constant for an undoped sample at 4.2°K.

discussions of deviations from the Curie-Weiss law behavior have been given by Megaw,[11] Känzig,[10] and Cochran.[31]

In order to determine the magnitude of the polarization in $KTaO_3$, we have examined the effect of an applied DC electric field on the small-signal dielectric constant. Experimental points are shown in Fig. 11 for the undoped sample at 4.2°K. The corresponding P vs E expression calculated from $P = \epsilon_o \int \kappa \, dE$ is plotted in Fig. 12. A slight saturation of the polarization is evident. The saturation polarization of $KTaO_3$ is clearly greater than 4 μcoulombs/cm^2.

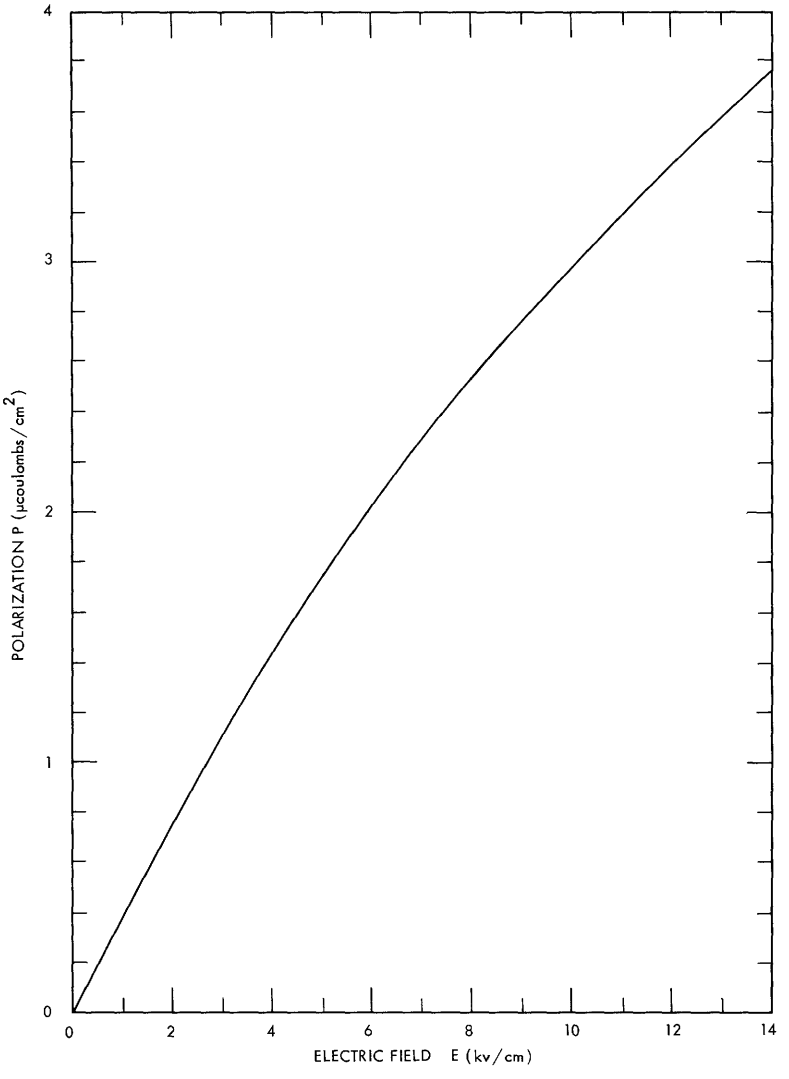

Fig. 12. Lattice polarization vs field strength for an undoped sample at 4.2°K.

b. Loss Properties

The loss tangent at room temperature (measured at 200 kcps) was 0.001. Low-temperature measurements were erratic and nonreproducible, because of condensed air or water vapor in the crystal holder.

We used dielectric resonator techniques[32] to measure the loss at microwave frequencies. The Q values are shown in Table III. The impurity concentration was approximately 0.02 mole per cent in the doped samples. Table III also shows an increase in loss with operating frequency. Rupprecht and Bell[33] and Silverman[34] reported a linear increase in loss tangent for $SrTiO_3$.

c. Electrical Conductivity

Two-terminal resistivity measurements with an electrometer (General Radio) indicate that the room-temperature DC resistivity of a "nonconducting" crystal is approximately

Table III. Microwave Q of doped and undoped samples of $KTaO_3$.

Sample	Frequency (Gc)	Loaded Q	Temperature (°K)
Undoped	9.0	≈1000	300
(air-grown)	9.0	≈10000	4.2
Fe-doped	11.97	1100	300
(air- or oxygen-grown)	8.39	1400	300
	9.0	≈9000	4.2
Mn-doped	11.72	780	300
(oxygen-grown)	8.83	1100	300
	9.0	≈9000	4.2
Mn-doped	9.0	200-400	300
(air-grown)	9.0	≈1000	4.2
Co-doped	11.31	440	300
(oxygen-grown)	8.41	420	300
	9.0	≈1000	4.2
Cr-doped	8.87	≈200	300
(air-grown)			

10^{11} ohm cm. For a discussion of highly conducting crystals, see Section X.

d. Pressure-Generated Current

Application of very light pressure (~10-100 grams per cm^2) to a nonconducting $KTaO_3$ crystal that has fired-on silver electrodes generates a small conductivity (~20 μamps with an ohmmeter). This current decays if the pressure is maintained. Removal of the pressure produces a current having the same sign.

4.2 OTHER PROPERTIES

High-resistivity, single-crystal, undoped $KTaO_3$ is transparent and colorless; however, the undoped crystals grown in air are blue rather than colorless. The color has been attributed to free-carrier absorption in the red and infrared where the free carriers are associated with donor centers produced by slight crystal reduction.

The refractive index of $KTaO_3$ has been estimated by measuring the apparent thickness of a sample with a microscope. The result is 2.3 ± 0.1. This is an average over the visible spectrum.

No measurements of thermal properties were made, except to note that crystals can be inserted into a furnace at 1230°C without cracking and can also be put directly into liquid helium from room temperature.

These crystals have the hardness of quartz and are readily cut with a diamond saw. They cut glass and are in turn cut by quartz. They cleave well along [100] planes.

$KTaO_3$ is slowly etched by dilute HF but seems to be unaffected by HCl, HNO_3, or H_2SO_4.

Vousden[35] used power x-ray techniques to measure the lattice constant of $KTaO_3$, and reported a value of 3.989 Å. He also established the fact that the structure of $KTaO_3$ is cubic perovskite at room temperature. We made similar x-ray studies on our crystals and we also measured a lattice constant of 3.989 Å.

V. OPTICAL ABSORPTION SPECTRA

5.1 INTRODUCTION

Optical absorption data contribute to an understanding of transition metal impurities. Unfortunately, only a limited amount of information can be obtained from optical data in doped $KTaO_3$ because a host lattice absorption edge masks the higher energy bands that we need in order to interpret the iron-group ion data. Narrow fluorescent bands, which we might use to identify ions, were not observed.

As shown in Fig. 13, the optical absorption edge for "pure" $KTaO_3$ at room temperature is ~0.35 microns, which gives a band gap of 3.5 ev, and this edge moves toward higher energies at low temperatures, as expected. No additional bands were found out to 3 microns, except for a sharp band near 2.8 microns. We have associated this absorption with O-H bonds in the lattice. (See Section XI.) This effect was also observed in the doped samples.

Beyond 3 microns, the undoped crystal remained relatively transparent until the first infrared lattice band was approached (near 6 microns).

All optical absorption data were obtained on a Beckman Model DK-1 spectrophotometer provided by the Laboratory for Insulation Research, M. I. T. We made optical absorption measurements from 0.3 microns to 3 microns at room temperature and at liquid-nitrogen temperature.

Griffith and Jorgensen have discussed many theoretical problems connected with

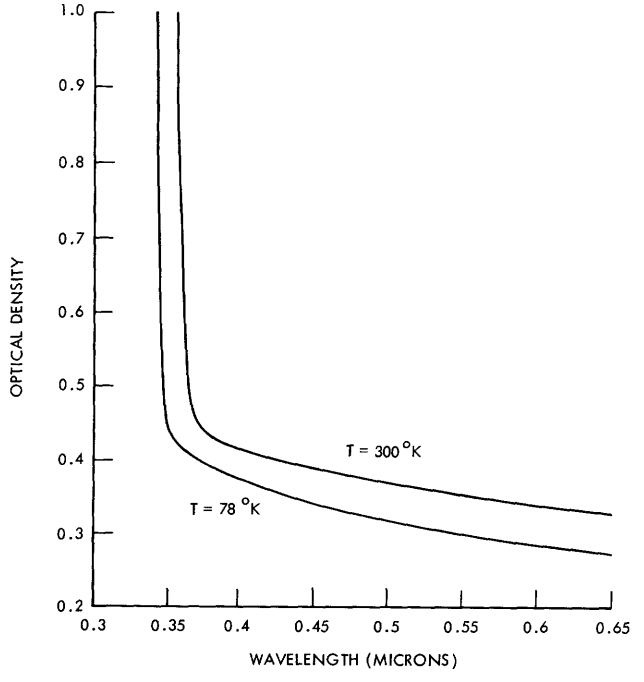

Fig. 13. Optical absorption of undoped $KTaO_3$.

the optical spectra of iron-group ions in crystals. Tanabe and Sugano[36] calculated energy-level spacings for the iron-group ions ($3d^n$ configuration only) in octahedral symmetry. Their results, as taken from Griffith,[37] are reproduced in Fig. 14. These curves are for assumed values of $\gamma = C/B$, where B and C are parameters connected

Table IV. Orbital degeneracy and group theoretical notation.

Mulliken	Bethe	Orbital degeneracy
A_1	Γ_1	1
A_2	Γ_2	1
E	Γ_3	2
T_1	Γ_4	3
T_2	Γ_5	3

with repulsion between electrons. The vertical scale in Fig. 14 is E/B, where E is the actual energy, and the horizontal scale is 10 Dq/B, where Dq is a crystal field parameter. The notation is that of Mulliken.[38] Orbital degeneracies of the levels and the corresponding Bethe[39] notation are given in Table IV.

5.2 OPTICAL ABSORPTION IN Fe-DOPED $KTaO_3$

The Fe-doped $KTaO_3$ crystal that we used for all of our optical measurements was grown in an oxygen atmosphere from a melt containing 20 mg of Fe_2O_3 per 70 grams of Ta_2O_5. This corresponds to approximately 800 ppm Fe. A smaller fraction of the iron entered the crystal, however. Chemical analysis of a crystal grown from a melt containing 1800 ppm Fe indicated that there were only 400 ppm in the final crystal. Chemical analyses were performed by D. Guernsey, Analytical Laboratory of the Department of Metallurgy, M.I.T. We assumed that the same ratio applied to the 800-ppm melt, and concluded that the crystal contained approximately 0.02 mole per cent iron. This crystal is pale green-yellow, and is 8.48 mm thick.

Experimental curves of optical density vs wavelength are shown in Fig. 15. Comparison of Fig. 15 with Fig. 13 shows that the iron doping rounds off the crystal absorption edge and adds a weak shoulder on the low-temperature curve at approximately 0.48 micron (21,000 cm^{-1}). Unfortunately, as is often true for added iron, the optical data are not particularly informative. The source of the difficulty may be the strong absorption in the ultraviolet observed for Fe^{3+} by several investigators.[40-42]

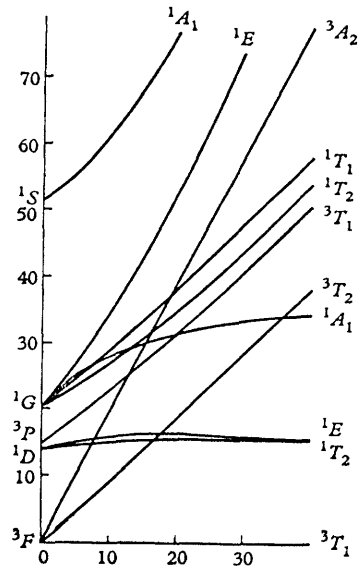

(a) d^2, V^{3+}, $\gamma = 4{\cdot}428$, $B = 860$ cm^{-1}.

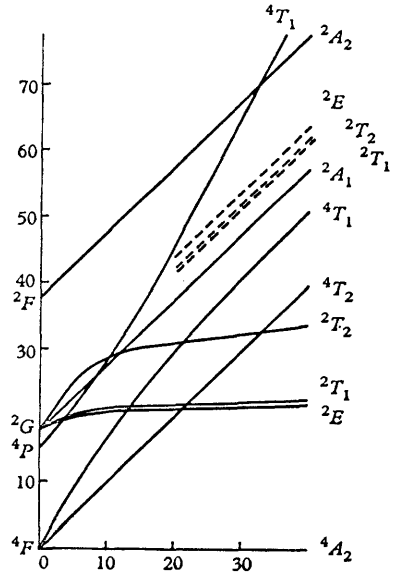

(b) d^3, Cr^{3+}, $\gamma = 4{\cdot}502$, $B = 918$ cm^{-1}.

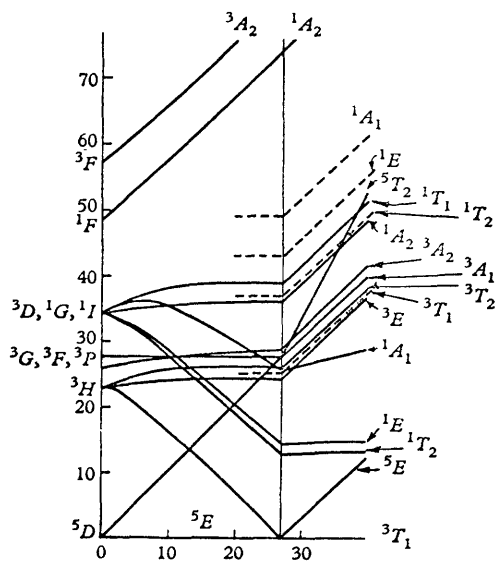

(c) d^4, Mn^{3+}, $\gamma = 4{\cdot}611$, $B = 965$ cm^{-1}.

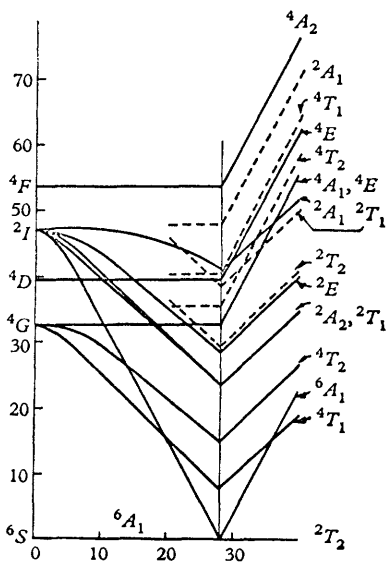

(d) d^5, Mn^{++}, $\gamma = 4{\cdot}477$, $B = 860$ cm^{-1}.

Fig. 9.2 For legend see over.

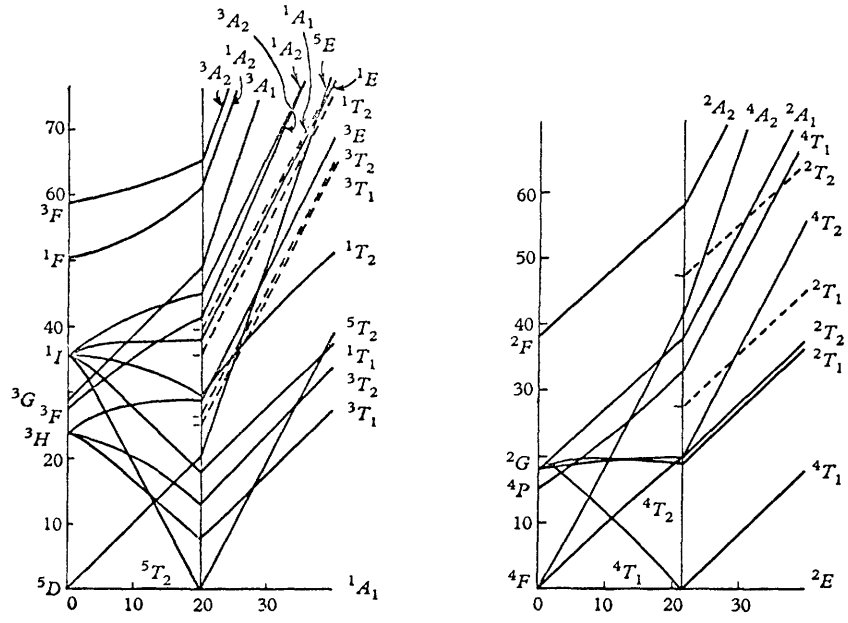

(*e*) d^6, Co^{3+}, $\gamma = 4{\cdot}808$, $B = 1{,}065$ cm^{-1}. (*f*) d^7, Co^{++}, $\gamma = 4{\cdot}633$, $B = 971$ cm^{-1}.

Figs. 9.2*a–f*. Energy plotted against Δ (both in units of B) for d^n ions, as calculated by Tanabe & Sugano (1954). The ion for which the calculation was actually made is shown in each case, together with their values for $\gamma = CB^{-1}$ and B. Except for d^2, not all the highly excited states are plotted.

Fig. 14. Iron-group energy level diagram (from J. S. Griffith, The Theory of Transition-Metal Ions, Cambridge University Press, 1961, pp. 261-262, with permission of the Cambridge University Press).

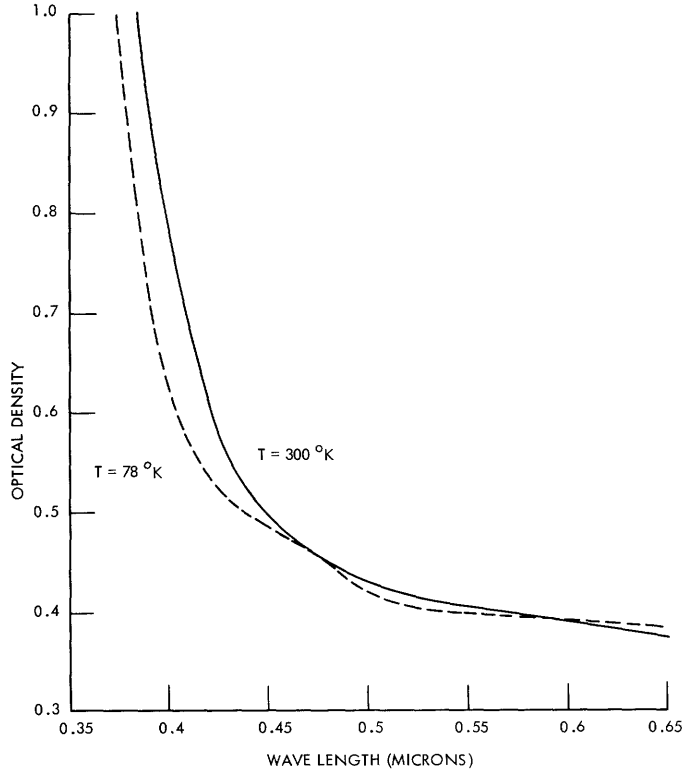

Fig. 15. Optical absorption of Fe-doped $KTaO_3$.

5.3 OPTICAL ABSORPTION IN Mn-DOPED $KTaO_3$

In contrast with the $KTaO_3$ crystals containing iron, the manganese-doped sample exhibited a well-resolved absorption peak separated from the $KTaO_3$ absorption edge

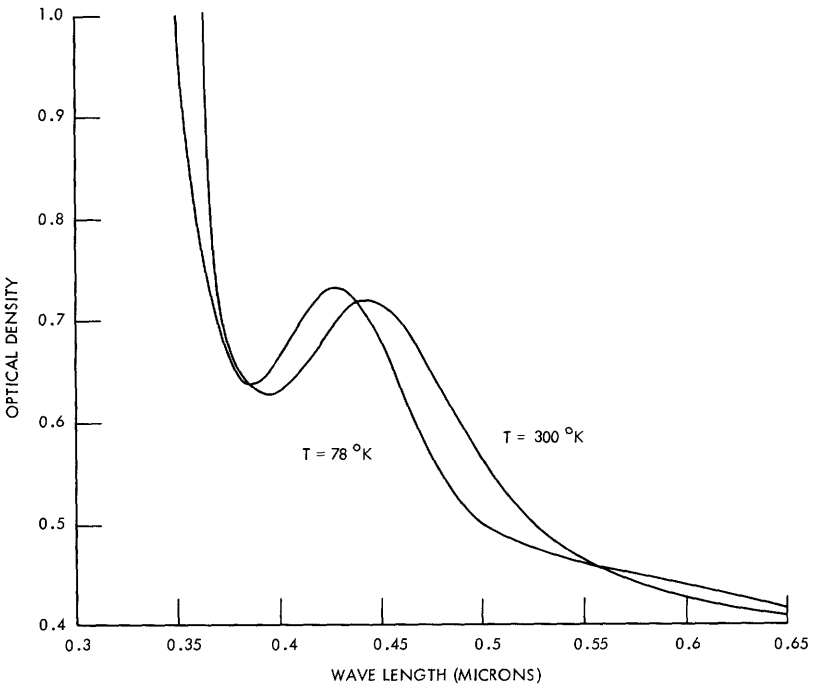

Fig. 16. Optical absorption of Mn-doped $KTaO_3$.

(Fig. 16). The crystal was 7.34 mm thick, and was grown in an oxygen atmosphere from a melt containing 24 mg MnO_2 per 70 grams of Ta_2O_5. We assumed the concentration was ~0.02 mole per cent. This crystal is pale yellow.

Table V. Optical absorption in Mn-doped $KTaO_3$.

Temperature (°K)	Absorption peak (cm^{-1})	Linewidth (cm^{-1})	Oscillator strength f
300	22,200	≈5000	$\approx 1.5 \times 10^{-4}$
78	23,000	≈4500	–

Figure 16 shows a curve of optical density vs wavelength for the sample. Table V gives the position of the absorption peak, linewidth, and oscillator strength taken from Fig. 16. The oscillator strength and linewidth are typical for 3d → 3d transitions.[37,40]

Unfortunately, a single absorption peak does not permit calculation of B and C, nor can we assign a valence state to the Mn ion from the position of one band. Several observations point, however, to $Mn^{4+}(3d^3)$ or $Mn^{5+}(3d^2)$:

(i) Mn-doped crystals grown in air rather than oxygen were a different color (pink); this indicates that air-grown crystals contain Mn in a lower valence state than the Mn ions in oxygen-grown crystals. The air-grown crystals lack a magnetic resonance at 4.2°K; this suggests that the ion is Mn^{3+} rather than Mn^{2+}. From these facts we conclude that Mn is tetravalent or higher in the yellow oxygen-grown samples.

(ii) Manganese is known to substitute in the perovskite $SrTiO_3$ as Mn^{4+}.

(iii) Mn^{4+} has[43] an absorption peak at 21,800 cm^{-1} in Al_2O_3, associated with the $4T_2 \rightarrow {}^4A_2$ transition (Fig. 14b); this is close to our observed value in $KTaO_3$. These observations do not rule out $Mn^{5+}(3d^2)$, although no optical data are available for this ion. The possibility of fluorescence exists for Mn^{4+} and has been observed in Al_2O_3 with Mn^{4+} by Geschwind, et al.[43] No fluorescence was observed with the unaided eye in our manganese-doped $KTaO_3$ when illuminated with an ultraviolet lamp.

5.4 OPTICAL ABSORPTION IN Co-DOPED $KTaO_3$

The single-crystal $KTaO_3$ containing cobalt was grown in an oxygen atmosphere from a melt containing 20 mg $CoCO_3$ per 70 grams of Ta_2O_5. The concentration is ~0.02 mole

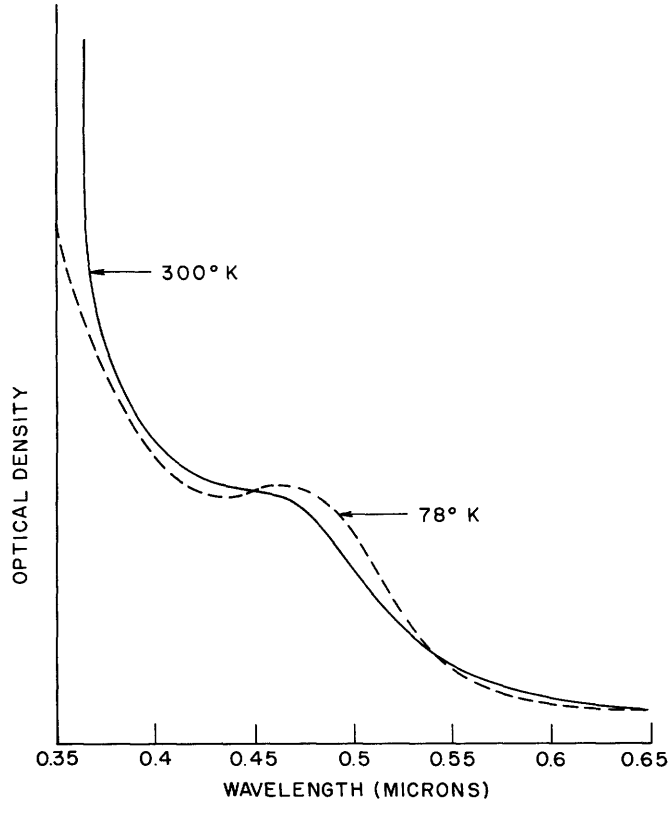

Fig. 17. Optical absorption of Co-doped $KTaO_3$.

per cent. The crystal is pale amber in color, and is 7.55 mm thick.

The optical absorption curve is shown in Fig. 17. A single absorption peak is resolved at 0.47 micron (21,300 cm^{-1}) at room temperature. Cooling to liquid-nitrogen temperature shifts the peak to 0.48 micron (20,800 cm^{-1}). Several considerations suggest that the Co^{3+} ion is present. (i) The Co^{2+} ion has usually been found in tetrahedral coordination. (ii) Co^{2+} usually has a band around 10,000 cm^{-1} in octahedral surroundings and all its transitions move to higher energy as the crystalline field increases during cooling. This can be seen from the positive slope of all the levels in the $3d^7$ energy-level diagram of Fig. 14f. (iii) Strong evidence for the presence of Co^{3+} was provided by the high-pressure experiments of Stephens and Drickamer[44] in K_3CoF_6. They found that the ground state is the ^5E (high-spin) state that can be seen at the left of the crossover point in the Tanabe and Sugano diagram of Fig. 14e. The $^5T_2 \rightarrow {}^5E$ transition occurs at 19,300 cm^{-1}. Application of hydrostatic pressure increased the energy-level spacing to 20,750 cm^{-1} at 150 kilobars. They predicted that crossover to the low-spin ground state ($^1A_1$) would occur at 220-250 kilobars, and the corresponding energy-level spacing would equal 21,300 cm^{-1}.

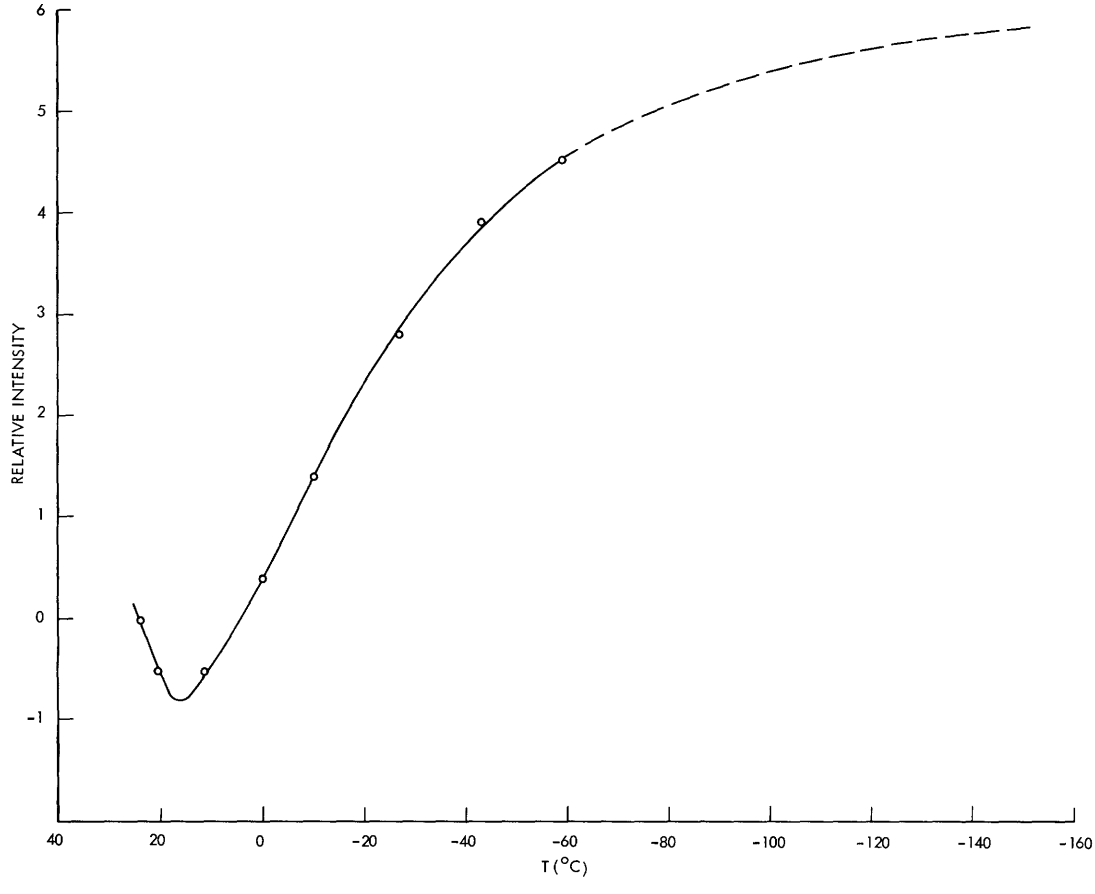

Fig. 18. Temperature dependence of optical absorption at 0.5 micron for Co-doped $KTaO_3$.

We observed an absorption peak at this frequency at room temperature in Co-doped $KTaO_3$ (Fig. 17). A proposed explanation for the absorption bands in Co-doped $KTaO_3$ is: At room temperature the strength of the crystalline field results in a high-spin state that is very slightly to the left of the crossover for the Co^{3+} ion. Cooling increases the crystal field as a result of lattice contraction, and the Co^{3+} ion shifts to the low-spin or strong-field state. The allowed transition changes from $^5E \rightarrow {}^5T_2$ to $^1T_1 \rightarrow {}^1A_1$, and the transition energy is reduced (see Fig. 14e). This would explain the shift of the absorption peak to longer wavelength at liquid-nitrogen temperature. In the neighborhood of crossover the energy-level positions may be altered somewhat by spin-orbit interaction and the possibility of local lattice distortion. Also, $^5T_2$ and $^1A_1$ states both may be populated. This fact and the overlap of the ^5E and $^1T_1$ levels could cause the absorption bands to move continuously from the high-spin to low-spin spacing as the crystal cools.

To check this observation, the crystal absorption at a fixed wavelength (0.5 micron) was measured as a function of temperature. The result is presented in Fig. 18. The curve tends to confirm this interpretation. These data were taken down to dry ice temperature. The dotted line is an extrapolation from absorption data obtained at liquid nitrogen temperature.

5.5 OPTICAL ABSORPTION IN Cr-DOPED $KTaO_3$

A crystal of $KTaO_3$ containing chromium was grown in air from a melt containing 25 mg of Cr_2O_3 per 70 grams of Ta_2O_5. No optical absorption spectra were observed and the crystal was colorless. The microwave Q is only 200 at room temperature, as compared with 1000 for undoped samples. The reason for this increased loss is not known.

VI. ELECTRON PARAMAGNETIC RESONANCE ABSORPTION SPECTRA

6.1 INTRODUCTION

EPR absorption spectra associated with Fe, Mn, Co, and Cr impurities in single-crystal $KTaO_3$ are presented and discussed in this section.

Because we are concerned with the presence of magnetic ions in the $KTaO_3$ host lattice, we ask: At what site does the impurity locate – interstitial or substitutional? What is its valence state and degree of covalency? What is the local symmetry at the impurity site, and how does this symmetry differ from that expected for the pure host crystal?

Simple ionic radii considerations suggest that iron-group ions should substitute at octahedrally coordinated B sites. A list of ionic radii is shown in Table VI. Since the

Table VI. Table of ionic radii, R.

Ion	R (Å)
Fe^{3+}	0.67
Cr^{3+}	0.65
Mn^{4+}	0.52
Mn^{2+}	0.91
Ti^{4+}	0.64

space available at B sites in the perovskites is between 0.6-0.7 Å, the "fit" for several of the iron-group ions appears to be quite good. Rare earths (~1.1 Å) would be expected to substitute in the larger A sites (~1.4 Å). Published EPR results confirm that iron-group ions do substitute at the B sites in $BaTiO_3$ and $SrTiO_3$. It should not be inferred from qualitative statements about "fit" that substitutional magnetic impurities leave the adjacent host lattice undisturbed. A valence difference between the impurity and the ion that it replaces may, for example, cause an oxygen vacancy to exist nearby, because of charge compensation. As a result, drastic symmetry changes can occur at the impurity site, and we cannot assume that EPR spectra will show the same symmetry as the bulk lattice. Even when no valence mismatch exists, local deviations from the bulk symmetry have been observed.[14] Certain valence states may show Jahn-Teller distortion. Published EPR results in $BaTiO_3$ and $SrTiO_3$ show that a substantial fraction of the Fe^{3+} ions added to the lattice can substitute in Ti^{4+} sites without altering the local symmetry, and that during polarization these sites are subject to local lattice distortions that are comparable with those expected for the bulk crystal.

All of our EPR spectra were observed at liquid-helium temperature only. No

magnetic resonances were observed at room temperature in any of the doped or undoped samples; this suggested that spin-lattice relaxation times are very short. No EPR were found in undoped crystals at either room temperature or 4.2°K, which confirms that magnetic resonances in the doped samples are associated with the intentionally added impurities.

6.2 EPR SPECTROMETER

The EPR spectrometer operates at X-band and is basically a conventional system employing 6-kc modulation of the magnetic field and phase-sensitive detection. The $KTaO_3$ crystals were used as dielectric resonators for all of our EPR spectra measurements. This host crystal has high-Q dielectric resonances. In a given crystal, most of the dielectric resonator modes had almost the same Q as that tabulated in Table III. That there were many modes is not surprising, especially at 4.2°K where the wavelength in the sample is less than 0.5 mm (X-band) and the crystal volume is at least 50 mm^3. We have not attempted to unravel these modes, but they are of rather high order at 4.2°K.

For the EPR measurements, the $KTaO_3$ crystal is mounted in polyfoam near the end of a shorted waveguide. The modulation of the magnetic field must penetrate to the crystal, however, and for this reason, the end portion of the waveguide was replaced by a quartz cylinder lined with a thin silver coating. The spatial variation of the RF field within the crystal is an important consideration for EPR measurements in which the dielectric resonator method is used. This influences line intensity through the variation of the angle between the RF field and the DC magnetic field and also affects line shape.

An electronic Smith Chart plotter which was available in our laboratory was inserted into the spectrometer system. This plotter is a superheterodyne system that employs two 30-mc IF strips and phase-sensitive detection. This equipment allows direct observation of crystal dielectric resonator modes as Q circles on the Smith Chart oscilloscope. A more important feature is the provision for separating the real (χ') and imaginary (χ'') parts of the paramagnetic susceptibility. This characteristic is particularly important in $KTaO_3$ because the χ'' signal is saturated at extremely low power levels (~0.1-0.01 μwatts). The different saturation behavior of the χ' and χ'' signals is a characteristic of inhomogeneously broadened EPR lines.[45-47]

The DC magnetic field was calibrated with a nuclear magnetic resonance probe. The uncertainty was ±2 at 1600 gauss, and ±10 at 3300 gauss. All EPR resonances were observed at a fixed microwave frequency by linearly sweeping the magnetic field.

Dielectric resonances were usually present over the frequency range of the klystron (8.2-9.6 Gc). Therefore, line position could be measured at several frequencies and the derivative of the magnetic field with respect to frequency could be determined.

Okaya and Barash[31] and also Carter and Okaya[48] used the dielectric resonator method to investigate EPR in rutile (TiO_2), and discussed the theory of such resonators.

6.3 EPR ABSORPTION IN Fe-DOPED $KTaO_3$

a. Introduction

The EPR spectra obtained from Fe-doped $KTaO_3$ were complicated by several factors.

1. Iron atoms substituted in the host crystal in at least two valence states.

2. The local crystal field symmetry at impurity ion sites was not the same for all ions, not even for those having the same valence.

3. Pronounced covalent effects were observed. In some cases, a superhyperfine structure associated with ligand nuclei (see Section VIII) was resolved.

4. The magnetic resonance lines were easily saturated and exhibited fast-passage effects that distorted the line shape and produced unusual dependence on modulation amplitude and power (see Section IX).

5. We observed a time dependence of the EPR spectrum. After nearly six months, certain EPR lines had disappeared. No effort was made to investigate this phenomenon. The original spectrum reappeared after one hour of ultraviolet irradiation with a mercury-arc lamp.

The EPR spectra were obtained from a $9.82 \times 5.26 \times 1.55$ mm^3 plate of Fe-doped $KTaO_3$ cut from a much larger sample. This crystal was grown in air. It contained

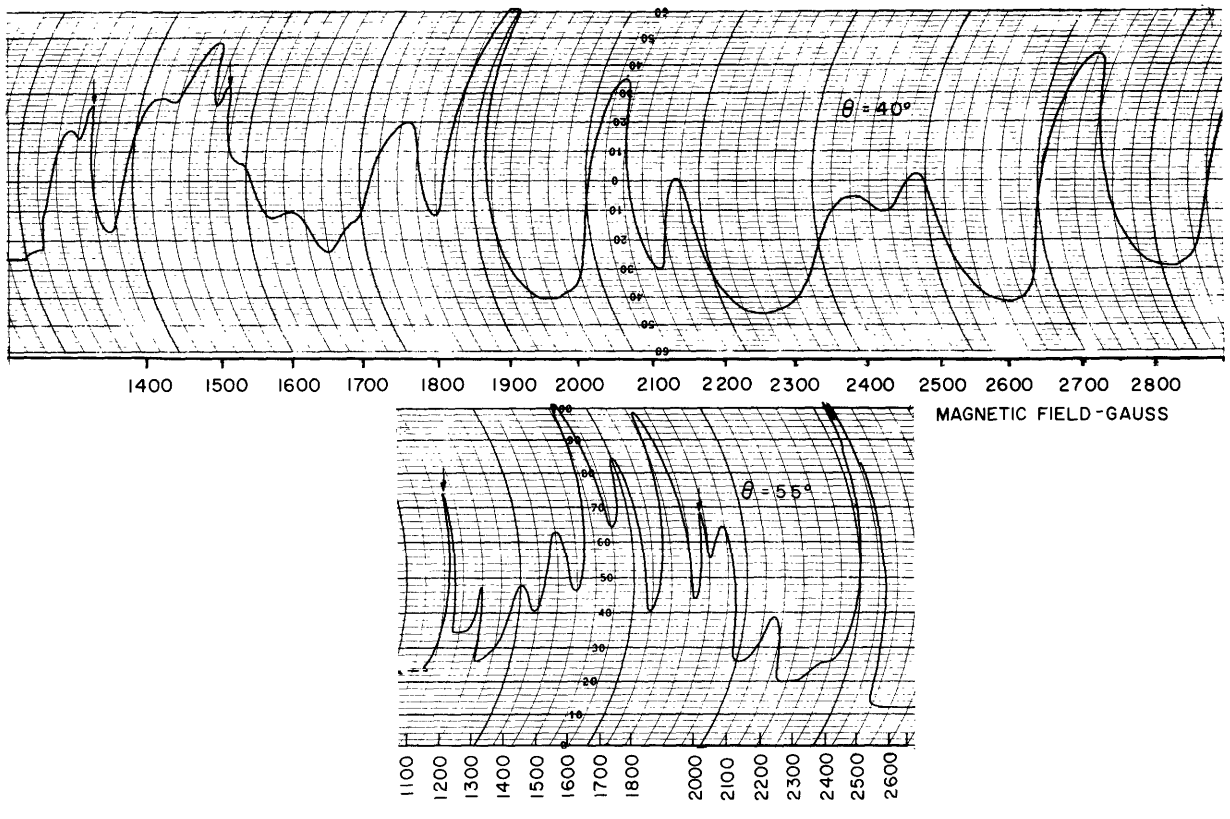

Fig. 19. Typical EPR for Fe-doped $KTaO_3$.

~0.02 mole per cent Fe. (Oxygen-grown crystals had the same spectra as those grown in air.) Unless the contrary is specifically stated, all magnetic resonances are associated with the dispersion or χ' portion of the total magnetic susceptibility $\chi = \chi' - j\chi''$. Except at very low power levels, χ'' was excessively saturated.

Approximately twenty resonance lines are visible at 4.2°K over a magnetic field range extending from 0 kG to 8 kG. Most of these lie between 1 kG and 5 kG. Two typical recorder traces of χ' over a portion of the field sweep are shown in Fig. 19. The lines are all one-sided and have linewidths of 50-100 gauss, except for three much narrower lines that are visible in the lower trace. In order to analyze the angular-dependence measurements, similar curves had to be taken at intervals of 1.25° because of the great number of lines, their widths, and their proximity.

b. Cubic Fe^{3+} Spectrum

We have associated one group of resonances with the Fe^{3+} ion situated in a cubic environment. Figure 20 shows these lines plotted against the angle of crystal rotation, θ,

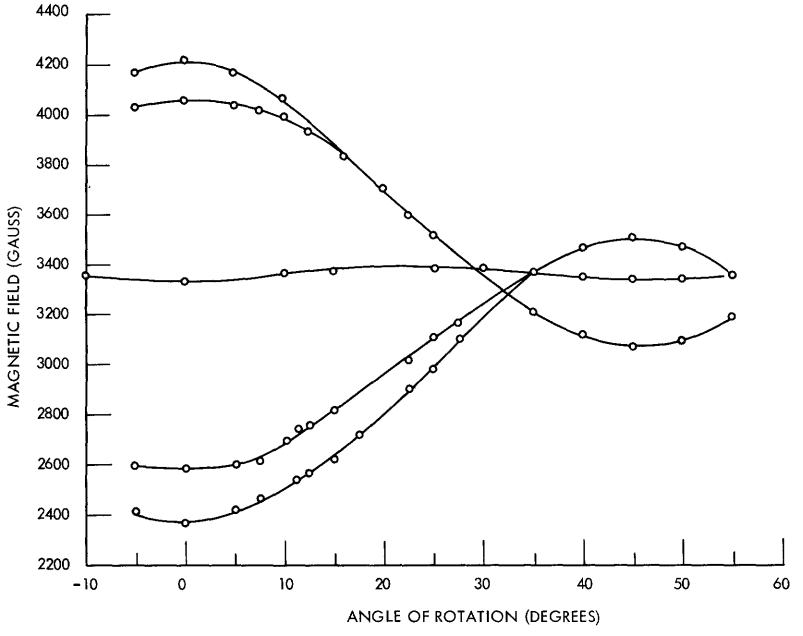

Fig. 20. Cubic Fe^{3+} spectrum. (9.277 Gc)

where θ is the angle between the DC magnetic field and a crystal [100] direction. At $\theta = 0°$, the DC magnetic field is along a cube edge and the axis of rotation is also a [100] direction. The line symmetry about 0° and 45° confirms cubic symmetry. Figure 21 shows representative recorder tracings for lines at $\theta = 0°$, 5°, and 45°. Arrows point to the cubic Fe^{3+} resonances.

The angular-dependence data plotted in Fig. 20 can be interpreted satisfactorily by

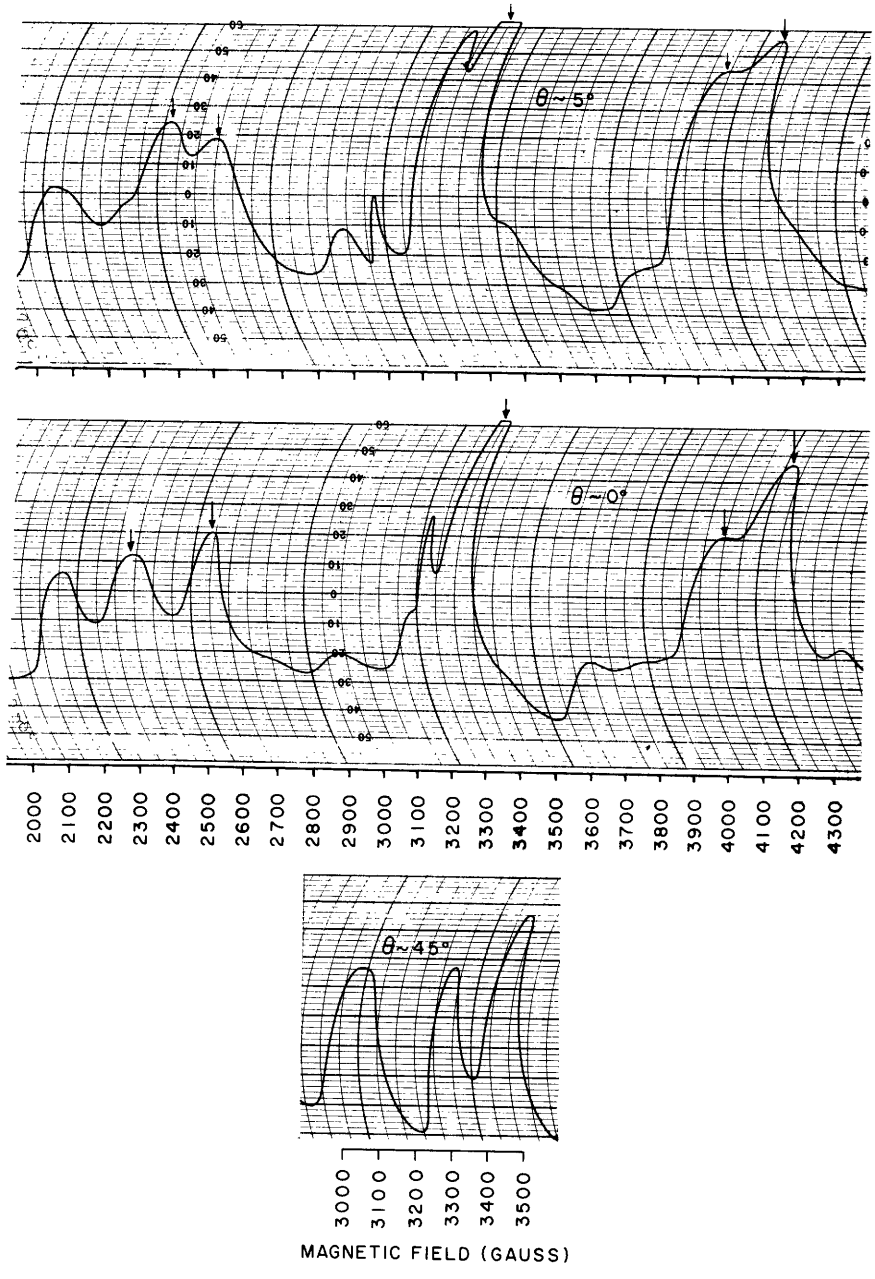

Fig. 21. Typical EPR for cubic Fe^{3+} (arrows).

making use of the cubic symmetry spin Hamiltonian for the $3d^5$ ion. This ion has a $^6A_1$ ground state (S=5/2). The appropriate spin Hamiltonian for this case has been discussed by Low,[49] Kronig and Bouwkamp,[50] Bleany and Stevens,[51] and others, and the equivalent spin operator is

$$\mathcal{H}_S = g\beta\bar{H}\cdot\bar{S} + \frac{a}{6}\left[S_x^4+S_y^4+S_z^4-\frac{1}{5}S(S+1)(3S^2+3S-1)\right],$$

where the splitting factor g is assumed to be isotropic and nearly equal to the free-spin value (2.0023), β is the Bohr magneton, and the zero-field splitting between the doublet and quartet is $|3a|$. We can make use of the published solutions to the 6×6 matrix for S = 5/2, given by Kronig and Bouwkamp and reproduced by Low. The solutions are power series that apply only if $\left|\frac{a}{g\beta H}\right| \ll 1$. The inequality is satisfied for this experiment. The energy levels (labeled by their strong-field quantum numbers) are

$$W_{\pm\frac{1}{2}} = \pm\ \beta H + \quad pa \pm \frac{5}{3}\phi(7-25\phi)\frac{a^2}{2\beta H} + \ldots$$

$$W_{\pm\frac{3}{2}} = \pm 3\beta H - \frac{3}{2}pa \pm \frac{5}{16}[1+\phi(22-75\phi)]\frac{a^2}{2\beta H} + \ldots$$

$$W_{\pm\frac{5}{2}} = \pm 5\beta H + \frac{1}{2}pa \pm \frac{5}{16}\left[1+\frac{1}{3}(50-113\phi)\right]\frac{a^2}{2\beta H} + \ldots, \qquad (1)$$

where $p = 1 - 5\phi$, $\phi = \ell^2m^2 + m^2n^2 + n^2\ell^2$, and ℓ, m, n are direction cosines relating the DC magnetic field direction to a [100] axis. If the rotation is in a crystal plane perpendicular to a cube edge, $\phi = \frac{\sin^2 2\theta}{4}$.

When $\theta = 0°$, the various allowed transitions with $\Delta m = \pm 1$ are given by the following expressions.

$$\frac{5}{2} \rightarrow \frac{3}{2} \qquad g\beta H = h\nu - 2a + \ldots$$

$$\frac{3}{2} \rightarrow \frac{1}{2} \qquad g\beta H = h\nu + \frac{5}{2}a - \frac{5}{16}\left(\frac{a^2}{2\beta H}\right) + \ldots$$

$$\frac{1}{2} \rightarrow -\frac{1}{2} \qquad g\beta H = h\nu + \ldots$$

$$-\frac{1}{2} \rightarrow -\frac{3}{2} \qquad g\beta H = h\nu - \frac{5}{2}a - \frac{5}{16}\left(\frac{a^2}{2\beta H}\right) + \ldots$$

$$-\frac{3}{2} \rightarrow -\frac{5}{2} \qquad g\beta H = h\nu + 2a + \ldots. \qquad (2)$$

When $\theta = 45°$, p = −0.25. Then the transitions are given by

$$\frac{5}{2} \rightarrow \frac{3}{2} \qquad g\beta H = h\nu - \frac{1}{2}a - \frac{5}{16}\left(\frac{a^2}{2\beta H}\right) + \ldots$$

$$\frac{3}{2} \rightarrow \frac{1}{2} \qquad g\beta H = h\nu + \frac{5}{8}a - \left(\frac{15}{16}\right)^2\left(\frac{a^2}{2\beta H}\right) + \ldots$$

$$\frac{1}{2} \rightarrow -\frac{1}{2} \qquad g\beta H = h\nu + \frac{5}{8}\left(\frac{a^2}{2\beta H}\right) + \ldots$$

$$-\frac{1}{2} \rightarrow -\frac{3}{2} \qquad g\beta H = h\nu - \frac{5}{8}a - \left(\frac{15}{16}\right)^2\left(\frac{a^2}{2\beta H}\right) + \ldots$$

$$-\frac{3}{2} \rightarrow -\frac{5}{2} \qquad g\beta H = h\nu + \frac{1}{2}a - \frac{5}{16}\left(\frac{a^2}{2\beta H}\right) + \ldots . \qquad (3)$$

The slight, second-order, angular dependence of the $\frac{1}{2} \rightarrow -\frac{1}{2}$ transition exhibits a maximum at $p = \frac{7}{50}$ and $\theta = 24°$ with a total spread of $\frac{49}{30}\left(\frac{a^2}{2\beta H}\right)$ according to Eq. 1.

Equations 1-3 predict the main features illustrated in Fig. 20. For $\theta = 0°$ (Eq. 2), a central $\frac{1}{2} \rightarrow -\frac{1}{2}$ transition is expected with two satellite pairs at approximately $\pm 2a$ and $\pm\frac{5}{2}a$ on either side. The second-order term reduces the separation between the high-field pair and increases that between the low-field pair. Since the total spread is $|5a|$, and the separation between the inner satellites is $|4a|$, we can obtain $|a|$ from Fig. 20. Both measurements give $|a| = 370 \pm 10$ gauss (345×10^{-4} cm^{-1}). The sign of a was not determined, although theory suggests that $a > 0$, and this has been confirmed by experiments obtained with other host lattices.[15-17] The splitting factor g can be obtained from the position of the $\frac{1}{2} \rightarrow -\frac{1}{2}$ transition at 0° by the substitution of f = 9.277 Gc and H = 3335 ± 20 gauss in $g = 714\,\frac{f}{H}$, which gives g = 1.99 ± 0.01. We then have $\left|\frac{a}{g\beta H}\right| = 0.11 \ll 1$ as required. The second-order correction $\left(\frac{a^2}{2\beta H}\right)$ is 41 gauss. Higher order terms, which have been neglected, are proportional to $\frac{a^3}{(2\beta H)^2}$ (< 4 gauss).

If we substitute these values of $|a|$, g, and $\frac{a^2}{2\beta H}$ in Eq. 3, resonances are predicted at 3530, 3510, 3140, and 3070 gauss for $\theta = 45°$. These calculated fields are in good agreement with Fig. 20. Examination of the $\theta = 45°$ recorder tracing of Fig. 21 shows that the high-field pair is not resolved, whereas slight broadening of the low-field pair is evident. This is consistent with the calculated resonance fields, which are only 20 gauss apart for the high-field lines, and 70 gauss apart for the low-field lines.

Most of the angular dependence is contained in the p parameter of Eq. 1, where $p = 1 - \frac{5}{4}\sin^2 2\theta$. Resonances should, therefore, coalesce at approximately 32°, as observed. The total calculated spread of the $\frac{1}{2} \rightarrow -\frac{1}{2}$ transition is 67 gauss, which is also in good agreement with Fig. 20. Less satisfactory agreement is obtained for the unequal spacings between pairs of satellite lines at $\theta = 0°$. The measured value of this separation difference is 60 ± 20 gauss, whereas the calculated value, from Eq. 2, is 26 ± 2 gauss.

The relative intensities of the Fe^{3+} resonances are expected to be proportional to (S-M)(S+M+1), or 8:5:9:5:8. Dobrov, Vieth, and Browne[15] observed intensity discrepancies in $SrTiO_3$ with Fe^{3+}. It is not clear from Fig. 21 whether similar deviations occur in $KTaO_3$.

It is instructive to compare our EPR results in $KTaO_3$ containing Fe^{3+} with similar observations made in the perovskites $SrTiO_3$ and $BaTiO_3$ and also in cubic MgO and CaO. Table VII gives values of a and g for each host lattice, the temperature of observation, and the room-temperature lattice constant a_o.

Table VII. Values of a and g for cubic Fe^{3+} ions.

Host lattice	a (cm^{-1})	g	T (°K)	a_o (Å)	Reference
$KTaO_3$	$(345\pm10)\times10^{-4}$	1.99 ±.01	4.2	3.99	–
$SrTiO_3$	+226 ±2	2.00	4.2	3.90	15,16
	+198 ±1	2.00	300	–	–
$BaTiO_3$	+100	2.00	>393	4.00	9
MgO	+205	2.00	300	4.20	52,49
CaO	+64	2.00	77	4.80	52

Table VII indicates that the splitting factor g in each of the crystals is close to the free-spin value (2.0023). A more interesting result is the variation of the cubic splitting parameter, a. Clearly, it is not simply related to the lattice constant. The observed value for a in $KTaO_3$ is the largest reported thus far.

c. Axial Fe^{3+} Spectrum

Three narrow lines (~20 gauss wide) are visible in the recorder tracing of Fig. 19. Also, a narrow line can be seen splitting off from the strong central resonance of Fig. 21. We have associated these resonances with Fe^{3+} ions in a crystal field of strong axial symmetry. A plot of line position against angle of rotation is shown in Fig. 22. Each of the three curves is for one of three mutually perpendicular axial crystal field directions. The plane of rotation of the crystal was ~27° from the [100] plane and caused the asymmetrical curves. At 90°, the DC magnetic field is perpendicular to two of the cube [100] edges and parallel to the other. This explains the observed double line. We concluded that the axial-field distortions are associated with each Fe^{3+} ion, rather than with random orientations of macroscopic domains within the crystal because the presence of Fe^{3+} ions in cubic symmetry (section 6.3b) suggests that the bulk crystal is

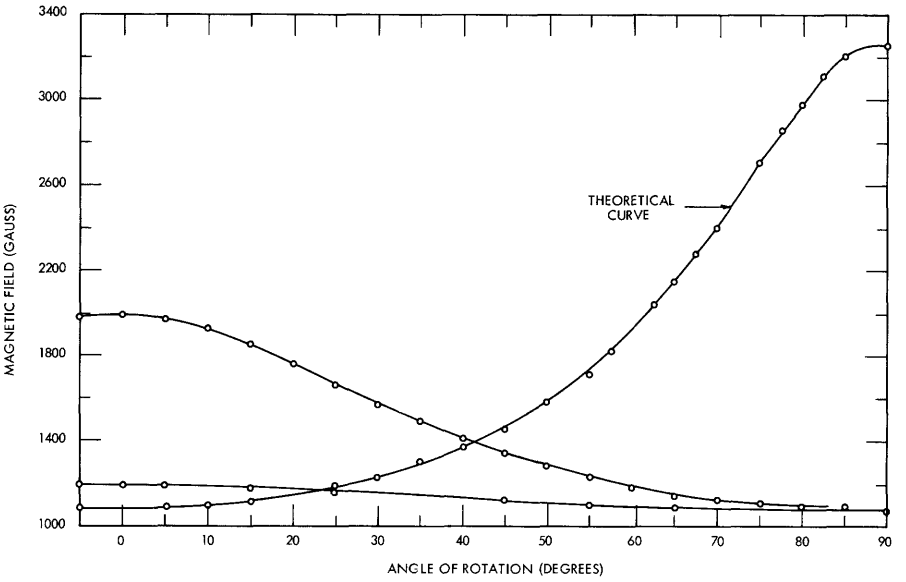

Fig. 22. Axial Fe^{3+} spectrum. Crystal plane of rotation ~27° from [100]. (9.158 Gc)

cubic. This conclusion is consistent with the fact that our observations were made above the Curie temperature.

Table VIII shows the 90° line positions and the measured values of g at two frequencies. Measured slopes of the Zeeman levels are also given. The line positions and

Table VIII. Line positions for axial Fe^{3+} spectrum.

Frequency (Gc)	DC field (gauss)	$g_{\parallel}$	$g_{\perp}$
9.504	1122 ±5		6.03±.02
8.787	1037 ±5		6.04±.02
.717	85 ±5		6.0 ±.3
9.504	3320 ±20	2.04±.02	
8.787	3071 ±20	2.04±.02	
.717	249 ±10	2.05±.1	

their slopes correspond to g factors of 6.0 and 2.0. We are therefore dealing with a Kramers doublet, with $g_{\perp} = 6.0$ and $g_{\parallel} = 2.0$. The identification of these values of g with Fe^{3+} (S=5/2) is straightforward. The axial spin Hamiltonian is

$$\mathcal{H} = g\beta H \cdot S + D\left[S_z^2 - \frac{1}{3}S(S+1)\right].$$

We assume that the g factor is isotropic, and that the distortion axis is along the z direction. If $D \gg g\beta H > 0$, the lower doublet is the $\frac{1}{2} \rightarrow -\frac{1}{2}$ transition. In the Appendix we show that this transition is given by

$$h\nu = g'\beta H,$$

where

$$g' = \left[g_{\parallel}^2 \cos^2\theta + g_{\perp}^2 \sin^2\theta \right]^{1/2}$$

and

$$g_{\parallel} = g \sim 2.0$$

$$g_{\perp} = 3g \sim 6.0. \qquad (4)$$

Here, θ is the angle between the DC field and the z axis. Equations 4 are plotted as the theoretical curve in Fig. 22. The 27° tilt of the crystal did not affect the angular dependence of this particular line because its crystal field was in the plane of rotation.

An approximate lower bound to D can be estimated by writing a series expansion for $g_{\perp}$ in powers of $\frac{g\beta H}{D}$. In the Appendix it is shown that

$$g_{\perp} = 3g \left[1 - \frac{23}{288} \left(\frac{g\beta H}{D} \right)^2 + \ldots \right].$$

The correction term in this equation is negligible because the measured value of $g_{\perp}$ is approximately 6.00, or 3g. If we conservatively estimate that $3g - g_{\perp} < 0.05$, the minimum value of D is calculated to be approximately 0.5 cm^{-1}. Because no transitions were observed between doublets, the actual value of D is probably much greater than this estimate.

The axial distortion that produces this large D term is almost certainly associated with a nearest-neighbor $O^{=}$ vacancy. Such a vacancy would provide charge compensation for a Fe^{3+} ion situated in a Ta^{5+} site. The claim for a nearest-neighbor vacancy is supported both by the observed distortion direction (along the three perpendicular axes between the tantalum and the oxygens) and by the narrow linewidth. The linewidth is approximately 20 gauss for the axial case, as compared with nearly 60 gauss for the $\frac{1}{2} \rightarrow -\frac{1}{2}$ transition associated with cubic Fe^{3+}. If the linewidth is caused primarily by hyperfine interactions with the ligand nuclei, the narrower width would imply significantly altered wave functions. A drastic rearrangement of ions and a major change in the character of the bonding would be expected for a missing nearest-neighbor $O^{=}$ vacancy.

d. Axial Fe^{5+} Spectrum

We have associated three additional resonances in the iron-doped sample with the Fe^{5+} ion situated in a site exhibiting axial symmetry. Fe^{5+} is isoelectronic ($3d^3$) with

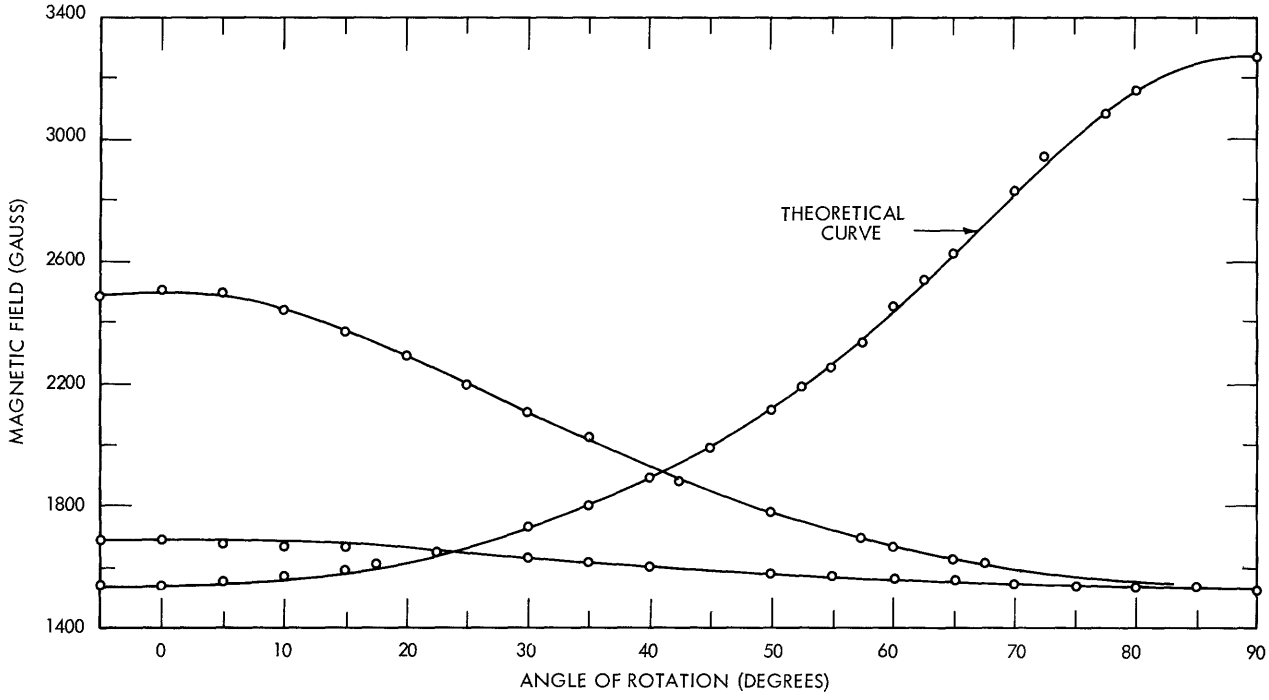

Fig. 23. Axial Fe^{5+} spectrum. Crystal plane of rotation ~27° from [100]. (9.158 Gc)

Cr^{3+} and Mn^{4+}. No previous observations of this ion have been published. A plot of line position against angle of crystal rotation is shown in Fig. 23. These data were obtained from a crystal tilted 27° with respect to a [100] lattice direction. At $\theta = 90°$, however, the tilt is no longer present, and the DC magnetic field lies along one of the three mutually perpendicular [100] axes. Under these conditions, we would expect two $g_\perp$ lines and one $g_{||}$ line, provided that the distortion axes and the [100] axes are coincident. According to Fig. 23 this is indeed the case, and we therefore conclude that the magnetic ions are subjected to axial local lattice distortions randomly distributed among the three [100] directions. There is a similarity between this spectrum and the axial Fe^{3+} spectrum of Fig. 22. In Table IX the positions of the two low magnetic field ($g_\perp$) lines, and also the slope of the associated Zeeman spacings are listed.

The origin of the axial distortion for the pentavalent Fe^{5+} ion in a Ta^{5+} site is not known. Müller[14] has reported the same effect for Mn^{4+} (also $3d^3$) in Ti^{4+} sites in

Table IX. Line positions for axial Fe^{5+} spectrum.

Frequency (Gc)	DC field (gauss)	$g_\perp$
9.504	1598 ±5	4.24 ±.01
8.787	1470 ±5	4.25 ±.01
.717	128 ±5	4.00 ±.15

$SrTiO_3$; the distortion may be related to the small size of these ions. From covalent bonding data (see Section VIII) we concluded that the Fe^{5+} ion is probably situated at the center of a cube formed by the eight next-nearest-neighbor K^+ ions. Apparently the axial distortion is associated with the O_6 oxygen octahedron. The high magnetic field ($g_{||}$) line is superimposed on the g = 2.0, $\frac{1}{2} \rightarrow -\frac{1}{2}$ transition associated with the cubic Fe^{3+} spectrum in Fig. 21 where a wide line can be seen separating off from the strong central resonance on the 5° tracing. Therefore the $g_{||}$ line could not be included in Table IX. In the lower recorder tracing of Fig. 19 the resonance at 2500 gauss is the same wide line at an angle of 55°. Fine structure is visible. (We discuss fine structure and covalent bonding effects in Section VIII.) The line intensities are independent of angle, and g~2.0. This suggests a $+\frac{1}{2} \rightarrow -\frac{1}{2}$ transition. A value of ~4 for $g_\perp$ (Table IX) tags the ion as $3d^3$. Therefore we associated the spectrum of Fig. 23 with $Fe^{5+}(3d^3)$.

To identify these spectra with Fe^{5+} (S=3/2), we start with the axial spin Hamiltonian

$$\mathcal{H} = g\beta H \cdot S + D\left[S_z^2 - \tfrac{1}{3}S(S+1)\right].$$

The matrix of this Hamiltonian within S = 3/2 is given for the Fe^{5+} ion in the Appendix. The following expressions have been derived, and apply if $D \gg g\beta H > 0$.

$$h\nu = g'\beta H,$$

where

$$g' = \left(g_{||}^2 \cos^2\theta + g_\perp^2 \sin^2\theta\right)^{1/2}$$

and

$$\begin{aligned} g_{||} &= g \sim 2.00 \\ g_\perp &= 2g \sim 4.00. \end{aligned} \qquad (5)$$

The measured value of $g_\perp$ is 4.24 (see Table IX) and gives $g_\perp > 2g_{||}$. We have, however, plotted a "theoretical" curve in Fig. 23 by substituting $g_{||} = 2.0$ and $g_\perp = 4.24$ in Eqs. 5, and the agreement with experimental data is excellent. If a finite D is allowed, the discrepancy between measured and calculated values of $g_\perp$ is even more pronounced. Geusic, Peter, and Schultz-DuBois[53] show that

$$g_\perp = 2g\left[1 - \frac{3}{16}\left(\frac{g\beta H}{D}\right)^2 + \ldots\right].$$

Clearly, the limiting value of $g_\perp$ is 2g or 4.00. It is interesting to note that in Table IX the slope of the Zeeman spacing, as determined from line positions at two different frequencies, is not 4.24 but is 4.0. The implication is either that the Zeeman levels start at H = 0 with a slope greater than 4.0 or there is a small zero-field splitting (~0.02 cm^{-1}). The latter is, of course, not permitted for a Kramers doublet. Before examining these

possibilities we should rule out several other interpretations of the spectrum.

When discussing axial Fe^{3+} we pointed out that $g_\perp \leq 6$ where

$$g_\perp = 3g\left(1 - \frac{23}{288}\left(\frac{g\beta H}{D}\right)^2 + \ldots\right). \tag{6}$$

An expression for the slope g_s can be obtained by differentiating Eq. 4. The result is

$$g_s = g_\perp - 3g\left(\frac{23}{144}\right)\left(\frac{g\beta H}{D}\right)^2 + \ldots . \tag{7}$$

Substituting $g_s = 4.0$, $g_\perp = 4.24$, and $3g \sim 6$ in Eq. 7 gives $\left(\frac{g\beta H}{D}\right)^2 \approx 0.25$. When this value is substituted in Eq. 6, the calculated $g_\perp$ is ~6 rather than 4. We conclude that the spectrum is not axial Fe^{3+} with an accidental $g_\perp$ of ~4. We can also discard ions of even valence (Fe^{2+}, Fe^{4+}, Fe^{6+}) because they have ground-state spin singlets in axial-field symmetry, and because the higher lying doublets require[48] that $g_\perp < g_{||}$.

The problem of explaining the observed $g_\perp = 4.24$ for a $3d^3(Fe^{5+})$ ion remains. Insufficient data were obtained to permit any definite conclusions. It would be desirable to examine EPR over a wide frequency range in order to obtain the Zeeman levels as a function of magnetic field. In particular, low-frequency data should determine how the levels approach degeneracy at zero field.

We conclude this discussion of the Fe^{5+} ion with the suggestion that the observed discrepancy between theory and experiment ($g_\perp > 2g_{||} > 4.0$) may result from covalent bonding effects. That covalent bonding is important for this ion is clearly revealed by a well-resolved superhyperfine interaction that involves the 8 next-nearest-neighbor potassium nuclei with spins of 3/2. Section VIII contains a thorough discussion of these data. Some molecular orbital calculations in conjunction with additional EPR data would be a suitable topic for further study.

e. Other Resonances

The Fe-doped $KTaO_3$ magnetic resonance spectrum exhibits many lines in addition to those which have already been associated with cubic Fe^{3+}, axial Fe^{3+}, and axial Fe^{5+}. Several of these are shown in Figs. 19 and 21. Intensities are comparable with those previously identified, and the linewidths vary between 50 gauss and 100 gauss. Angular-dependence data were obtained for many of these lines. These measurements were complicated by the number of lines, their overlap, and their intensity variations. It was not always possible to follow the resonances as they moved through one another even when we obtained spectra every 1.25°. Figure 24 shows the angular dependences of the stronger lines. Unconnected points are weak resonances which could not be followed with certainty. The line continuity indicated near M, J, H, and M' may be incorrect, although the separations at M and M' seemed to be real. Increased spectrometer sensitivity reveals many additional resonances that have not been investigated. Two curves in

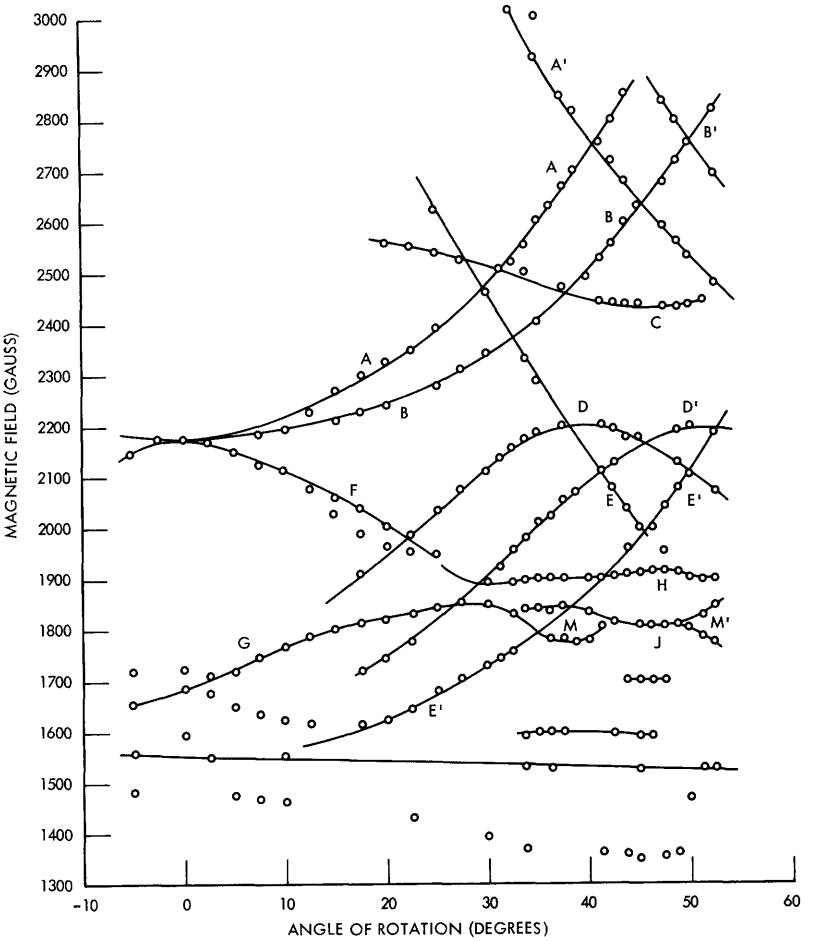

Fig. 24. Partial Fe^{3+} spectra. Crystal rotated about cube edge. (9.158 Gc)

Fig. 24 (E and E') are resonances that have already been associated with Fe^{5+} and will not concern us here.

The most striking feature of Fig. 24 is the presence of symmetry axes displaced approximately ±5° from 45° rotation. This is evident in curves A-A', B-B', D-D', and M-M'. Poor resolution apparently prevents observation of the minimum separation expected for the A and B curves near 0°. This multiply degenerate resonance at 0° is the low-field line in the two upper recorder tracings of Fig. 21. The magnetic field at resonance is 2180 gauss (9.158 Gc) which corresponds to g = 3.0. Measurements at two different frequencies (Table X) show that the slope is also 3.0 within the measurement accuracy. Table X suggests that the A, B, or F transitions at 0° are associated with a g = 3.0 Kramers doublet. It is instructive to compare the observed angular dependence of the A and B curves with

$$g' = \left(g_1^2\cos^2\theta + g_2^2\sin^2\theta\right)^{1/2},$$

where θ is the angle between the applied magnetic field and the local field symmetry axis. The subscripts refer to two perpendicular directions in the crystal. This equation applies in axial symmetry if the ground-state doublet lies considerably below all excited states.[50] If we take $g_1 = 3.0$, the value of g_2 is calculated to be 1.5. This calculation assumes that the A and A' or B and B' curves cross at $\theta = 45°$. (Note that this is not the θ of Fig. 24.) The value $g_2 = 1.5$ and the fact that $g_1 = 2g_2$ suggest that it might be worthwhile to continue the A and B curves out to 90°. There are two conceivable explanations for the observed g factors. The first is that g values close to 3.00 and 1.5 are merely accidental and involve a fortuitous mixing of spin and orbital states in an even electron system. The closeness of g_1 to 3.00 makes this difficult to accept. A second is the possibility of a double quantum jump associated with the Fe^{3+} ion. As shown previously, $g_\perp \sim 6.0$ for this ion when it is in a strong axial crystalline field. A double jump would then occur at an apparent g value of 3.0. Also, the observed $g_2 \sim 1.5$ would correspond to a g value of 3.0 for a true single quantum jump. This may be the F resonance (actually two separate lines) in Fig. 24. If this interpretation is correct, the $g_2 = 3.0$ (single quantum jump) is an accidental consequence of the angle between the distortion axis and the crystalline cubic axes, while the $g_1 = 3.0 = \frac{g_\perp}{2}$ (double quantum jump) implies that the magnetic field is perpendicular to the distortion axis for the A and B curves at $\theta = 0°$ in Fig. 24.

Table X. Line positions for g = 3.0 resonances in iron-doped $KTaO_3$.

Frequency (Gc)	DC field (gauss)	g
9.494	2251 ±20	3.0 ±.03
8.670	2060 ±20	3.0 ±.03
.824	191 ±20	3.1 ±.3

The presence of a double quantum jump may be related to the very high dielectric constant of $KTaO_3$ at 4.2°K. Nonlinearities in the dielectric behavior may generate sufficient field strength at the second harmonic of the X-band operating frequency to induce what appear to be double quantum jumps. The local distortion might enhance this effect in the immediate vicinity of the impurity ion. Perhaps a term of the form $E \cdot H$ or $P \cdot H$ is involved in the transition.

These considerations have not been examined in detail, although it is suggested that most of the resonances in Fig. 24 are associated with Fe^{3+} in a variety of local symmetries dictated by the position of a next-nearest-neighbor charge compensation $O^=$ vacancy and vacancies at more remote sites. Further study is clearly called for. Perhaps a higher operating frequency would lessen the difficulties caused by the proximity of all of the rather broad resonances. Unfortunately, the crystal Q is low at 25 Gc.

6.4 EPR ABSORPTION IN Mn-DOPED $KTaO_3$

At 4.2°K, the EPR spectrum consists of two resonances having the angular dependences shown in Fig. 25. The two lines merge at $\theta = 0°$, and one line is isotropic. This is clear evidence for axial symmetry with the distortion axes along each of the mutually perpendicular cube edge directions. In Fig. 25 an angle of rotation of 0° corresponds to 90° between the DC magnetic field and the distortion axis. The angular-dependent line loses signal intensity rather rapidly and falls below the noise level at approximately 24°. In the right-hand tracing of Fig. 26 the linewidth is 160 gauss, and a poorly resolved fine structure is evident on the top. The left-hand tracing of Fig. 26 is on an expanded scale and shows that this structure contains six lines separated by approximately 28 gauss. These six lines are the expected hyperfine structure associated with the spin 5/2 Mn nucleus.[49] Separation between these lines is much less, however, than that reported in other host lattices.[14,49] This aspect of the Mn spectrum is discussed in Section IX.

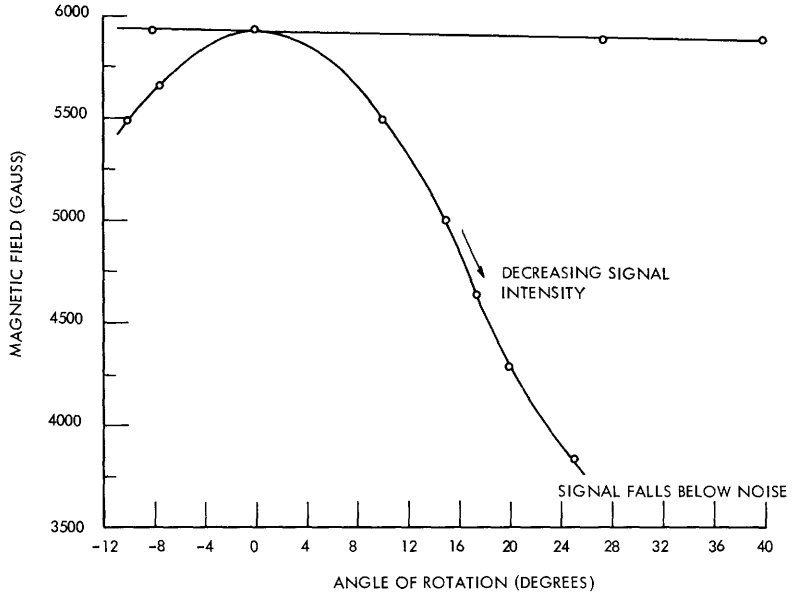

Fig. 25. EPR spectrum for Mn in $KTaO_3$. Crystal rotated about cube edge. (9.062 Gc)

The position of one of the hyperfine structure peaks of Fig. 26 is tabulated in Table XI at two different measurement frequencies. This permits calculation of the slope of the Zeeman spacing that results in the observed transition. The slope $g_s \sim 2.0$ applies at $\theta = 0°$, that is, the DC magnetic field is perpendicular to the distortion axis. As the crystal is rotated, the g_s value associated with the angular-dependent line falls and at $\theta = 24°$, $g_s \sim 1.3$. Line intensities remain essentially constant when the crystal is cooled from 4.2°K to 2.6°K. This result indicates that the transitions are within the ground state.

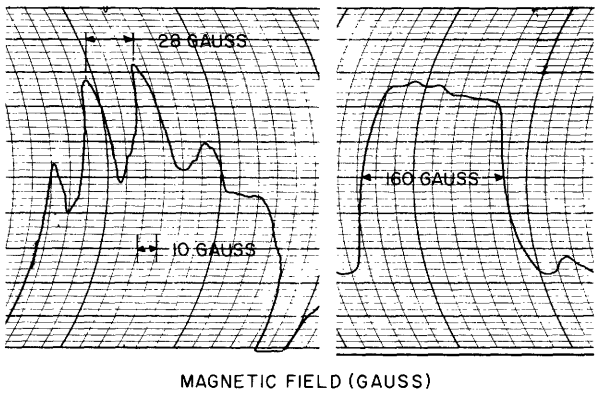

Fig. 26. EPR hyperfine structure for Mn-doped $KTaO_3$. (θ=90°)

Table XI. Line positions for manganese EPR spectrum.

Frequency (Gc)	Magnetic field (gauss)	Slope g_s
9.062	5977	–
8.588	5810	–
.474	167 ±5	2.02 ±.06

Several aspects of the Mn spectrum are puzzling, and we are unable to definitely relate the spectrum to either Mn^{4+} or Mn^{5+}.

6.5 EPR ABSORPTION IN Co-DOPED $KTaO_3$

No EPR spectra were observed either at room temperature or at 4.2°K. Lack of resonance at low temperatures may result if (i) the ground state is $^1A_1$ as claimed in the preceding discussion of the optical absorption spectrum, or (ii) the ground state is $^5T_2$ and the impurity site is distorted in such a way that the lowest state is a singlet.

We conclude that these negative EPR results do not prove or disprove our assertion that the Co^{3+} ground states are different at room temperature and at 4.2°K. These results do, however, eliminate the Co^{2+} ion, which would be expected to give a magnetic resonance spectrum.

6.6 EPR ABSORPTION IN Cr-DOPED $KTaO_3$

Observation of EPR spectra at 4.2°K reveals a single very broad line, approximately 2500 gauss wide and centered at 2000 gauss. This line is actually a poorly resolved combination of several resonances. Rotation away from 0° separates some of these, but loss of intensity soon drops them below noise level. No detailed examination of these resonances was undertaken. Clearly, chromium does not substitute in the lattice as Cr^{3+}.

VII. ELECTRIC FIELD EFFECTS ON EPR SPECTRA

Of the EPR results described in Section VI only the cubic Fe^{3+} spectrum is suitable for electric field experiments. All the other spectra show large local deviations from cubic symmetry; therefore any slight distortion caused by electrostriction would not be detectable.

For the electric field experiments we used the same sample as for the EPR data. The sample was placed in a silver-lined quartz cylinder on the end of an X-band waveguide. High-voltage leads passed through a teflon bushing in the dewar cap, continued through the centers of the screws that held the quartz cylinder onto the waveguide, and finally through a 1/4 inch hole into the sample holder. Figure 27 shows the interior

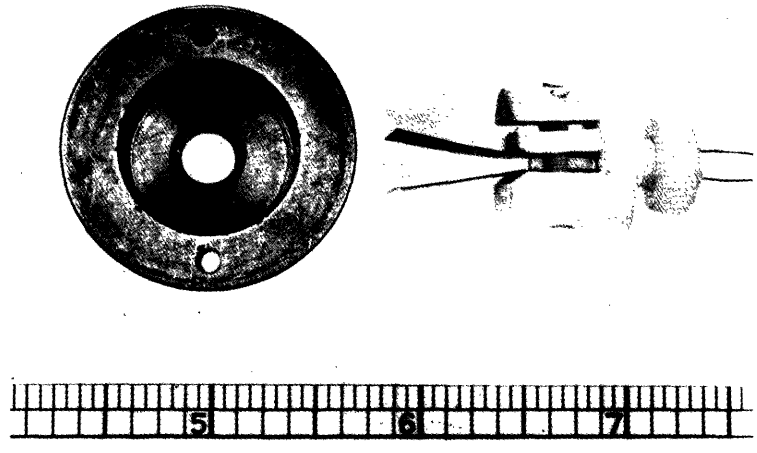

Fig. 27. Detail of high-voltage crystal holder and silver-lined quartz waveguide termination.

details of the sample holder. The crystal is clamped between the jaws of the teflon vise shown at the right. Two copper plates are pressed against the large surfaces of the sample, and the voltage leads are held between the copper and the vise. The copper plates flare out and are insulated from the X-band waveguide by a flexible polyfoam plug (not shown). The polyfoam also dampens vibrations of the copper which would superimpose excessive noise on the EPR signal. Flaring of the copper electrodes into the waveguide was necessary to provide a reasonable match to crystal dielectric resonances. No electrodes were placed on the sample other than the copper plates. Evaporated gold lowered the Q of all dielectric resonances to an excessive degree, while fired silver paint seemed to uncouple all the modes at 4.2°K.

It was necessary to use a well-stabilized high-voltage power supply; otherwise, the change in crystal dielectric constant (and resonant frequency) associated with voltage variations would have caused excessive drift of the EPR signal. The voltage was not applied to the crystal until it was immersed in liquid helium, since the breakdown

strength at room temperature was only several kilovolts per centimeter.

Because the electrodes were thick enough to shield the crystal from the 6-kc field modulation, all EPR Stark-effect measurements were made with the electric field perpendicular to the DC magnetic field. Both fields lie along crystal [100] axes or cube edges. If we assume that the applied electric field causes an axial distortion of the local symmetry at Fe^{3+} sites, the Fe^{3+} spin Hamiltonian is

$$\mathcal{H} = g\beta H \cdot S + \frac{a}{6}\left[S_x^4 + S_y^4 + S_z^4 - \frac{1}{5}S(S+1)(3S^2+3S-1)\right] + D\left[S_z^2 - \frac{1}{3}S(S+1)\right]$$

$$+ \frac{F}{180}\left[35S_z^4 - 30S(S+1)S_z^2 + 25S_z^2 - 6S(S+1) + 3S^2(S+1)^2\right],$$

for which the z axis is the distortion axis. The term in D results from an axial Y_2^0 term in the crystal field potential. The last term is a consequence of the fact that Y_4^{+4} and Y_4^{-4} are not related to Y_4^0 by the same constant factor as in cubic symmetry. In cubic symmetry the crystalline field is proportional to $\left[Y_4^0 + \frac{70^{1/2}}{14}\left(Y_4^4 + Y_4^{-4}\right)\right]$.

To find the energy levels it is convenient to begin with the assumption that the magnetic field lies along the z or distortion axis, since the axial terms are then diagonal. We then have

$$W_{\pm 5/2} = W'_{\pm 5/2} + \frac{10}{3}D + \frac{1}{3}F$$

$$W_{\pm 3/2} = W'_{\pm 3/2} - \frac{2}{3}D - F$$

$$W_{\pm 1/2} = W'_{\pm 1/2} - \frac{8}{3}D + \frac{2}{3}F.$$

The primes refer to the energy expressions given in Section VI for cubic symmetry. Because the magnetic field is actually perpendicular to the applied electric field, a transformation[50] is required; therefore, we replace D in these expressions by $-\frac{1}{2}D$. We should also transform F, but F is usually much smaller than D and we shall neglect it. The final result for the magnetic field at resonance is

$$g\beta H_1 = h\nu - 2a + 2D + \ldots$$

$$g\beta H_2 = h\nu + \frac{5}{2}a + D - \frac{5}{16}\frac{a^2}{g\beta H} + \ldots$$

$$g\beta H_3 = h\nu + \ldots$$

$$g\beta H_4 = h\nu - \frac{5}{2}a - D - \frac{5}{16}\frac{a^2}{g\beta H} + \ldots$$

$$g\beta H_5 = h\nu + 2a - 2D + \ldots .$$

According to these expressions an axial distortion caused by the electric field changes the separation in the outer pairs of lines by $|3D|$, and the outer lines shift half as much

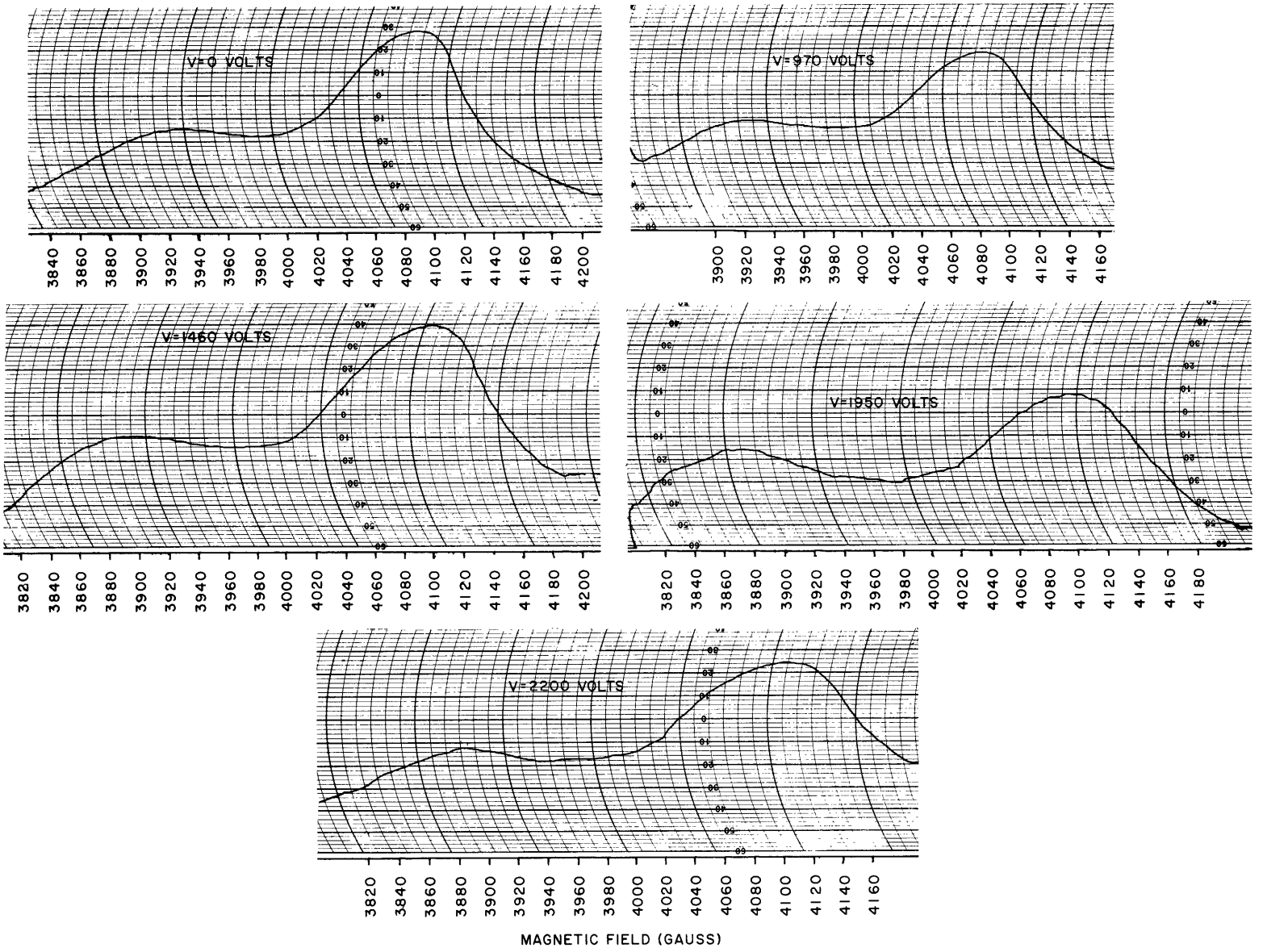

Fig. 28. Effect of applied electric field on magnetic resonances.

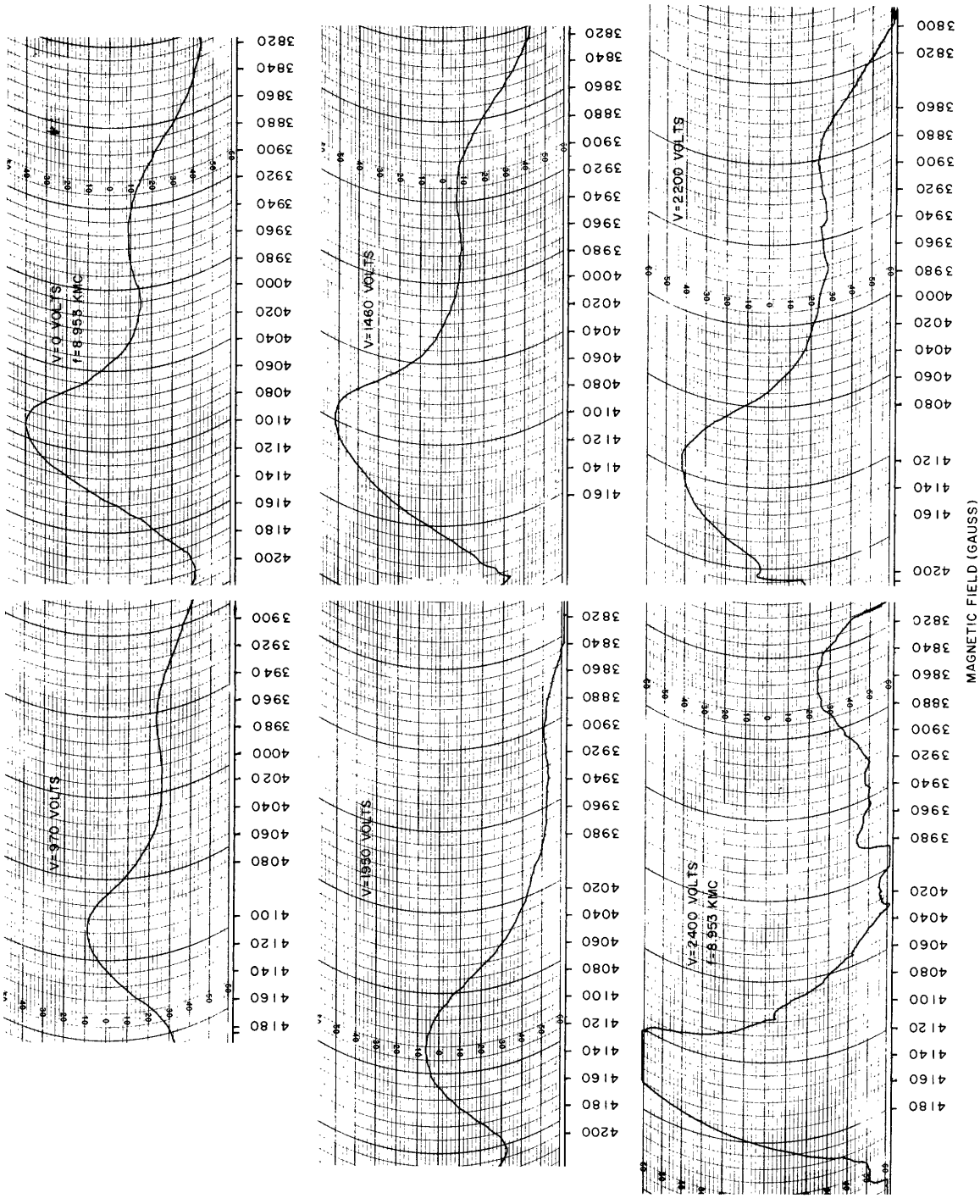

Fig. 29. Effect of applied electric field on magnetic resonances.

as the inner ones. All electric-field experiments were conducted on the high-field pair of lines. With $a > 0$, this pair is at H_2 and H_5. If $H_2 - H_5$ increases as the electric field is applied, then $D > 0$.

To measure the Stark effect we increase the voltage applied to the crystal and select a dielectric resonance on the Smith Chart oscilloscope. A strong voltage dependence of the mode frequencies is observed, although a detailed examination of this phenomenon was not undertaken. After we selected a suitably matched mode, we locked the spectrometer on the resonance and recorded the EPR spectrum. Figures 28 and 29 show tracings for various applied voltages. The corresponding records in the two figures are associated with the two directions of field sweep. Breakdown occurred in the high-voltage circuit at 2400 volts; consequently, only one direction of sweep was possible. The tracing shows a significant increase in line separation from which we conclude that $D > 0$. The width of the resonances and their overlap contribute considerable uncertainty about the true positions of the line centers. We estimate from these data that changes in peak positions and peak spacings can be determined within ±10 gauss.

The data of Figs. 28 and 29 are plotted in Figs. 30 and 31. Each point refers to the

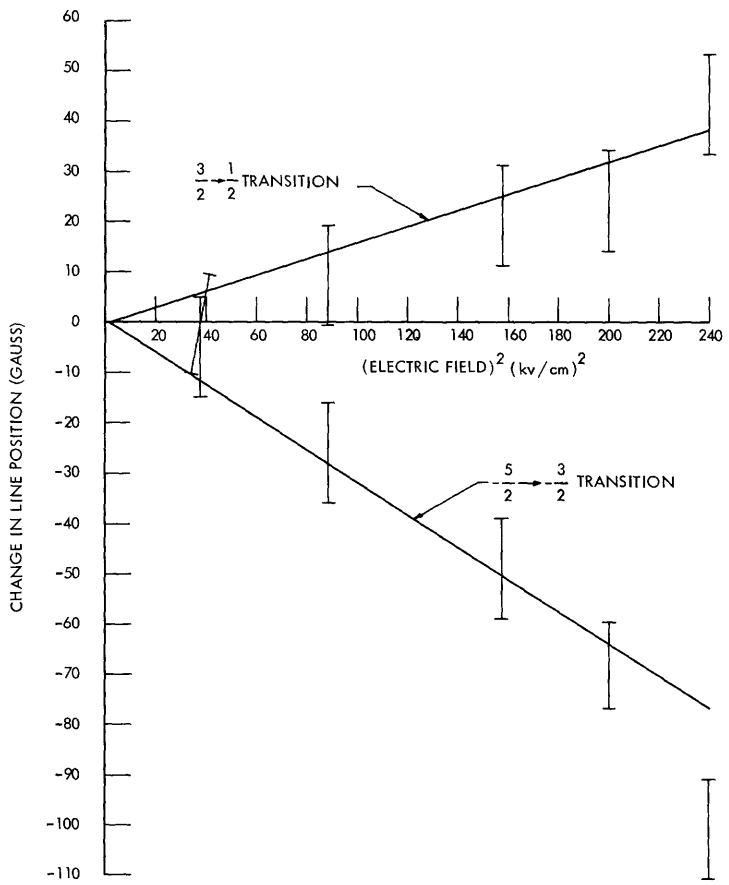

Fig. 30. EPR line position vs the square of the electric field.

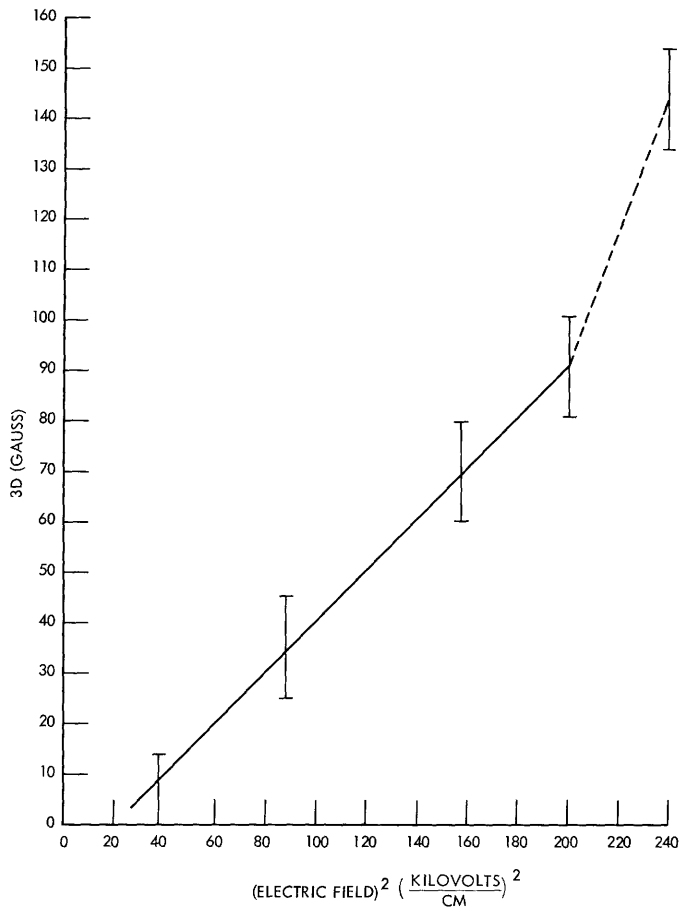

Fig. 31. Axial-splitting parameter 3D as a function of the square of the applied electric field.

average of two sweep directions of the field. The solid lines of Fig. 20 are drawn with slopes of +1 and −2 and emphasize the fact that the electric field effect on the low-field line is approximately twice the effect on the high-field line, as predicted. The increased line separation with applied electric field implies a positive value of D; this agrees with the observations in the tetragonal phases of both $BaTiO_3$ and $SrTiO_3$, and suggests that lattice distortions in $KTaO_3$ may be of the same nature as in other perovskites.

The magnitude of D may be estimated from observations on other crystals. Germanier, Gainon, and Lacroix[54] have attempted to relate D to the electric potential parameter A_2^0 for the $3d^5$ ion (Fe^{3+}, Mn^{2+}). Their final expression involves spin-orbit and spin-spin interactions and contains terms linear and quadratic in A_2^0. Agreement with experiment is poor, however, and these authors suggest that covalent bonding effects may be significant. They also report an experimental study of axial strain (pressure) effects on D in cubic MgO containing Fe^{3+}, Mn^{2+}, and Ni^{2+}. A linear relationship between D and strain (or A_2^0) is observed. Germanier and co-workers estimate that a term that is quadratic in A_2^0 does not become important until D exceeds approximately 0.2 cm^{-1}. Walsh[56,58] also finds a linear relationship between D and axial strain

Table XII. Effect of strain on D in several crystals.

Crystal	$D(10^{-4}\ cm^{-1})$	Reference
Fe^{3+} in MgO	14	54, 55
Ni^{2+} in MgO	130	57, 55
$NiSiF_6$	80	56
Mn^{2+} in MgO	3.5	54, 55

in nickel fluosilicate. Table XII summarizes the data and gives D for axial macroscopic strains of 0.01 per cent.

Huibregtse, Drougard and Young[59] find that the relation between lattice strains in $BaTiO_3$ and the polarization is

$$\epsilon = 9 \times 10^{-4} P^2,$$

where ϵ is the strain (per cent) in the polarization direction, and P is measured in $\mu coulombs/cm^2$. The square-law dependence results from the presence of a center of inversion in the unpolarized (cubic) $BaTiO_3$ lattice. If we assume that lattice strains affect the D associated with Fe^{3+} in $BaTiO_3$ to the same extent as for Fe^{3+} in MgO (see Table XII), the following expression can be written relating D to P^2.

$$D \approx 1.3\ P^2\ (10^{-4}\ cm^{-1}).$$

This quadratic EPR Stark effect requires polarizations greater than 3 $\mu coulombs/cm^2$ to produce a significant effect ($10^{-3}\ cm^{-1}$).

Hornig, Rempel and Weaver[9] observe that when a $BaTiO_3$ crystal is cooled below 120°C the tetragonal term D becomes significant and increases discontinuously to $\sim 450 \times 10^{-4}\ cm^{-1}$, while a remains approximately constant. Additional cooling increases D to $930 \times 10^{-4}\ cm^{-1}$ at 27°C. Rimai and Demars[13] report similar experiments in $BaTiO_3$ crystals containing $Gd^{3+}(4f^7)$ ions in Ba^{2+} sites, and compare their results with those of Hornig. The proportionality is found between D and P^2 for both ions. These data are calculated from the temperature dependence of D between 120°C and 27°C and are converted to polarization dependence by using the polarization vs temperature data of Merz.[60] The result is that $D = 1.4\ P^2$ for Fe^{3+} and $D = 0.5\ P^2$ for Gd^{3+}, where the D are the tetragonal terms in the spin Hamiltonian in units of $10^{-4}\ cm^{-1}$, and P is the total spontaneous polarization in $\mu coulombs/cm^2$.

The order of magnitude of our estimates that $D \approx P^2$ is confirmed by the data of Fig. 32 which shows a plot of 3D against P^2 for Fe^{3+}-doped $KTaO_3$. Taking 1 gauss = $0.93 \times 10^{-4}\ cm^{-1}$, we obtain (for $P > 1.5\ \mu coulombs/cm^2$)

$$D(10^{-4}\ \mathrm{cm}^{-1}) \approx -7 + 3P^2.$$

The values of P required to obtain Fig. 32 from Fig. 31 were calculated from the P vs E data of Fig. 12. (The last curve applies to an undoped sample, whereas the EPR

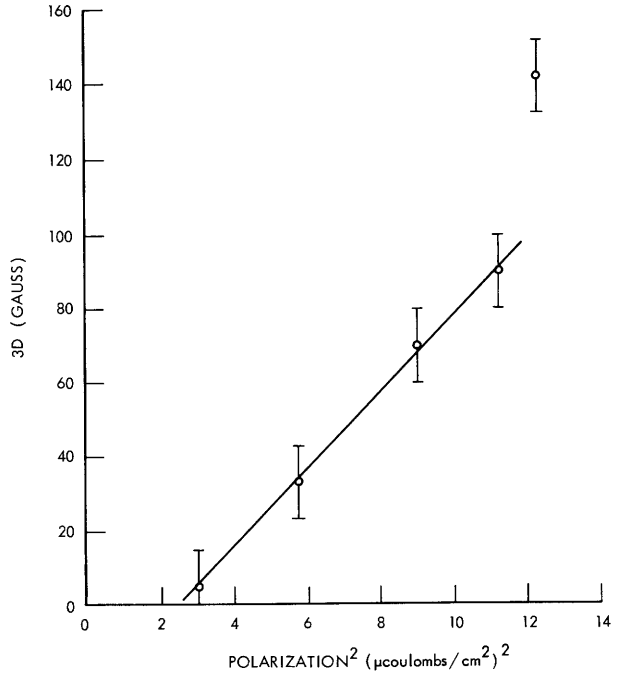

Fig. 32. Axial-splitting parameter 3D as a function of the square of the lattice polarization.

sample contains ~200 ppm Fe.) For this calculation we used an estimated low field κ (~3500) obtained by linear interpolation between the κ for the undoped sample and the κ for the 400-ppm sample. If we neglect the small term in P^5, the required polynomial becomes

$$E \approx 3.3\ P + 10^{-1}\ P^3.$$

Here, we have assumed that the coefficient of P^3 is the same as that for an undoped sample. The magnitude of the correction is less than 0.5 μcoulombs/cm^2, even at the highest fields.

Deviations from square-law behavior of D at low- and high-field strengths are apparent in Fig. 32. There are several possible explanations: (i) Because the Fe^{3+} ion is an impurity, the bulk lattice polarization might not generate a Y_2^0 at this site until the polarization of the surrounding unit cells was sufficient to overcome the predisposition of the impurity unit cell to remain cubic. The fact that Fe^{3+} lowers the Curie temperature tends to confirm the idea that the impurity stabilizes the cubic symmetry. (ii) Our assumption that $Y_2^0 \propto P^2$ may break down at high fields would explain the observed sharp

increase in 3D. (iii) The low-field deviations may be due to the electrode system. There may be a voltage drop between the copper plates and the sample. The frequencies of the dielectric resonances shift in a series of closely spaced but discontinuous steps as the electric field is applied. This suggests that liquid-helium breakdown occurs between the sample and the electrodes. Breakdown begins during the first 100 volts of applied field, and changes in the resonant frequency of the crystal are apparent immediately. At points where breakdown occurs, a low resistance path is expected between copper and the sample. If only a small region of the interface between the sample and the electrode breaks down at low voltages, we would expect the field within the crystal to have a strong spatial dependence. This would broaden the magnetic resonance line, because of the resulting variations in D within the sample. We would then expect the line to become narrower as the electric field increases and as the spatial variation decreases. That the opposite actually occurs is shown in Fig. 33 in which the linewidth of the $\frac{3}{2} \rightarrow \frac{1}{2}$ transition is plotted against E^2 and supports the claim that the voltage drop between electrode and crystal is small (< 100 volts) and could not cause the observed deviations from square-law behavior at low polarizations. Perhaps the most likely explanation is that the crystal is not precisely cubic at 4.2°K but has a built-in strain of approximately 7×10^{-6}.

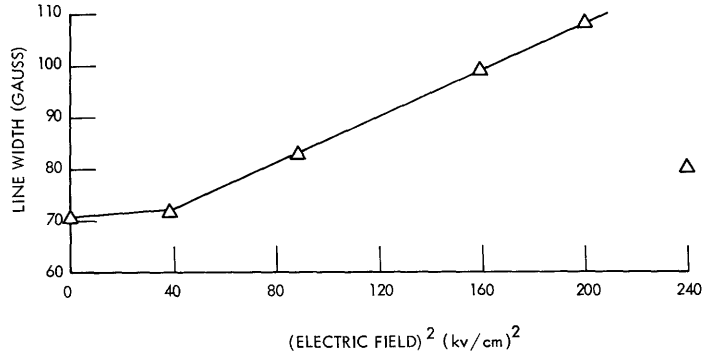

Fig. 33. Effect of applied electric field on resonance linewidth.

We still must explain the increase in linewidth with an increase in electric field strength and the decrease in linewidth at the high-field point in Fig. 33. This experimental point is also associated with a rapid increase in $|3D|$, as illustrated in Figs. 31 and 32. The increase in linewidth may result from a distribution of crystal strains that produces a somewhat different electrostrictive effect in various parts of the crystal. We suggest that additional data are needed at high polarization.

The final conclusion to be drawn from the EPR Stark-effect data is that the order-of-magnitude expression $D \approx P^2$ is valid. The total polarization, therefore, is a good measure of the lattice distortion at a magnetic impurity site both for the spontaneous polarizations associated with Fe^{3+} in $BaTiO_3$, and for the induced polarizations for Cr^{3+} in MgO and Fe^{3+} in $KTaO_3$. We conclude that the electrostriction coefficient is relatively constant from material to material, if P^2 rather than E^2 is taken to be the significant

driving force. We have also shown that an induced polarization produces essentially the same effect as a spontaneous polarization. The negative results of Hornig, Rempel, and Weaver concerning the EPR Stark effect in $BaTiO_3$ remain puzzling. Perhaps the dielectric-resonator method could be applied to $BaTiO_3$ by using the large single crystals that are now available.

Table XIII. Stark effect.

E(kv/cm)	$D(10^{-4}\ cm^{-1})$		
	Fe^{3+} in $KTaO_3$	Cr^{3+} in Al_2O_3	Cr^{3+} in MgO
5	~0	5	–
10	12	9	–
14	30	13	–
100	–	–	0.002

In Table XIII, we compare the quadratic EPR Stark effect for Fe^{3+} in $KTaO_3$ with the linear effect[3] of Cr^{3+} in Al_2O_3 and with the quadratic effect of Cr^{3+} in MgO.

The measured D values for Fe^{3+} in $KTaO_3$ are the largest reported thus far for either quadratic or linear Stark effects for iron-group substitutional impurities. (Interstitials in silicon give a much larger effect.)

VIII. COVALENT BONDING PHENOMENA IN $KTaO_3$

Evidence for covalent bonding of the impurity ions to the ligands is provided by the observed EPR in $KTaO_3$ and includes a resolved ligand hyperfine structure. The ligand electrons may penetrate into the region occupied by the central ion (central field covalence)[40] or the orbits of the magnetic electrons may include an admixture of orbitals on the ligands (symmetry restricted covalence). The experimental evidence can be summarized as follows.

1. The $\frac{1}{2} \rightarrow -\frac{1}{2}$ transition associated with the Fe^{3+} ion in cubic symmetry is much broader than would be expected if dipole-dipole interactions caused the broadening.

2. A well-resolved hyperfine structure has been observed for the Fe^{5+} spectra.

3. The six hyperfine lines for the Mn ion are much more closely spaced in $KTaO_3$ than in other host lattices.

4. The saturation behavior suggests that the EPR lines are inhomogeneously broadened. We shall now discuss each of these observations except for the fast passage effects and saturation behavior, which are reported in Section IX.

If we refer to Fig. 21, which shows recorder tracings of the cubic Fe^{3+} spectrum, we see that the linewidth of the central $\frac{1}{2} \rightarrow -\frac{1}{2}$ resonance is ~60 gauss at half-maximum. At 45° the line has the same width. The other transitions are broader, perhaps 100-120 gauss, and almost independent of angle. In the 45° tracing, for example, all of the resonances are of comparable width except for one low-field line, which is a double line. The broad linewidth cannot be attributed to crystal strains because the $\frac{1}{2} \rightarrow -\frac{1}{2}$ transition is expected to be much less affected by strains than the others $\left(\pm\frac{5}{2} \rightarrow \pm\frac{3}{2},\ \pm\frac{3}{2} \rightarrow \pm\frac{1}{2}\right)$. The last are transitions between different Kramers doublets and depend directly upon the zero-field splittings. As a result, a distribution of zero-field splittings attributed to lattice strains should broaden these lines and not affect the $\frac{1}{2} \rightarrow -\frac{1}{2}$ transition. This effect has been observed in $SrTiO_3$ and in $BaTiO_3$ containing Fe^{3+}. Hornig and his co-workers[9] find a narrow 7-gauss $\frac{1}{2} \rightarrow -\frac{1}{2}$ transition for Fe^{3+} in $BaTiO_3$. The other lines are much broader, and are 200 gauss wide for some crystal orientations. These authors also find that the linewidths have a pronounced angular dependence for all but the $\frac{1}{2} \rightarrow -\frac{1}{2}$ transition. Similar results have been observed for Fe^{3+} in $SrTiO_3$, for which the $\frac{1}{2} \rightarrow -\frac{1}{2}$ transition is only 7-10 gauss wide and the others are 30-50 gauss wide.[16] We conclude that the 60-gauss linewidth of the $\frac{1}{2} \rightarrow -\frac{1}{2}$ transition for Fe^{3+} in $KTaO_3$ cannot be caused by crystal strains, although it is possible that the 25-55 gauss extra width of the other transitions results from this mechanism.

The observed 60-gauss width cannot be attributed to dipole-dipole interactions within the Fe^{3+} spin system. Hornig and his co-workers report an iron concentration of 0.01-0.04 mole per cent in their $BaTiO_3$ samples. This concentration is comparable with that in $KTaO_3$ (0.02%), while their $\frac{1}{2} \rightarrow -\frac{1}{2}$ linewidth is only 7 gauss. Calculations of spin-spin broadening in ruby reported by Grant[61] suggest that the theoretical linewidth should

be less than 1 gauss for the low concentrations known to be present in $KTaO_3$.

We attribute the observed line broadening in Fe^{3+}-doped $KTaO_3$ to an unresolved hyperfine interaction with the ligand nuclei. This effect is not expected in either $BaTiO_3$ or $SrTiO_3$, since only a small fraction of the nuclei in these substances exhibits a non-zero nuclear spin (see Table XIV). Bennett and Budnick[62] have observed nuclear magnetic resonance in $KTaO_3$ associated with the Ta_{181} (I = 7/2) nucleus.

Since the six nearest-neighbor oxygens have no nuclear moment, the existence of a nuclear hyperfine interaction in $KTaO_3$ implies that the magnetic $3d^5$ electrons couple to next-nearest-neighbor nuclei. To understand this coupling, we examine the nature of the $3d^5$ wave functions. Low and others have shown that an octahedral crystalline field splits a fivefold degenerate 3d function into a lowest triplet and a higher doublet. The triplet orbitals are usually designated $d\epsilon$ (or t_{2g}), and the doublet orbitals $d\gamma$ (or e_g). The $d\epsilon$ wave functions transform in the same way as xy, xz, and yz; each displays four lobes at 45° with respect to the x, y, and z directions. The $d\gamma$ orbitals transform as (x^2-y^2) and $(3z^2-r^2)$, and have lobes and maximum charge density in the direction toward the six oxygens. The repulsion between the $O^=$ ligands and the $d\gamma$ orbitals raises their energy relative to the $d\epsilon$ orbitals. If Hund's rule applies, as it does for high-spin $Fe^{3+}(3d^5)$, the first three electrons are in $d\gamma$ orbitals.

Table XIV. Nuclear spins and moments.

Nucleus	Spin	μ (Nuclear magnetons)	Abundance (%)
Ta_{181}	7/2	2.1	100
K_{39}	3/2	0.391	93.1
K_{41}	3/2	0.215	6.9
Ti	0	0	87
Ba	0	0	82
Sr	0	0	92

For covalency it is necessary to include admixtures of orbitals localized on the ligands. When such covalent admixtures are included, a hyperfine interaction can occur between the magnetic electrons and the ligand nuclei. Tinkham[63] lists three mechanisms for this interaction: (i) an isotropic contact contribution from admixture of S-electron orbitals; (ii) an anisotropic interaction between electron and nuclear magnetic moments; and (iii) an interaction between orbital moments and nuclear moments.

Eisenstein[64] and Liehr[65] have used symmetry arguments to decide which ligand orbitals are permitted to mix with the $d\epsilon$ and $d\gamma$ central-ion orbitals. The pertinent results are shown in Table XV, in which σ and π refer to angular momenta (measured

Table XV. Allowed ligand admixtures.

Central ion orbital	"Cubal" K^+ site	"Octahedral" $O^=$ site
$d\epsilon$	σ, π	π
$d\gamma$	π	σ

with respect to the bond axes) for the allowed ligand orbital admixtures.

Table XV shows that no symmetry restriction prevents a hyperfine interaction between $d\epsilon$ central-ion orbitals and the potassium nuclei. Interactions of this type (cube center to corner) have not been reported, although Tinkham[63] observed resolved nearest-neighbor hyperfine structure with the F^- octahedron in Mn^{2+}-doped ZnF_2. He suggested that the important contribution to the hfs comes from ligand σ orbitals because they overlap central-ion orbitals to a greater extent than do ligand π orbitals. According to Table XV, $d\epsilon$ orbitals should give a small hfs with nuclei at octahedral sites (e.g., F^- in ZnF_2). This has been confirmed by Tinkham who found a large hfs for $Mn^{2+}(d\epsilon^3, d\gamma^2)$ and a much smaller hfs for $Cr^{3+}(d\epsilon^3)$. According to Table XV, σ coupling is allowed only from $d\epsilon$ orbitals to the K^+ nuclei in $KTaO_3$.

We return to the examination of EPR linewidths and repeat our contention that the observed 60-gauss linewidth of the $\frac{1}{2} \rightarrow -\frac{1}{2}$ transition in cubic Fe^{3+} is primarily due to an unresolved hyperfine interaction. It seems unlikely that the Ta nuclei interact strongly with the central Fe^{3+} ion, since they are separated by $O^=$ ions. Perhaps the lack of resolution is due to broadening of the individual hyperfine lines by a weak Ta-Fe^{3+} interaction. The main interaction would be between K^+ orbitals and the $d\epsilon$ central-ion orbitals. Two other aspects of the Fe^{3+} spectrum are worth examining. (i) The EPR lines in the axial Fe^{3+} spectrum are only 20 gauss wide. As we have concluded, the axial distortion almost certainly results from a nearest-neighbor $O^=$ vacancy. This vacancy is expected to significantly rearrange the nuclear positions and to alter the bonding characteristics. It is not surprising, then, that hyperfine interactions are significantly affected. (ii) All the magnetic resonances in Fe-doped $KTaO_3$ (except for axial Fe^{3+}) have comparable linewidths. This is consistent with the suggestion that many of these resonances are due to Fe^{3+} with next-nearest-neighbor or more remote $O^=$ vacancies. When the $O^=$ vacancies lie beyond the magnetic-ion unit cell, a drastic modification of the covalent bonding of $d\epsilon$ orbitals to the K^+ nuclei is not expected.

If the preceding arguments are correct, we expect that an ion having only $d\epsilon$ orbitals – for example, $Fe^{5+}(d\epsilon^3)$ – will be broadened as much as $Fe^{3+}(d\epsilon^3 d\gamma^2)$. The interaction with the Ta^{5+} nuclei should be much weaker, since no $d\gamma$ orbitals are assumed to be present and thus cannot overlap the intervening $O^=$ ions or couple to the next-nearest-neighbor Ta nuclei. The K^+ hyperfine interaction might be resolved. This has been observed for the Fe^{5+} ion in $KTaO_3$.

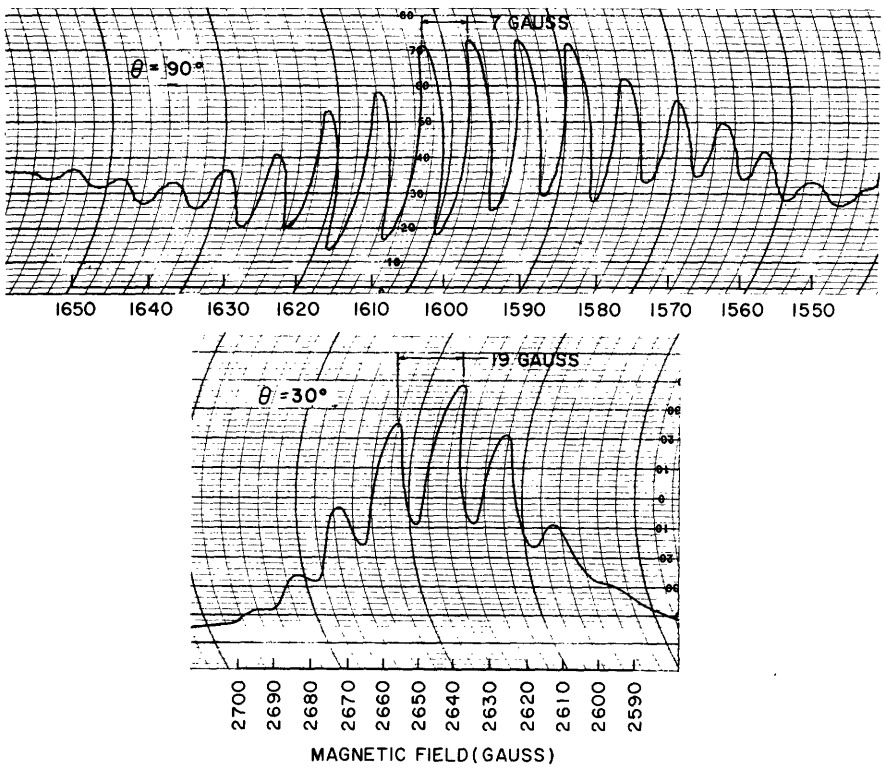

Fig. 34. Hyperfine structure of Fe^{5+} spectrum.

Figure 34 shows the hyperfine structure of the Fe^{5+} spectrum. The top recorder tracing for χ'' was obtained with the magnetic field perpendicular to the distortion axis and the bottom tracing was obtained at an angle of 30°. Seventeen lines are clearly visible in the 90° spectrum. The separation is 7 gauss, and linewidths at half-maximum are approximately 3 gauss. (At high power levels (> 10 db) another narrow line disrupts the symmetry of the hyperfine pattern. The source of this resonance is not known.) If the hfs arises from hyperfine interaction with the eight surrounding K^+ nuclei (spin 3/2), the expected relative line intensities can be calculated. The maximum total spin I of the eight nuclei is 12, which gives (2I + 1), or 25 lines. The individual line intensities were calculated for eight spin 3/2 nuclei. Although Low[48] indicates that these numbers are binomial coefficients, it should be emphasized that our numbers are not. The results are listed in Table XVI. The relative intensities for six spin 3/2 and four spin 3/2 nuclei are also given.

The total number of combinations of spin orientations must equal 4^8, 4^6, and 4^4, respectively. The totals in Table XV check these values, if we double all entries except the zero-spin number.

The relative line intensities (at θ = 90° on Fig. 34) are indicated on Fig. 35 by circles. Both theoretical curves are taken from Table XV. On Fig. 35 the width at one-half the maximum value is 8 line spacings or 56 gauss. It is reasonable, then, to suggest that the unresolved 60-gauss linewidth for the $\frac{1}{2} \rightarrow -\frac{1}{2}$ transition in cubic Fe^{3+} is

Table XVI. Expected relative intensities of hyperfine lines.

Spin (I)	8 Spin 3/2 Nuclei	6 Spin 3/2 Nuclei	4 Spin 3/2 Nuclei
0	8092	580	44
1	7728	546	40
2	6728	456	31
3	5328	336	20
4	3823	216	10
5	2472	120	4
6	1428	56	1
7	728	21	
8	322	6	
9	120	1	
10	36		
11	8		
12	1		

produced by the same interaction.

The relatively good agreement between the observed Fe^{3+} hyperfine structure and a theory based on 8 equivalent spin 3/2 nuclei suggests that all of the K^+ nuclei couple equally to the central ion. The EPR angular dependence data, however, show a strong axial distortion. It may be that the Fe^{5+} ion remains in the center of an $8K^+$ cube, but

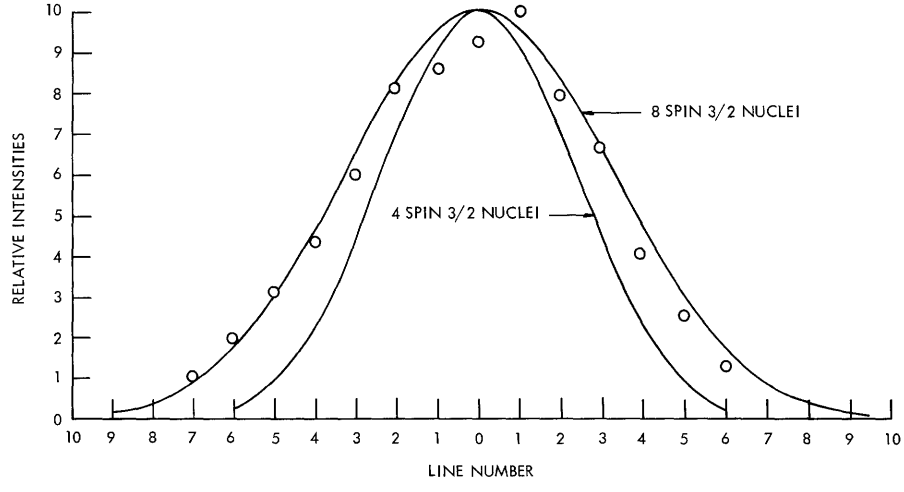

Fig. 35. Relative line intensities of next-nearest-neighbor hyperfine resonances for Fe^{5+}. Solid lines are based on Table XVI.

one of the 6 nearest-neighbor $O^{=}$ ions moves in closer to the Fe^{5+} ion. This collapse of the O_6 octahedron may be related to the small size of the Fe^{5+} (see our previous discussion).

The lower recorder tracing of χ' in Fig. 34 is for $\theta = 30°$ from the distortion axis. Line spacing is 19 gauss, hyperfine linewidth is ~12 gauss, and the total linewidth remains at ~60 gauss. The hyperfine interaction is clearly anisotropic, although a complete investigation of angular dependence was not undertaken. At $\theta = 0°$ (along the distortion axis), the hyperfine lines are unresolved. According to Tinkham an anisotropic hyperfine interaction is expected if the dipole-dipole term dominates. More data must be obtained before a thorough discussion of the hyperfine interaction can be presented. In particular, a complete determination of angular dependence might permit sorting the various interactions, as Tinkham did for ZnF_2. From these data it would be interesting to calculate the percentage of the time that the magnetic electrons spend on the K^+ ions. The ligand admixtures may also provide an explanation for the $g_\perp = 4.25$ splitting factor for Fe^{5+}.

The preceding discussion of the effects of covalent bonding applies only to the magnetic impurities. The nature of bonding in the host lattice cannot be inferred from these results.

IX. LINE SHAPE, SATURATION, AND FAST-PASSAGE BEHAVIOR

The published EPR for $BaTiO_3$ and $SrTiO_3$ are derivative χ'', that is, they have the double-sided dispersion shape. Derivative line shapes in $KTaO_3$ differ from those observed in the titanates in several respects.

1. Resonances are all one-sided and absorption shaped with either χ' or χ'' observed.
2. Reversal of the direction of the field sweep leaves the sign of χ' unchanged and changes the sign of χ''.
3. Strong saturation of χ'' relative to χ' is observed.

We shall attribute this line shape and saturation behavior to inhomogeneous broadening associated with the previously discussed ligand hyperfine interaction. The line shape and the saturation resemble that observed for the hyperfine broadened EPR of the F centers in the alkali halides. We can therefore make use of published theoretical results that were derived to explain F-center observations.

Perhaps the most typical characteristic of an inhomogeneously broadened EPR line is the difference in the saturation behavior of the dispersion and absorption signals. Portis[45] has shown that

$$\frac{\chi''}{\chi'} \approx \frac{1}{\left(1+\gamma^2 H_1^2 T_1 T_2\right)^{1/2}}, \tag{8}$$

where H_1 is the RF magnetic field in the sample, T_1 and T_2 the spin-lattice and spin-spin relaxation times, and γ the gyromagnetic ratio. F-center EPR in NaCl supports[44] this expression. The use of the sample as a dielectric resonator complicates the saturation; H_1 is not constant throughout the sample and, therefore, the degree of saturation should exhibit a spatial variation.

Inhomogeneously broadened EPR can exhibit a bewildering variety of line shapes determined by the relative magnitudes of many test parameters. Weger[66] has examined the problem theoretically and experimentally. His experimental results are concerned with inhomogeneously broadened EPR in phosphorus-doped silicon. The test conditions that produce the line shapes observed in $KTaO_3$ are described by Weger as "rapid adiabatic passage with a short time between consecutive field modulation cycles"; this refers to Weger's Case 7, in which there is phase-sensitive detection.

$$\gamma H_1^2 \geq H_m \omega_m \tag{9a}$$

$$\gamma^2 H_1^2 T_1 T_2 \gg 1 \tag{9b}$$

$$2\pi f_m T_1 \gg 1 \tag{9c}$$

$$H_m \gg H_1 \tag{9d}$$

$$\frac{dH_o}{dt} \ll \frac{H_m}{T_1}, \tag{9e}$$

where H_1 is the RF field, H_m the modulation field, f_m the modulation frequency, and H_o the DC magnetic field. To determine whether Eq. 9 applies to our experiment, we require estimates of H_1 and T_1.

The maximum value of H_1 in the $KTaO_3$ sample can be estimated from

$$W = \frac{QP_L}{\omega},$$

where W is the total energy stored in the sample, P_L is the power absorbed, and ω is the RF frequency. We also have

$$W = \frac{1}{2}\mu_o H_1^2 Vf.$$

Here, the factor f depends on the details of the mode pattern but is probably ~1/8, since we expect a rather high-order mode that has spatial variation in all three crystal directions, and V is the crystal volume. The final result is

$$H_1 \text{ max} \approx 0.2\sqrt{\frac{Q_o P_L}{V}}, \tag{10}$$

where H_1 is in gauss, P_L is the power lost in microwatts, V is the crystal volume in mm^3, and Q_o is the crystal Q in units of 10^3. The appropriate parameters for the iron-doped sample are $Q_o \sim 10$, $V = 80$ mm^3, and $P_L \approx \frac{1}{2}P_i$, with P_i the incident power in microwatts. Then

$$H_1 \text{ max} \approx 0.05\ P_i^{1/2} \text{ gauss}.$$

We can estimate T_1 by examining the saturation behavior in $KTaO_3$. Observation of the relative magnitudes of χ' and χ'' is facilitated by direct visual observation of the magnetic Q circle on the Smith Chart plotter as the field is swept slowly through resonance. This circle becomes a straight line in the χ' direction at high powers because χ'' is heavily saturated. As the power is reduced, the straight line broadens into an ellipse and, in the unsaturated limit, into a circle. A typical set of saturation data for one of the iron resonances is given in Table XVII. From Table XVII the maximum RF field for $\gamma^2 H_1^2 T_1 T_2 \approx 1$ in Eq. 8 is estimated to be 0.01 gauss. Taking $\overline{H_1^2} \approx \frac{1}{8}|H_1 \text{ max}|^2$, we obtain $T_1 T_2 \sim 30 \times 10^{-11}$ sec^2. If we assume also that $T_2 \sim 10^{-8}$, the estimated T_1 becomes approximately 30 msec. This value of T_2 corresponds to a dipolar broadening of approximately 1 gauss. According to Grant,[61] the ~0.02 per cent concentration of magnetic impurities in $KTaO_3$ is expected to exhibit widths of the order of 10^{-8} sec.

Similar saturation results are obtained for the Mn-doped sample: $V \sim 500$ mm^3, $P_i \sim 100$ μwatts, and $\chi'/\chi'' \sim 10^3$. Substitution of these values in Eqs. 8 and 10 gives

Table XVII. Saturation behavior of the resonance line.

H_1 max (gauss)	Power (μwatts)	$\frac{\chi''}{\chi'}$
.05	1	~0
.02	.1	~1/4
.005	.01	~1

$T_1T_2 \sim 10^{-10}$, or 10^{-11} sec^2 and $T_1 \sim$ 1-10 msec.

These estimates merely suggest that the observed saturation behavior is consistent with T_1 values in the 1 msec to 100 msec range, and that very long time constants are not required. A thorough investigation of saturation behavior was not attempted.

We are now able to see whether Weger's Case 7 applies. Equation 9a is the adiabatic condition. Substituting ω_m = 6 kc and $H_1 \approx 0.05\ P_i^{1/2}$ in (9a) gives $P_i \geq H_m$. Since H_m = 0.1-1.0 gauss and $P_i \sim$ 0.1-10 μwatts, the adiabatic inequality is satisfied at the higher power levels. Equation 9b is the saturation condition, and it is satisfied. Equation 9c requires $T_1 \gg 0.03$ msec, which is also satisfied. Equation 9d requires $H_m \gg H_1$, or $H_m \gg 0.05\ P_i^{1/2}$. This inequality holds except at high power levels and low modulation amplitudes. Equation 9e requires a field sweep rate less than 100 gauss/sec and is easily satisfied.

We conclude, then, that the test conditions are of the right order of magnitude to produce the observed absorption shapes, provided that the EPR lines in $KTaO_3$ are inhomogeneously broadened.

X. CONDUCTING CRYSTALS (TRANSPORT PROPERTIES)

Electrical conductivity, Hall effect, and optical absorption data obtained from pale blue, transparent, single-crystal $KTaO_3$ are presented and briefly discussed in this section. An extremely rapid increase in electron mobility μ with decreasing temperature ($\mu \propto T^{-3}$) has been observed.

There are few published references to transport properties in materials with high dielectric constants. Breckenridge and Hosler[67] and von Hippel, Kalnajs, and Westphal[68] have reported conductivity and Hall measurements in n-type rutile (TiO_2). Branwood, Hughes, Hurd, and Tredgold,[69] and Branwood and Tredgold[70] report rather incomplete conductivity investigations of ceramic and single-crystal $BaTiO_3$. Hall effect and free-carrier absorption experiments had not been previously reported in any of the perovskite ferroelectrics. It should be emphasized that our investigation of transport properties is peripheral to the main investigation, which concerns the EPR Stark effect, and no claim is made that the literature search is complete or that the interpretation of data is definitive. Some interesting possibilities for future research are suggested, however.

Pale blue, transparent crystals grown from low-tin melts were used in all measurements. Preliminary attempts to measure two-terminal resistivity were unsuccessful because low-resistance ohmic contact to the crystal could not be achieved. Because of these difficulties, a four-terminal null method was used for all resistivity measurements.

Hall-effect data and most of the resistivity measurements were obtained from a crystal with the dimensions and electrode configuration shown in Fig. 36. Electrodes

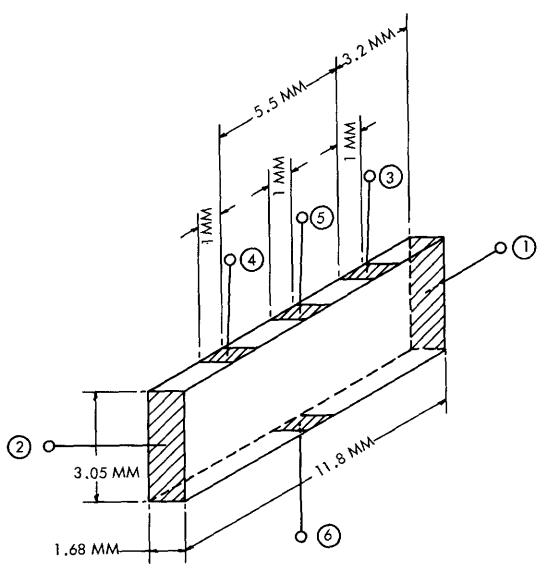

Fig. 36. Sample for Hall effect and conductivity measurements.
⑤ and ⑥, Hall probes.
③ and ④, Conductivity probes.

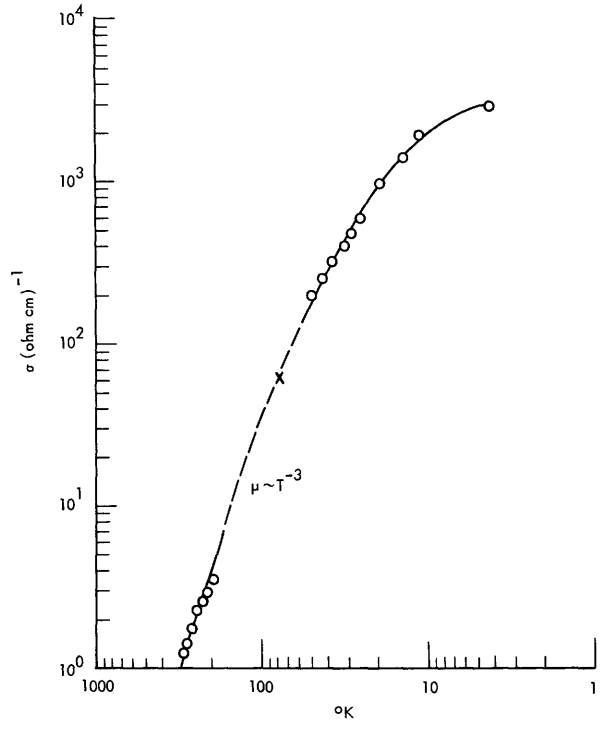

Fig. 37. Temperature dependence of the electrical conductivity for conducting $KTaO_3$.

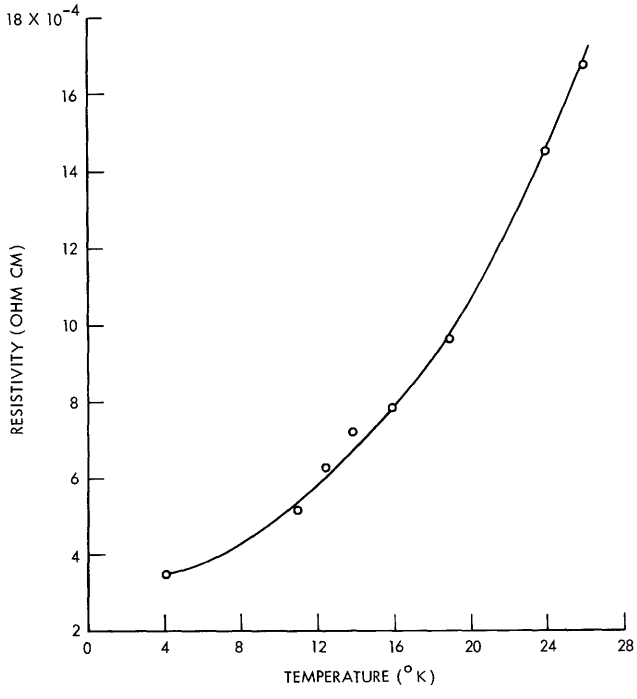

Fig. 38. Low-temperature resistivity of $KTaO_3$.

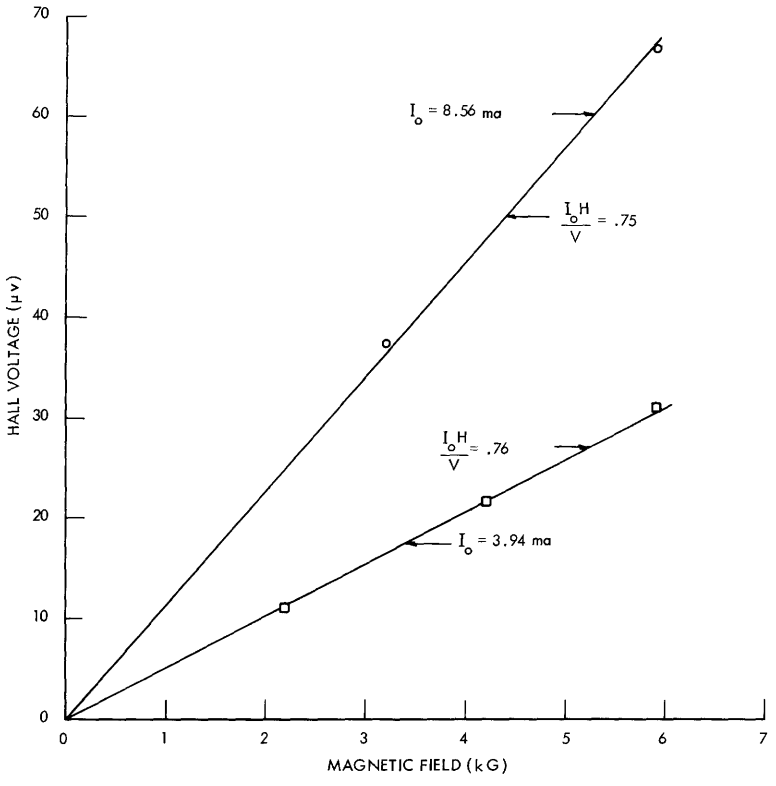

Fig. 39. Hall voltage as a function of DC magnetic field strength.

were of evaporated gold and were connected to the copper lead wires with 50-50 tin-indium solder. In order to stabilize the crystal temperature and minimize thermoelectric effects, the sample was mounted on a copper block which was surrounded by a cylindrical copper heat shield. Electrical conductivity vs temperature data are shown in Fig. 37. The low-temperature data are particularly interesting, and are plotted separately on a linear graph in Fig. 38. Room-temperature Hall data are plotted in Fig. 39 for two values of the crystal current I_o. From Figs. 37 and 39, we obtain a carrier concentration at room temperature of

$$n = 2.8 \times 10^{17}\ \text{cm}^{-3},$$

and a Hall coefficient

$$R = -22\ \text{cm}^3/\text{coulomb}.$$

The negative R indicates electron or n-type conduction.

The Hall mobility μ_H can be calculated from $R_\sigma = \mu_H$, if we know the conductivity and the Hall coefficient. By substituting $|R| = 22\ \text{cm}^3/\text{coulomb}$ and $1/\sigma = 0.8$ ohm cm, we obtain the Hall mobility at room temperature

$$\mu_H = 28\ \frac{\text{cm}^2}{\text{volt sec}}.$$

This value is of the order of magnitude that is observed in a number of oxide single crystals. Typical values after Hannay[71] are 5 cm^2/volt sec for BaO, 10 cm^2/volt sec for CdO, 2 cm^2/volt sec for MgO, and several hundred for ZnO.

The temperature dependence of the conductivity is evident in Fig. 37 and implies a temperature dependence of the Hall mobility that is at least as strong, since $\frac{dn}{dT} > 0$. At 215°K, the Hall coefficient had not changed from the room-temperature value. Consequently, the carrier density remained at 2.8×10^{17} cm^{-3} down to at least 215°K. The entire temperature dependence of σ is then contained in μ (see Fig. 37) and this implies that

$$\mu_H \propto T^{-3} \quad \text{for} \quad T > 215°K.$$

Below 215°K, a less rapid change is indicated. Because Hall measurements were not obtained below 215°K, it is not known how the dependence of conductivity on temperature should be divided between R and μ_H. An assumption of constant concentration places a lower bound on μ at 4.2°K of 63,000 cm^2/volt sec.

The following expression can be written for μ_D, the drift mobility

$$\mu_D = \frac{e\langle\tau\rangle}{m_c^*} \approx \mu_H,$$

where $\langle\tau\rangle$ is the average value of the carrier relaxation time, m_c^* is the conductivity effective mass, and e is the electronic charge. Temperature dependence of μ_D or μ_H can be contained in either $\langle\tau\rangle$ or m_c^* as has been discussed in detail by Lyden.[72] The temperature dependence of τ is given by Hannay.[71] Lattice scattering by acoustic vibrations requires that $\tau_L \propto T^{-n}$ with $1 \leq n \leq 3/2$. The value of n depends upon the degree of degeneracy and the precise shape of the band edges. With spherical band edges and no degeneracy, n = 3/2. At low temperature, impurity scattering often dominates with its $\tau_I \propto T^{3/2}$ dependence. In polar crystals such as $KTaO_3$ or TiO_2, optical mode

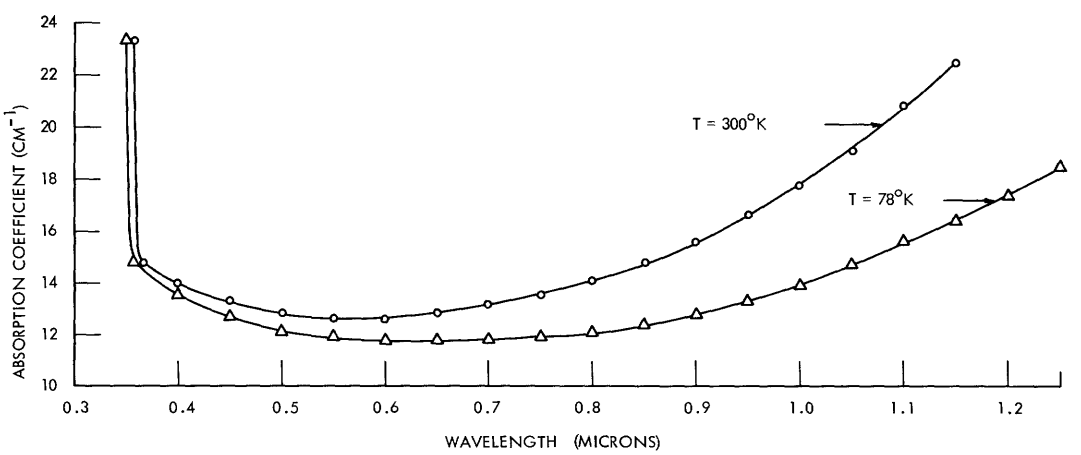

Fig. 40. Optical absorption of conducting $KTaO_3$.

scattering can be important. For this mechanism $\tau_o \propto Ae^{\theta/T}$, where A is a comparatively weak function of temperature, and θ is the Debye temperature.

The use of the Drude-Zener theory[71] of free-carrier absorption offers a convenient means of examining the temperature dependence of m_c^*. Optical absorption data were obtained from a pale blue crystal, 1.55 mm thick, rather than from the sample used for Hall and conductivity measurements. This crystal has a room temperature resistivity of 0.16 ohm cm. Results are plotted in Fig. 40. The sharp increase at 0.35 micron is associated with the characteristic optical absorption edge of $KTaO_3$. Increased absorption in the infrared gives the crystals their blue color. The data of Fig. 40 are plotted against λ^2 in Fig. 41. The predicted square dependence for free-carrier absorption is roughly confirmed at the longer wavelengths. From these data it is possible to estimate

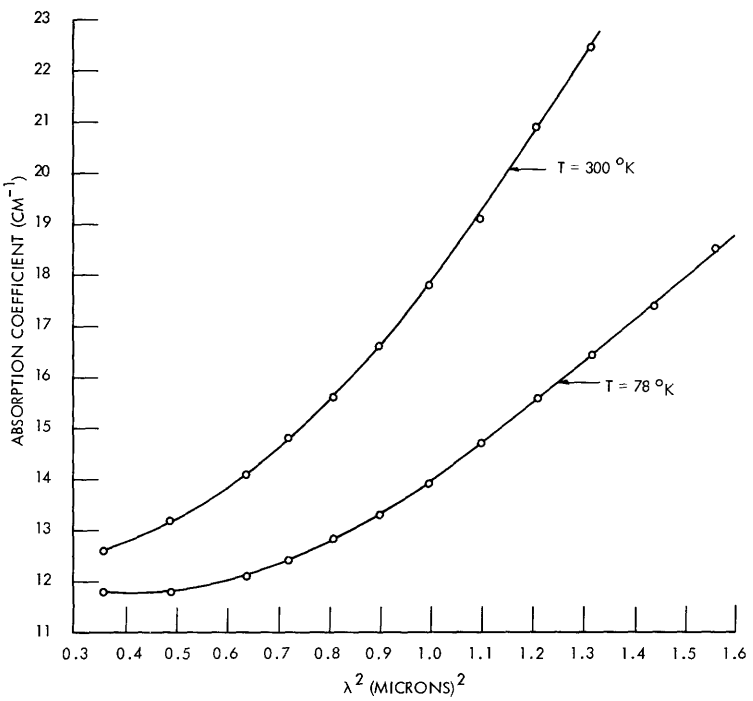

Fig. 41. Near infrared absorption of conducting $KTaO_3$.

the ratio between m_c^* at 300°K and 78°K. We obtain $m_{300} \sim 80$ and $m_{78} \sim 13$. Large effective masses have also been observed in TiO_2 by Breckenridge and Hosler.[67] These calculations allow separation of the mobility temperature dependence into τ and m_c^* parts in the expression $\mu = \frac{e\tau}{m_c^*}$. We obtain

$$\frac{\tau_{78}}{\tau_{300}} \approx 10 \approx \left(\frac{300}{78}\right)^{1.7}.$$

This expression suggests that $\tau \propto T^{-1.7}$. This is of the same order of magnitude as the

temperature dependence expected for acoustical mode scattering.[71]

Thus far we have not suggested a mechanism to explain the large effective mass of the carriers or the temperature dependence of the effective mass. Because of the ferroelectric character of $KTaO_3$, a rapid increase in dielectric constant occurs with decreasing temperature and we suggest that at least the temperature dependence of the effective mass is related to this increase in dielectric constant. Relevant work has been done by Breckenridge and Hosler[67] on semiconducting (reduced) rutile (TiO_2). These authors report large effective masses (30-100 m_o), which they suggest are associated with a narrow impurity band. This band presumably arises from the overlap of Bohr-type orbits surrounding the donor centers. In high dielectric constant materials these orbits can be abnormally large and may be of approximately the same magnitude as the average spacing between donor centers. Conduction then takes place between centers by a "hopping" mechanism associated with the donor sublattice. The first Bohr radius in the simplest theory is $r_b = \frac{\kappa a_o}{Z}$, where κ is the low-frequency dielectric constant, a_o is the atomic unit of distance (0.53 Å), and Z is the effective nuclear charge of the donor centers. For $KTaO_3$, $r_b \sim 60$ Å at room temperature, if a doubly charged $O^=$ vacancy is assumed to be the donor, and if the average spacing between donors is ~100 Å for a donor concentration of $N \sim 10^{18}$ cm^{-3}. At 4.2°K, r_b increases to approximately 1000 Å. The Bohr orbits are clearly large enough to overlap. Because $r_b \propto \kappa$, the "hopping" probability, or charge overlap between donor centers, should increase with increasing κ. This should broaden the impurity band and thereby reduce the effective mass as the temperature is lowered. This qualitative argument is confirmed in rutile for which m_c^* is less in the high dielectric constant c direction than in the a direction. The reduced effective mass in $KTaO_3$ at low temperature may have the same origin.

Because insufficient data were obtained to determine the complete temperature-dependence of Hall coefficient, effective mass, and mobility in $KTaO_3$, our conclusions about transport phenomena are only tentative. To summarize,

1. Conduction is n-type.
2. Free carriers are not significantly frozen out at 4.2°K.
3. The conductivity effective mass is large and strongly temperature dependent.
4. The $\mu \propto T^{-3}$ temperature dependence about 78°K can be separated into an effective-mass dependence and a $\tau_L \propto T^{-1.7}$ relaxation-time dependence. This suggests that acoustical mode scattering may dominate at these temperatures.
5. An impurity band or "hopping" mechanism for conductivity may explain the strong decrease in effective mass with decreasing temperature.

These tentative conclusions[73] indicate a need for further work on transport phenomena in $KTaO_3$. This is a good material for such an investigation because electron mobilities are large enough to permit relatively easy Hall-effect measurements. Since these crystals are conducting and transparent,we can also make free-carrier optical absorption experiments in the same sample. This allows us to separate the mobility temperature

dependence into effective-mass and relaxation-time components. $KTaO_3$ has an added advantage for impurity-band studies, which stems from its structure. The simple cubic structure should simplify any theory and should also eliminate the complication encountered in rutile because of the effect of birefringence.

XI. EVIDENCE FOR THE EXISTENCE OF O-H BONDS IN $KTaO_3$

Optical absorption experiments in $KTaO_3$ reveal narrow absorption bands near 3500 cm^{-1}. These data are plotted in Figs. 42 and 43 at room temperature and

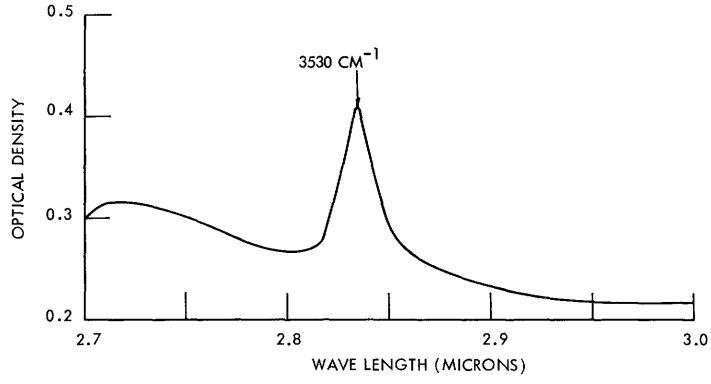

Fig. 42. O-H band in undoped $KTaO_3$ at room temperature.

at 78°K for undoped crystals. The position of the bands suggests a typical O-H stretching vibration of the kind observed in rutile by Soffer[74] and discussed by von Hippel.[68] In solids the O-H stretching frequency depends upon the O-O distance

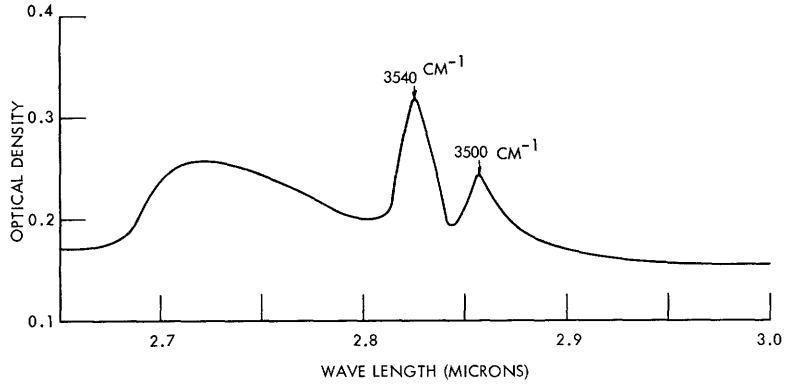

Fig. 43. O-H bands in undoped $KTaO_3$ at 78°K.

between competing oxygen ions.[75]

In the case of $KTaO_3$, the entrapped hydrogen is almost certainly caused by H_2O in the starting chemicals (K_2CO_3 is hygroscopic). Table XVIII shows band positions obtained from a variety of samples at room temperature and liquid-nitrogen temperature. The frequency of the band in undoped $KTaO_3$ predicts[75] an O-O spacing of 2.85 Å, as compared with the X-ray value of 2.82 Å. Two bands are observed at room temperature in Mn-doped and Co-doped samples.

Table XVIII. Positions of O-H stretching bands.

Sample	Temperature (°K)	Band positions (cm^{-1})	Crystal thickness
Undoped	300	3530	4.2
Undoped	78	3540, 3500	
Mn-doped	300	3530, 3493	7.34
Mn-doped	78	3540, 3500, 4300	
Fe-doped	300	3530	
Fe-doped	78	3540, 3500	
Co-doped	300	3530, 3493 (not shown)	7.55
Co-doped	78	3540, 3500	

All crystals also have a weak band at approximately 4300 cm^{-1}. This is apparently the same weak band (4340 cm^{-1}) observed in rutile by Soffer.

XII. CONCLUSION

The major conclusion to be drawn from our EPR study in $KTaO_3$ is the validity of our order-of-magnitude estimate relating the parameter D in the axial spin Hamiltonian to the lattice polarization P by the expression

$$D \approx P^2,$$

where D is in units of 10^{-4} cm^{-1}, and P is in $\mu coulombs/cm^2$. This result suggests that very large polarizations are required, as predicted, in order to obtain a significant EPR Stark effect.

We have also shown that a significant fraction of Fe^{3+} ions can be substituted in cubic sites of $KTaO_3$ without altering the local cell symmetry, even though a valence mismatch of 2 exists. The required charge compensation is sufficiently remote, hence it does not affect the Fe^{3+}-O_6 octahedron. A large fraction of the Fe^{3+} ions, however, does not experience cubic symmetry but appears to be in large axial fields directed along any of the three equivalent [100] crystalline directions. This suggests a nearest-neighbor charge compensation $O^=$ vacancy. We have observed an Fe^{5+} EPR spectrum with a large resolved hfs which we have attributed to σ coupling of the $d\epsilon$ orbitals of Fe^{5+} to the 8 next-nearest-neighbor spin 3/2 potassium nuclei. This inhomogeneous broadening is the apparent cause of the much broader $\frac{1}{2} \rightarrow -\frac{1}{2}$ lines observed for Fe^{3+} in $KTaO_3$ when compared with Fe^{3+} in $SrTiO_3$ and $BaTiO_3$. The cubic splitting parameter a is also considerably larger in $KTaO_3$ than in $BaTiO_3$ or $SrTiO_3$. The reason for this is not known.

Several aspects of the EPR results are not understood, particularly the fact that $g_\perp = 4.24 > 4$ for the Fe^{5+} spectrum. Other puzzling aspects include the angular dependence of the hyperfine structure, the g = 3.0 Kramers doublet with the possibility of double quantum jumps, symmetry of 45 ± 5° for several EPR lines of Fe-doped $KTaO_3$ and the EPR spectra with Mn impurities. The Mn spectra, in fact, could not be described by a simple spin Hamiltonian by assuming any valence state of manganese. The fact that a six-line hfs was observed indicates that the spectrum was caused by Mn, therefore we are tempted to suggest that rather drastic admixtures of ligand orbitals are involved. Further study is clearly called for in conjunction with molecular orbital calculations.

More work on the EPR Stark effect would also be of interest. Observation with the electric field parallel to the magnetic field would double the observed effect.

The Co^{3+} ion in $KTaO_3$ gave the most interesting optical spectrum. We have suggested the possibility that there is crossing between low-spin and high-spin ground states with cooling, and it would be of interest to extend the study of the Co^{3+} optical spectrum.

Dielectric constant measurements have shown that the Curie temperature of $KTaO_3$ is ~1°K rather than the previously published value of 13°K.

Finally, we have briefly investigated the transport properties of slightly reduced

$KTaO_3$ and found that it is an n-type semiconductor with a mobility of 28 cm^2/volt sec at room temperature. The mobility is strongly temperature-dependent, increasing to >20,000 cm^2/volt sec at 4.2°K.

APPENDIX

SOLUTION OF AXIAL SPIN-HAMILTONIAN FOR $3d^5$, $3d^3$, AND $3d^2$

The axial spin-Hamiltonian is[48]

$$\mathcal{H} = g\beta H \cdot S + D\left[S_z^2 - \frac{1}{3}S(S+1)\right],$$

where g is assumed to be isotropic, and the z and axial directions coincide. If H lies in the x-z plane and θ is the angle between z and H,

$$\mathcal{H} = g\beta H S_z \cos\theta + \frac{g\beta H \sin\theta}{2}(S_+ + S_-) + D\left[S_z^2 - \frac{1}{3}S(S+1)\right]. \qquad \text{(A-1)}$$

If a lower $\pm 1/2$ Kramers doublet lies far below all other doublets ($D \gg g\beta H > 0$), the angular dependence of this doublet can be calculated by diagonalizing only the 2×2 submatrix of the $\pm 1/2$ terms.

a. The Fe^{3+} ion. The spin operator S is 5/2 for the Fe^{3+} ion, and the corresponding 2×2 matrix is

M	$\frac{1}{2}$	$-\frac{1}{2}$
$\frac{1}{2}$	$\frac{1}{2}g\beta H\cos\theta - \frac{8}{3}D - E$	$\frac{3}{2}g\beta H$
$-\frac{1}{2}$	$\frac{3}{2}g\beta H$	$-\frac{1}{2}g\beta H\cos\theta - \frac{8}{3}D - E$

Solving for the energy, we obtain

$$E = -\frac{8}{3}D \pm \beta H\left(\frac{g^2}{4}\cos^2\theta + \frac{9g^2}{4}\sin^2\theta\right)^{1/2}$$

and the transition energy

$$h\nu = 2\beta H\left(\frac{g^2}{4}\cos^2\theta + \frac{9g^2}{4}\sin^2\theta\right)^{1/2}$$

or

$$h\nu = g'\beta H,$$

where $g' = \left(g_{\|}^2 \cos^2\theta + g_{\perp}^2 \sin^2\theta\right)^{1/2}$, and $g_{\|} = g \approx 2.00$, $g_{\perp} = 3g \approx 6.00$.

To calculate the six energy levels within S = 5/2 at $\theta = 90°$ we used the following 6×6 matrix obtained from Eq. A-1. We shifted the zero of energy to $-\frac{8}{3}D$, and defined $\epsilon = \frac{E}{D}$ and $h = \frac{g\beta H}{D}$.

M	$\frac{5}{2}$	$\frac{3}{2}$	$\frac{1}{2}$	$-\frac{1}{2}$	$-\frac{3}{2}$	$-\frac{5}{2}$
$\frac{5}{2}$	$6-\epsilon$	$\frac{\sqrt{5}}{2}h$				
$\frac{3}{2}$	$\frac{\sqrt{5}}{2}h$	$3-\epsilon$	$\sqrt{2}\,h$			
$\frac{1}{2}$		$\sqrt{2}\,h$	$-\epsilon$	$\frac{3}{2}h$		
$-\frac{1}{2}$			$\frac{3}{2}h$	$-\epsilon$	$\sqrt{2}\,h$	
$-\frac{3}{2}$				$\sqrt{2}\,h$	$3-\epsilon$	$\frac{\sqrt{5}}{2}h$
$-\frac{5}{2}$					$\frac{\sqrt{5}}{2}h$	$6-\epsilon$

The energy ϵ can be expanded in powers of h by making use of standard degenerate perturbation theory. We have

$$\mathcal{H}_{eff} = \mathcal{H}_{ij} + \sum_n \frac{\langle i|\mathcal{H}|n\rangle\langle n|\mathcal{H}|j\rangle}{E - E_n} + \ldots,$$

where i and j refer to the two $\pm 1/2$ states, and $|n\rangle$ are the higher lying levels. The new 2×2 matrix of the $\pm 1/2$ states is

M	$\frac{1}{2}$	$-\frac{1}{2}$
$\frac{1}{2}$	$-\epsilon - \frac{2h^2}{3-\epsilon}$	$\frac{3}{2}h$
$-\frac{1}{2}$	$\frac{3}{2}h$	$-\epsilon - \frac{2h^2}{3-\epsilon}$

Solving for ϵ, we obtain

$$\epsilon = \pm\frac{3}{2}h - \frac{2}{3}h^2 \mp \frac{41}{12 \cdot 16}h^3 \pm \frac{3}{32}h^3$$

and

$$\Delta\epsilon = h\nu = 3h - \frac{23}{96}h^3.$$

If $h\nu = g'\beta H$ and $h = g\beta H/D$, the final result is

$$g' = 3g\left[1 - \frac{23}{288}\left(\frac{g\beta H}{D}\right)^2 + \ldots\right].$$

b. The Fe^{5+} ion. The spin operator S is 3/2 for the Fe^{5+} ion, and the corresponding 2×2 matrix is

M	$\frac{1}{2}$	$-\frac{1}{2}$
$\frac{1}{2}$	$\frac{1}{2}g\beta H\cos\theta$ $-E$	$g\beta H \sin\theta$
$-\frac{1}{2}$	$g\beta H \sin\theta$	$-\frac{1}{2}g\beta H\cos\theta$ $-E$

Solving for the energy, we obtain

$$E = \pm\beta H\left(\frac{g^2}{4}\cos^2\theta + g^2\sin^2\theta\right)^{1/2}.$$

The transition energy is

$$h\nu = 2\beta H\left(\frac{g^2}{4}\cos^2\theta + g^2\sin^2\theta\right)^{1/2},$$

or

$$h\nu = g'\beta H,$$

where $g' = \left(g_{\parallel}^2\cos^2\theta + g_{\perp}^2\sin^2\theta\right)^{1/2}$, and $g_{\parallel} = g \sim 2.00$, $g_{\perp} = 2g \sim 4.00$.

c. The Mn ion. The matrix of $Mn^{5+}(3d^2)$ at $\theta = 90°$ can be obtained similarly from Eq. A-1 with S = 1.

M	1	0	-1
1	$\frac{1}{3}D - E$	$\frac{\sqrt{2}}{2}g\beta H$	0
0	$\frac{\sqrt{2}}{2}g\beta H$	$-\frac{2}{3}D - E$	$\frac{\sqrt{2}}{2}g\beta H$
-1	0	$\frac{\sqrt{2}}{2}g\beta H$	$\frac{1}{3}D - E$

Solving for the energy, we obtain

$$E_{1,2} = E - \frac{2}{3} D = D, \ \frac{D}{2} \pm \frac{1}{2}(D^2+4g^2\beta^2H^2)^{1/2}.$$

If we substitute $g\beta H = h$, the level spacing within the doublet is given by

$$h\nu = -\frac{D}{2} + \frac{1}{2}(D^2+4h^2)^{1/2}$$

or if $h \gg D$

$$h\nu \approx -\frac{D}{2} + h + \frac{1}{8}\frac{D^2}{h} + \ldots$$

and the slope is

$$g_s = \frac{dh\nu}{d\beta H} = g\left[1 - \frac{1}{8}\left(\frac{D}{g\beta H}\right)^2 + \ldots\right].$$

Acknowledgment

The author wishes to thank Professor Robert L. Kyhl, who supervised this work and offered many helpful suggestions. Thanks are also due to the Microwave Spectroscopy Group of the Research Laboratory of Electronics, M. I. T., for providing the EPR spectrometer and other equipment. The Laboratory for Insulation Research, M. I. T., under the direction of Professor Arthur A. von Hippel, generously provided crystal-growing and auxiliary facilities, as well as the optical spectrometer. The assistance of members of the Laboratory for Insulation Research is gratefully acknowledged, in particular, that of Dr. Arthur Linz, for his helpful discussions.

Thanks are extended to the Bell Telephone Laboratories, Inc., for support extended the author under their Communications Development Training Program.

References

1. N. Bloembergen, Science 133, 1363 (1961).
2. N. Bloembergen and E. B. Royce, in Paramagnetic Resonance, Proceedings of the First International Conference held in Jerusalem, July 16-20, 1962, edited by W. Low (Academic Press, New York, 1963), Vol. 2, p. 607.
3. J. O. Artman and J. C. Murphy, in Paramagnetic Resonance, Proceedings of the First International Conference held in Jerusalem, July 16-20, 1962, edited by W. Low (Academic Press, New York, 1963), Vol. 2, p. 634.
4. M. E. Browne, Phys. Rev. 121, 1699 (1961).
5. G. W. Ludwig and H. H. Woodbury, Phys. Rev. Letters 7, 240 (1961).
6. G. W. Ludwig and F. S. Ham, in Paramagnetic Resonance, Proceedings of the First International Conference held in Jerusalem, July 16-20, 1962, edited by W. Low (Academic Press, New York, 1963), Vol. 2, p. 620.
7. F. S. Ham, Phys. Rev. Letters 7, 242 (1961).
8. M. Weger and E. Feher, in Paramagnetic Resonance, Proceedings of the First International Conference held in Jerusalem, July 16-20, 1962, edited by W. Low (Academic Press, New York, 1963), Vol. 2, p. 628.
9. A. W. Hornig, P. C. Rempel, and H. E. Weaver, J. Phys. Chem. Solids 10, 1 (1959).
10. W. Känzig, Ferroelectrics and Antiferroelectrics, in Solid State Physics, Vol. 4, edited by F. Seitz and D. Turnbull (Academic Press, Inc., New York, 1957).
11. H. Megaw, Ferroelectricity in Crystals (Methuen and Co. Ltd., London, 1957).
12. W. Low and D. Shaltiel, Phys. Rev. Letters 1, 51 (1958).
13. L. Rimai and G. A. deMars, Phys. Rev. 127, 702 (1962).
14. K. A. Müller, Phys. Rev. Letters 2, 341 (1959).
15. W. I. Dobrov, R. F. Vieth, and M. E. Browne, Phys. Rev. 115, 79 (1959).
16. K. A. Müller, Paramagnetische Resonanz von Fe^{3+} in $SrTiO_3$ Einkristallen, Prom. Wr. 2791 (Buchdruckerei Birkhauser A. G., 1958).
17. K. A. Müller, in Paramagnetic Resonance, Proceedings of the First International Conference held in Jerusalem, July 16-20, 1962, edited by W. Low (Academic Press, New York, 1963), Vol. 1, p. 17.
18. L. Rimai and G. A. deMars, in Paramagnetic Resonance, Proceedings of the First International Conference held in Jerusalem, July 16-20, 1962, edited by W. Low (Academic Press, New York, 1963), Vol. 1, p. 51.
19. R. S. Rubins and W. Low, in Paramagnetic Resonance, Proceedings of the First International Conference held in Jerusalem, July 16-20, 1962, edited by W. Low (Academic Press, New York, 1963), Vol. 1, p. 59.
20. S. Triebwasser, Phys. Rev. 101, 993 (1956).
21. S. Triebwasser, Phys. Rev. 114, 63 (1959).
22. J. K. Hulm, B. T. Matthias, and E. A. Long, Phys. Rev. 79, 885 (1950).
23. J. P. Remeika, J. Am. Chem. Soc. 76, 940 (1954).
24. J. P. Remeika, Private communications, Bell Telephone Laboratories, Inc., 1961.
25. C. E. Miller, J. Appl. Phys. 29, 233 (1958).
26. A. Reisman, F. Holtzberg, M. Berkenblit, and M. Berry, J. Am. Chem. Soc. 78, 4514 (1956).
27. Suk Suet Soo, The Dielectric Behavior of $KTaO_3$, S. B. Thesis, Department of Physics, M. I. T., 1952.

28. A Nishioka, K. Sekikawa, and M. Owaki, J. Phys. Soc. Japan 11, 180 (1956).
29. J. H. Barrett, Phys. Rev. 86, 118 (1952).
30. J. C. Slater, Phys. Rev. 78, 748 (1950).
31. W. Cochran, Advances in Physics 9, 387 (1958).
32. A. Okaya and L. F. Barash, Proc. IRE 50, 2081 (1962).
33. G. Rupprecht and R. O. Bell, Phys. Rev. 125, 1915 (1962).
34. B. D. Silverman, Phys. Rev. 125, 1921 (1962).
35. P. Vousden, Acta Cryst. 4, 373 (1951).
36. Y. Tanabe and S. Sugano, J. Phys. Soc. Japan 9, 753 (1954).
37. J. S. Griffith, The Theory of Transition Metal Ions (Cambridge University Press, London, 1961), pp. 261-262.
38. R. S. Mulliken, J. Chem. Phys. 3, 375 (1935).
39. H. Bethe, Ann. Phys. 3, 133 (1929).
40. C. K. Jorgensen, Absorption Spectra and Chemical Bonding in Complexes (Pergamon Press, New York, 1962).
41. A. M. Clogston, J. Appl. Phys. 31, 1985 (1960).
42. H. W. Gandy, Phys. Rev. 113, 795 (1959).
43. S. Geshwind, P. Kisliuk, M. P. Klein, J. P. Remeika, and D. L. Wood, Phys. Rev. 126, 1684 (1962).
44. D. R. Stephens and H. G. Drickamer, J. Chem. Phys. 35, 424 (1961).
45. W. E. Blumberg, Phys. Rev. 119, 1842 (1960).
46. A. M. Portis, Phys. Rev. 91, 1071 (1953).
47. K. Halback, Helv. Phys. Acta 27, 259 (1954).
48. D. Carter and A. Okaya, Phys. Rev. 118, 1485 (1960).
49. W. Low, Paramagnetic Resonance in Solids (Academic Press, New York, 1960).
50. R. de L. Kronig and C. J. Bouwkamp, Physica 6, 290 (1939).
51. B. Bleany and K. W. H. Stevens, Rep. Progr. Phys. 16, 108 (1953).
52. A. Shuskus, Phys. Rev. 127, 1529 (1962).
53. J. E. Geusic, M. Peter and E. O. Schultz-DuBois, Bell System Tech. J. 38, 291 (1960).
54. A. M. Germanier, D. Gainon, and R. Lacroix, Phys. Letters (Netherlands) 2, 105 (1962).
55. M. A. Durand, Phys. Rev. 50, 449 (1936).
56. W. M. Walsh, Jr., Phys. Rev. 104, 324 (1956).
57. A. M. Germanier and R. Lacroix, Helv. Phys. Acta 34, 401 (1961).
58. W. M. Walsh, Jr., Cruft Laboratory Progress Reports Nos. 41-48, Harvard University, Cambridge, Mass., 1956-1958.
59. E. J. Huibregtse, M. E. Drougard, and D. R. Young, Phys. Rev. 98, 1562 (1955).
60. W. Merz, Phys. Rev. 91, 513 (1953).
61. W. Grant, Ph. D. Thesis, Department of Physics, M. I. T., June 1962.
62. L. H. Bennett and J. I. Budnick, Phys. Rev. 120, 1812 (1960).
63. M. Tinkham, Proc. Roy. Soc. (London) A236, 535, 549 (1956).
64. J. C. Eisenstein, J. Chem. Phys. 25, 142 (1956).

65. A. D. Liehr, J. Chem. Educ. 39, 135 (1962).

66. M. Weger, Bell System Tech. J. 39, 1013 (1960).

67. R. G. Breckenridge and W. R. Hosler, Phys. Rev. 91, 793 (1953).

68. A. von Hippel, J. Kalnajs, and W. B. Westphal, Dipoles and Charge Carriers in Rutile, Technical Report 164, Laboratory for Insulation Research, M. I. T., June 1961.

69. A. Branwood, O. H. Hughes, J. D. Hurd, and R. H. Tredgold, Proc. Phys. Soc. (London) 79, 1161 (1962).

70. A. Branwood and R. H. Tredgold, Proc. Phys. Soc. (London) 76, 93 (1960).

71. N. B. Hannay, Semiconductors (Reinhold Publishing Company, New York, 1959).

72. H. A. Lyden, The Effective Masses of Free Carriers in PbTe: Their Temperature Dependence and Contribution to Transport Properties, Scientific Report No. 7, Air Force Cambridge Research Laboratory, Bedford, Mass., January 15, 1962.

73. Since this report was written, these conclusions have been modified as a result of further investigation. See S. H. Wemple, Transport Properties of Oxygen-Deficient $KTaO_3$ (accepted for publication by the Physical Review).

74. B. H. Soffer, J. Chem. Phys. 35, 940 (1961).

75. G. C. Pimentel and A. L. McClellen, The Hydrogen Bond (Freeman and Co., San Fransico, 1960).

76. A. Linz, Private communication, Laboratory for Insulation Research, M. I. T., 1961.